INFORMATION TO USERS

This manuscript has been reproduced from the microfilm master. UMI films the text directly from the original or copy submitted. Thus, some thesis and dissertation copies are in typewriter face, while others may be from any type of computer printer.

The quality of this reproduction is dependent upon the quality of the copy submitted. Broken or indistinct print, colored or poor quality illustrations and photographs, print bleedthrough, substandard margins, and improper alignment can adversely affect reproduction.

In the unlikely event that the author did not send UMI a complete manuscript and there are missing pages, these will be noted. Also, if unauthorized copyright material had to be removed, a note will indicate the deletion.

Oversize materials (e.g., maps, drawings, charts) are reproduced by sectioning the original, beginning at the upper left-hand corner and continuing from left to right in equal sections with small overlaps.

Photographs included in the original manuscript have been reproduced xerographically in this copy. Higher quality 6" x 9" black and white photographic prints are available for any photographs or illustrations appearing in this copy for an additional charge. Contact UMI directly to order.

Bell & Howell Information and Learning
300 North Zeeb Road, Ann Arbor, MI 48106-1346 USA
800-521-0600

UMI®

Reproduced with permission of the copyright owner. Further reproduction prohibited without permission.

NOTE TO USERS

This reproduction is the best copy available.

UMI

Reproduced with permission of the copyright owner. Further reproduction prohibited without permission.

DISSERTATION

Dye Sensitization of TiO_2 Crystals and Nanocrystalline Films with a Ruthenium Based Dye

Submitted by

Akiko Fillinger

Department of Chemistry

In partial fulfillment of the requirements
for the Degree of Doctor of Philosophy

Colorado State University

Fort Collins. Colorado

Fall 2000

Reproduced with permission of the copyright owner. Further reproduction prohibited without permission.

UMI Number: 3002075

UMI®

UMI Microform 3002075
Copyright 2001 by Bell & Howell Information and Learning Company.
All rights reserved. This microform edition is protected against
unauthorized copying under Title 17, United States Code.

Bell & Howell Information and Learning Company
300 North Zeeb Road
P.O. Box 1346
Ann Arbor, MI 48106-1346

Reproduced with permission of the copyright owner. Further reproduction prohibited without permission.

COLORADO STATE UNIVERSITY

October. 26. 2000

We hereby recommend that the dissertation prepared under our supervision by **Akiko Fillinger** entitled *Dye Sensitization of TiO_2 Crystals and Nanocrystalline Films with a Ruthenium Based Dye* be accepted as fulfilling in part the requirements for the degree of **Doctor of Philosophy.**

Committee on Graduate Work

Adviser

Department Head

Reproduced with permission of the copyright owner. Further reproduction prohibited without permission.

Abstract of Dissertation

Dye Sensitization of TiO_2 Crystals and Nanocrystalline Films with a Ruthenium Based Dye

The dye/semiconductor interface of a recently developed highly efficient (overall conversion efficiency > 13 %) dye sensitized nanocrystalline TiO_2 solar cell was investigated. First, the adsorption and desorption rates of the dye (*cis*-di(thiocyanato)bis(2,2'-bipyridyl-4,4'-dicarboxylate)ruthenium(II):N3), and the relationship between the dye coverage and the photon-to-current conversion efficiencies were examined for nanocrystalline TiO_2 films. A two-step dye adsorption mechanism was postulated where initial binding of N3 is through one carboxyl group, with subsequent binding of two or more carboxyl groups. The photon-to-current conversion efficiencies were found to increase abruptly at a coverage of about 0.3 monolayers. To explain the non-linear increases in the conversion efficiencies, a hole-hopping mechanism was proposed. At greater than 30 % coverage, hole transfer between adjacent N3 molecules becomes possible and facilitates the regeneration of the oxidized N3 by the redox species (I^-) in the matrix of the nanoporous structure.

Reproduced with permission of the copyright owner. Further reproduction prohibited without permission.

Natural anatase crystals were also investigated as substrates for dye sensitization by N3 to circumvent the complexity of the nanoporous structure of the nanocrystalline TiO_2 films. A crystal face dependence of the sensitization yield was observed and explained with the variation in the distances between the Ti binding sites by different crystal faces. The dye sensitized photocurrents with the natural anatase crystals had millisecond rise times. The rise time decreased with greater light intensity and greater dye coverage, suggesting that trapping and detrapping of injected electrons at traps in the crystals is involved in the electron transport in the natural anatase crystals. The absorbed photon to current efficiency of the nanocrystalline films was calculated to be approximately three to seven times greater than that of the single crystals, indicating more recombination in the single crystals.

Finally, the surface morphologies of natural and synthetic TiO_2 crystals were investigated with scanning electron microscopy and atomic force microscopy. Several surface treatments were attempted to obtain flat terraced surfaces suitable for imaging the adsorbed N3.

Akiko Fillinger

Department of Chemistry
Colorado State University
Fort Collins, CO 80523

Fall 2000

Reproduced with permission of the copyright owner. Further reproduction prohibited without permission.

ACKNOWLEDGMENTS

I sincerely thank my adviser, Professor Bruce A. Parkinson, for mentoring me in my graduate work in electrochemistry and my research subject of photovoltaic solar cells. His sharp intuition and vast knowledge have always fueled me to proceed to the next step.

To the members of the Parkinson group, whom I spent time with, I would like to give thanks for their heartfelt comradeship, which supported me in academic matters and psychological manner. I am also greatly thankful to Professor Nancy Levinger and Professor Ellen Fisher for providing me constant morale support.

Finally, Chris, who has shared so much happiness and frustration with me through my graduate life, thank you so much for letting me pursuit my academic goal and for your infinite support.

Reproduced with permission of the copyright owner. Further reproduction prohibited without permission.

Table of Contents

CHAPTER ONE

Background 1

1.1. Brief History and Overview of Photoelectrochemical Cells 1

1.1.1. Mechanism of Operation of Electrochemical Photovoltaic Solar Cells 2

1.1.2. Different Forms of Photoelectrochemical Cells 4

1.1.3. Development of Practical Photoelectrochemical Cells 6

1.1.4. Dye Sensitization of Large Bandgap Semiconductors 9

1.1.5. Evaluation of Efficiency 11

1.2. Dye-Sensitized Nanocrystalline TiO_2 Solar Cells 14

1.2.1. Operation and Energetics of the Dye-sensitized Nanocrystalline TiO_2 Solar Cell 14

1.2.2. Nanocrystalline TiO_2 Semiconductor Electrodes 18

1.2.3. Effcient Sensitizer 22

1.2.4. Charge Transport in Nanocrystalline TiO_2 Film 28

1.2.5. Kinetics of the Reactions in the Dye-Sensitized Nanocrystalline TiO_2 Solar Cell 33

1.3. Unknown Aspects of the Dye-Sensitized Nanocrystalline TiO_2 Solar Cells 36

References Cited in Chapter 1 39

Reproduced with permission of the copyright owner. Further reproduction prohibited without permission.

CHAPTER TWO

The Adsorption Behavior of a Ruthenium Based Sensitizing Dye to Nanocrystalline TiO_2: Coverage Effects on the External and Internal Sensitization Quantum Yield ---- 44

Abstract ---- 44

2.1. Introduction ---- 45

2.2. Experimental ---- 46

2.3. Results and Discussion ---- 48

2.3.1. N3 Adsorption and Desorption ---- 48

2.3.2. Model for N3 Binding to Nanocrystalline TiO_2 ---- 53

2.3.3. Dye Coverage Effects on Incident Photon to Current Efficiency ---- 57

2.3.4. Absorbance of N3 Adsorbed to a Nanocrystalline TiO_2 Film ---- 59

2.3.5. Dye Coverage Effects on Absorbed Photon to Current Efficiency ---- 60

2.3.6. Possible Explanation for the Dye Coverage Effects on APCE ---- 63

2.4. Conclusions ---- 68

References Cited in Chapter 2 ---- 69

Reproduced with permission of the copyright owner. Further reproduction prohibited without permission.

CHAPTER THREE

Dye Sensitization of Natural Anatase Crystals with a Ruthenium Based Dye 72

Abstract 72

3.1. Introduction 73

3.2.Experimental 75

3.3. Results and Discussion 79

3.3.1. Sensitization behavior and Surface Morphology of the Natural Anatase Crystals 79

3.3.2. Characterization of the Bulk Properties of the Anatase Crystals 90

3.3.3. Discussion of the Face Dependence of the Dye Sensitization 95

3.3.4. Sensitization Photocurrent Transients 100

3.3.5. Comparison of Sensitization Behavior between the Anatase Natural Crystals and Nanocrystalline Films 106

3.4. Conclusions 114

References cited in Chapter 3 115

Reproduced with permission of the copyright owner. Further reproduction prohibited without permission.

CHAPTER FOUR

Imaging Crystal Surfaces ---- 118

4.1. Sample Crystals ---- 120

4.2. Atomic Force Microscopy ---- 121

4.3. Surface treatments and Morphologies of Crystal Surfaces ---- 125

i) Brazilian Anatase Crystals ---- 125

ii) Norwegian and Russian Anatase Crystals ---- 133

iii) Synthetic Anatase Thin Film ---- 137

iv) Synthetic Rutile Single Crystals ---- 137

4.4. Summary and Direction for Future Work ---- 142

References cited in Chapter 4 ---- 144

Reproduced with permission of the copyright owner. Further reproduction prohibited without permission.

List of Figures

CHAPTER ONE

Figure 1.1. Schematic of an electrochemical photovoltaic cell ---- 3

Figure 1.2. Schematic of different types of photoelectrochemical cells ---- 5

Figure 1.3. The solar spectrum and the bandgap of the semiconductor ---- 7

Figure 1.4. Schematic of a dye-sensitized photovoltaic cell ---- 10

Figure 1.5. Relationship between the output power, the short-circuit current, the open-circuit voltage, and the fill factor ---- 13

Figure 1.6. Schematic of dye-sensitized nanocrystalline TiO_2 solar cell ---- 15

Figure 1.7. Photocurrent-voltage characteristics of the dye-sensitized nanocrystalline TiO_2 solar cell ---- 17

Figure 1.8. Scanning electron micrograph of a nanocrystalline TiO_2 film ---- 19

Figure 1.9. TiO_2 synthesis by hydrolysis of titanium isopropooxide ---- 21

Figure 1.10. Absorption spectrum of a TiO_2 nanocrystalline film ---- 23

Figure 1.11. Molecular structure of the sensitizer ---- 24

Figure 1.12. Absorption spectrum of N3 ---- 25

Figure 1.13. Molecular orbital diagram for N3 attached to TiO_2 surface and the charge transfer between them ---- 27

Figure 1.14. Photo action spectrum of a nanocrystalline TiO_2 film sensitized with N3 ---- 29

Figure 1.15. Electron concentration profile inside of the dye-sensitized nanocrystalline TiO_2 film ---- 31

Reproduced with permission of the copyright owner. Further reproduction prohibited without permission.

Figure 1.16. Rates for the electron transfer reactions in the dye-sensitized nanocrystalline TiO_2 electrode 34

Figure 1.17. Goals of this project 37

CHAPTER TWO

Figure 2.1. Adsorption of N3 to nanocrystalline TiO_2 49

Figure 2.2. Desorption of N3 from nanocrystalline TiO_2 50

Figure 2.3. N3 adsorption and desorption isotherms 52

Figure 2.4. Possible binding modes of N3 to TiO_2 (101) surface 55

Figure 2.5. Incident photon to current efficiency of nanocrystalline TiO_2 films sensitized with N3 at various coverages 58

Figure 2.6. Absorbance spectra of N3 adsorbed to a nanocrystalline TiO_2 film 61

Figure 2.7. Absorbed photon to current efficiency of nanocrystalline TiO_2 film 62

Figure 2.8. Hole hopping mechanism 67

Table 2.1. Ratio of desorbed N3 to initially adsorbed N3 51

CHAPTER THREE

Figure 3.1. Optical micrographs of natural anatase crystals 76

Figure 3.2. Photocurrent spectra of anatase crystals sensitized with N3 80

Figure 3.3. Plot of the IPCE of an anatase crystals vs. [N3] 81, 84

Figure 3.4. Scanning electron micrographs of the natural anatase crystals 85

Reproduced with permission of the copyright owner. Further reproduction prohibited without permission.

Figure 3.5. Plot of the $IPCE_{max}$ vs. time ---- 88

Figure 3.6. Photocurrent-voltage curves of the natural crystals ---- 93, 94

Figure 3.7a & b. Crystal structure model of anatase and the distances between Ti sites ---- 98

Figure 3.7.c. Possible combinations of carboxyl groups of N3 for bidentate chelating binding ---- 99

Figure 3.8. Photocurrent transients of the sensitized natural anatase crystal ---- 102

Figure 3.9. Plot of rise time of dye sensitized photocurrent for the natural anatase crystals ---- 104

Figure 3.10. The trap/detrapping mechanism involved in electron transport in the natural anatase crystals ---- 105

Figure 3.11. Plot of photocurrent vs. light intensity ---- 107

Table 3.1. Comparison of the anatase crystals with nanocrystalline TiO_2 film ---- 109

CHAPTER FOUR

Figure 4.1. Russian anatase crystal ---- 120

Figure 4.2. Crystal model of rutile and the distances between Ti sites ---- 122

Figure 4.3. Schematic of AFM fluid cell ---- 124

Figure 4.4. Optical micrographs of Brazilian anatase crystal ---- 126

Figure 4.5. AFM image of a Brazilian anatase crystal (001) face ---- 127

Figure 4.6. Crystal potted in epoxy ---- 128

Figure 4.7 AFM images of a Brazilian anatase after polished ---- 130

Figure 4.8. AFM images of a Brazilian anatase after polished and treated with hot 5 M NaOH ---- 131

Figure 4.9. AFM images of the Brazilian anatase in ethanol ---- 132

Reproduced with permission of the copyright owner. Further reproduction prohibited without permission.

Figure 4.10. Optical micrograph and crystal model of a Norwegian anatase (101) face 134

Figure 4.11. AFM images of a Russian anatase as received 135

Figure 4.12. AFM images of a Russian anatase after polished 136

Figure 4.13. AFM images of a synthetic anatase film 138

Figure 4.14. AFM images of synthetic rutile single crystal (001) face as received 149

Figure 4.15. AFM images of synthetic rutile in ethanol 140

Figure 4.16. AFM images of a synthetic rutile (100) face as received 141

Reproduced with permission of the copyright owner. Further reproduction prohibited without permission.

CHAPTER ONE

Background

The development of renewable energy has become very important because of the environmental deterioration caused by the consumption of fossil fuel and the concern for the exhaustion of fossil fuels in the near future. One of those alternative energy sources is solar energy. Electrochemical photovoltaic cells convert solar energy to electric energy based on the photovoltaic effect. Dye-sensitized nanocrystalline TiO_2 solar cells, which I have chosen for my research subject, are the latest promising electrochemical photovoltaic cells. In this chapter, a brief history and overview of the photoelectrochemical cells will be presented in Section 1. Then, the dye-sensitized nanocrystalline TiO_2 solar cell will be introduced in Section 2. Finally, unknown aspects of this new type of solar cell will be discussed in Section 3 in order to clarify the goal of my research project.

1.1. Brief History and Overview of Photoelectrochemical Cells

The photovoltaic effect is a fairly old discovery. In 1839 a French physicist, Edmond Becquerel, observed a voltage and a current when illuminating a silver electrode immersed in a chloride electrolyte.[1] The

Reproduced with permission of the copyright owner. Further reproduction prohibited without permission.

appearance of a voltage across the illuminated semiconductor/electrolyte interface (or p-n junction) is called the photovoltaic effect. However, it was not until 1955 that the origin of the photovoltaic phenomenon was understood with the work on germanium semiconductor electrodes done by Brattain and Garret.[2] During the next decade, the theory of semiconductor photoelectrochemistry was more fully developed at Bell Laboratories in the U. S. by Dewald,[3, 4] Boddy,[5, 6] and Turner;[7, 8] in Germany by Gerischer[9, 10] and Memming;[11, 12] and in Russia by Myamlin and Pleskov.[13]

1.1.1. Mechanism of Operation of Electrochemical Photovoltaic Solar Cells

A schematic representation of electrochemical photovoltaic cell is illustrated in Figure 1.1. The electrochemical photovoltaic cell consists of a semiconductor electrode, a counter electrode, and an electrolyte solution. Electrons in the valence band of the semiconductor are excited to the conduction band by absorbing photons of energy greater than the bandgap energy (E_g) of the semiconductor. Since the electrons (e^-) excited to the conduction band leave holes (h^+) in the valence band, electron-hole pairs are created in the semiconductor. In the case of n-type semiconductor (Figure 1.1), the electric field formed at the semiconductor/electrolyte interface drives electrons into the bulk of the semiconductor, to the back contact and then to the outer circuit. The holes are driven to the semiconductor/electrolyte interface under the electrical field, and oxidize the reduced species of the redox couple (R). At the counter electrode, the electrons reduce the oxidized species of the redox couple, resulting in no net charge in the semiconductor or

Reproduced with permission of the copyright owner. Further reproduction prohibited without permission.

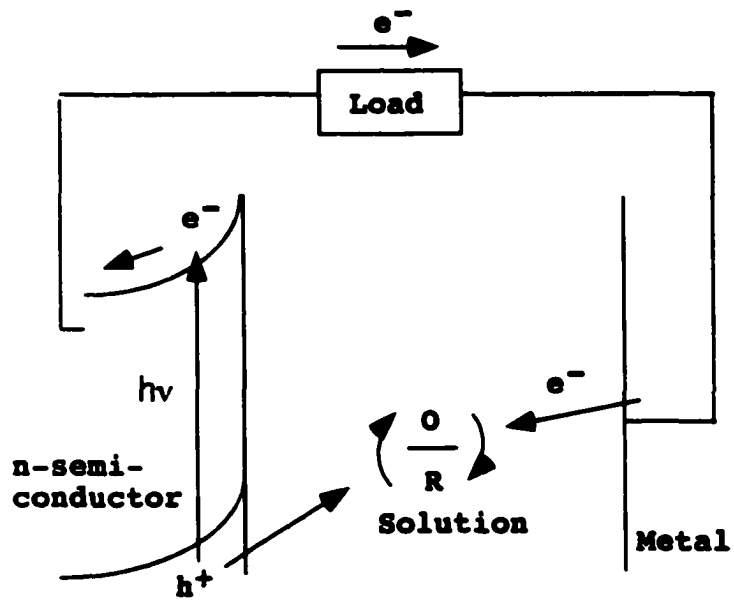

Figure 1.1. Schematic representation of an electrochemical photovoltaic cell with an n-type semiconductor electrode. R is the reduced species of the redox couple, and O is the oxidized species of the redox couple.

Reproduced with permission of the copyright owner. Further reproduction prohibited without permission.

solution. This is the mechanism of light-to-electricity conversion by an electrochemical photovoltaic cell.

1.1.2. Different Forms of Photoelectrochemical Cells

Electrochemical photovoltaic cells are one form of photoelectrochemical cells. All photoelectrochemical cells consist of a semiconductor electrode, a counter electrode (usually metal), and a redox electrolyte solution, and function based on the photovoltaic effect. The other forms of photoelectrochemical cells are photosynthetic cells and photocatalytic cells. Schematic representations of the different types of photoelectrochemical cells are presented in Figure 1.2.[14] In photovoltaic cells (Figure 1.2.a & b) the reaction that occurs at the counter electrode is the reverse of the reaction at the semiconductor electrode. The cell converts light to electricity ideally without any change in the solution composition or the electrode materials.

In photoelectrosynthetic cells (Figure 1.2. c & d) the reaction at the counter electrode is different from that at the semiconductor. The net cell reaction is driven by light in the non-spontaneous direction ($\Delta G > 0$), so that solar energy is stored as chemical energy. An example of this type of photoelectrochemical cells is n-$SrTiO_3$/ H_2O/Pt cell used for water splitting (Reaction 1).[15]

$$2H_2O \longrightarrow 2H_2 + O_2 \quad (\Delta G = 475\ kJmol^{-1}) \qquad \text{(Reaction 1)}$$

Photocatalytic cells (Figure 1.2 e & f) are similar to photosynthetic cells, yet the reaction is driven in the spontaneous direction ($\Delta G < 0$). In this type of

Reproduced with permission of the copyright owner. Further reproduction prohibited without permission.

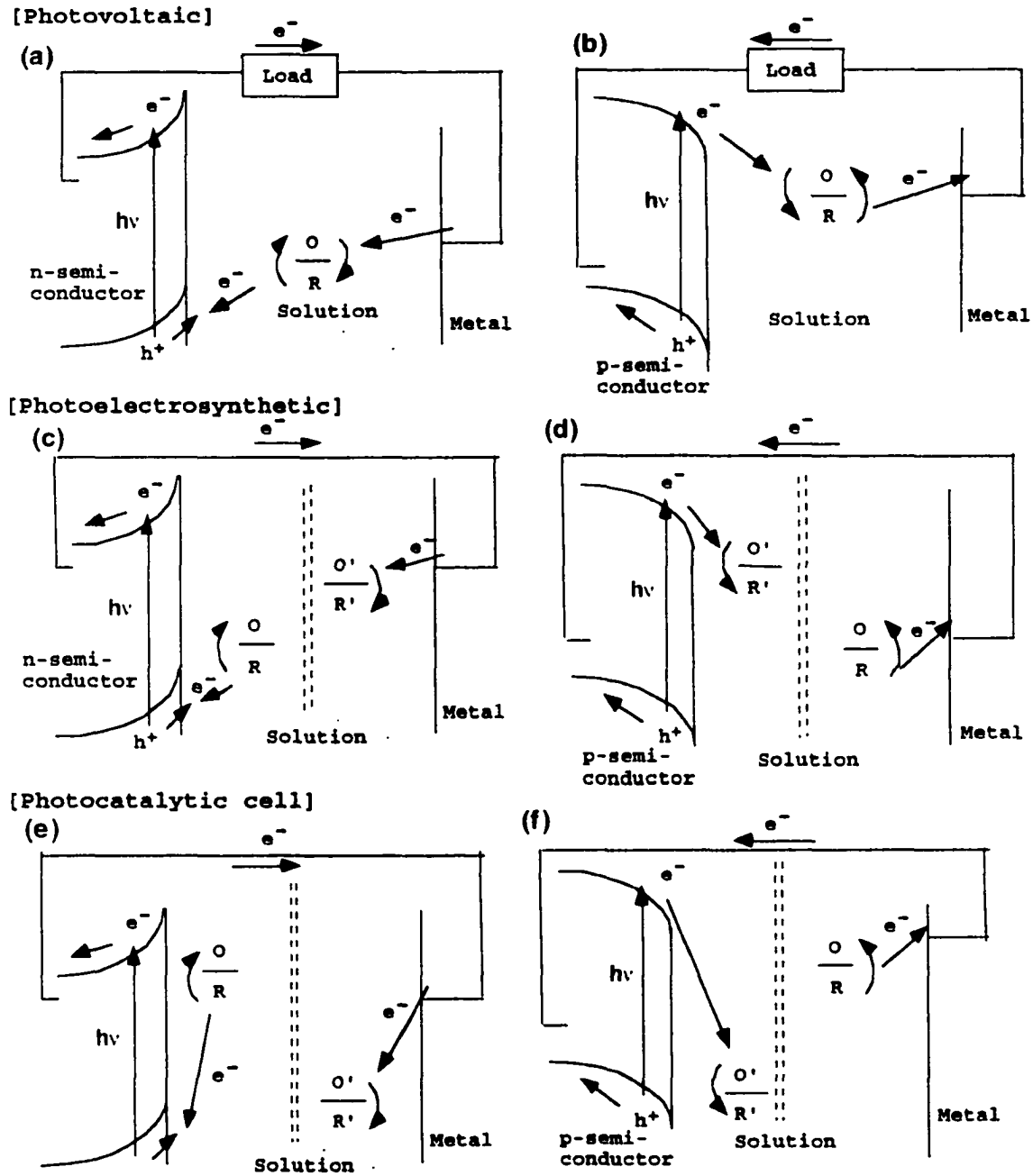

Figure 1.2. Schematic representation of different types of photo-electrochemical cells.[14]

Reproduced with permission of the copyright owner. Further reproduction prohibited without permission.

cell, light energy is used to overcome the activation energy of a very slow reaction. An example of this type of photoelectrochemical cell is n-TiO_2/CH_3OH/Pt cell for the decomposition of methanol (Reaction 2).[16]

$3O_2 + 2CH_3OH \longrightarrow 4H_2O + 2CO_2$ ($\Delta G = -1401$ kJmol^{-1}) (Reaction 2)

Photocatalytic cells are not useful for energy conversion but may be useful for photodegradation of pollutants.

1.1.3. Development of Practical Photoelectrochemical Cells

In 1972, the news of a possible practical application of photoelectrochemical cells energized the electrochemical community. Fujishima and Honda reported the decomposition of water to hydrogen and oxygen with an illuminated TiO_2 electrode.[17] This photoelectrochemical cell is a photoelectrosynthetic cell (Figure 1.2.c), which converts solar energy to chemical energy. An intrinsic disadvantage of large bandgap semiconductors, including TiO_2 (E_g = 3.2 eV), is their limited light utilization. As shown in Figure 1.3, the solar spectrum has less than 5 % of its energy in the UV region (> ~3.1 eV). Therefore, the maximum conversion efficiency of solar energy to electricity or stored energy with the large bandgap electrodes is less than 5 %.

To overcome this limitation, small bandgap semiconductors, for instance gallium arsenide (Eg = 1.4 eV)[18] and cadmium selenide (Eg = 1.7 eV),[19] were intensely studied. These small bandgap semiconductors have ideal bandgap values for the maximum utilization of the solar spectrum (Figure 1.3). However, these semiconductors tend to be unstable in an electrolyte solution under illumination. Because the minority carriers are usually highly reactive,

Reproduced with permission of the copyright owner. Further reproduction prohibited without permission.

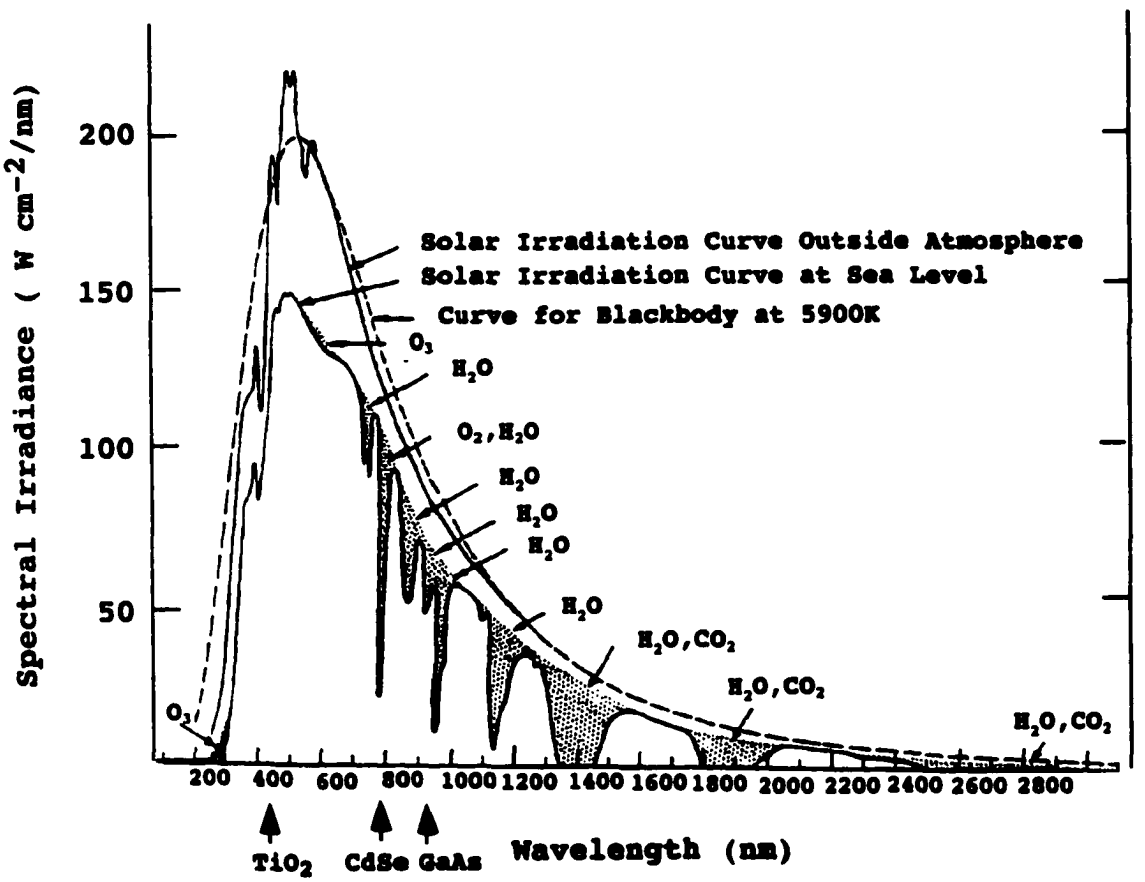

Figure 1.3. The solar spectrum and the bandgap of the semiconductors. The gray areas indicate the absorption by the molecules.

Reproduced with permission of the copyright owner. Further reproduction prohibited without permission.

these semiconductors themselves undergo oxidation or reduction reaction with the minority carriers. This process is known as photocorrosion. Reaction 3 describes the photocorrosion of n-type GaAs in a neutral solution under illumination.

$$GaAs + 6H_2O + 6h^+ \xrightarrow{h\nu} Ga(OH)_3 + As(OH)_3 + 6H^+ \quad \text{(Reaction3)}$$

Because the standard potential (E_0) for this reaction at pH 7 (-0.45 V vs. SCE) falls within the energy gap between the band edges (E_v = -0.23 V and E_c = -1.65 V vs. SCE at pH 7), the electrode is unstable with respect to the corrosion reaction.[18] Photocorrosion is one of the reasons why photoelectrochemical cells have not found practical applications for energy conversion.[20, 21] Yet, photocorrosion can be significantly reduced with redox reactions of suitable redox potential and reaction rate to compete effectively with the corrosion reaction. In several systems, a high degree of kinetic stability that overcomes the thermodynamic instability has been achieved.[22-25]

In addition to improving the stability, lowering of the production costs of the semiconductor is critical for the practical development of photoelectrochemical cells. The growth of bulk crystal semiconductors, such as with the Bridgeman and Czochralski methods, is slow and/or costly.[26, 27] One solution to the high production cost of bulk crystal semiconductors is the use of polycrystalline semiconductors. The production of polycrystalline materials usually requires less energy, less time, and less material. Those economical production techniques include chemical vapor deposition,[28] spray pyrolysis, pressure sintering,[29] chemical bath plating, and electroplating.[30] The

Reproduced with permission of the copyright owner. Further reproduction prohibited without permission.

efficiency of polycrystalline semiconductor electrodes is usually lower than single crystals because the probability of the recombination of electron-hole pairs is greater due to the presence of grain boundaries and other defects. Yet, some studies have revealed that polycrystalline semiconductor electrodes can achieve a relatively high percentage (60 to 85 %)[31, 32] of the efficiency of the single crystal counterpart.

1.1.4. Dye Sensitization of Large Bandgap Semiconductors

Extension of the utilization of the solar spectrum for photovoltaic cells made with wide bandgap semiconductors has been demonstrated by dye-sensitizing the semiconductors. A schematic representation of a dye-sensitized photovoltaic cell is shown in Figure 1.4. The dye molecules are chemically or physically adsorbed onto the semiconductor surface. Upon absorption of the light, the electronically excited dye molecules inject electrons into the conduction band of the semiconductor. The combination of dye and semiconductor needs to be chosen so that the energy level of the excited state of the dye is higher than the bottom of the conduction band ($\Delta V > 0.1$ eV).[33] A unique feature of the dye-sensitized system is that the functions of light absorption and charge collection are divided between the semiconductor and the dye. In other words, the semiconductor works solely as a charge transporter and collector, not as a light absorber. The advantage of the separation of the light absorption and the charge collection is that there is less possibility of photocorrosion of the semiconductor since minority carriers are not produced in the semiconductors.

Reproduced with permission of the copyright owner. Further reproduction prohibited without permission.

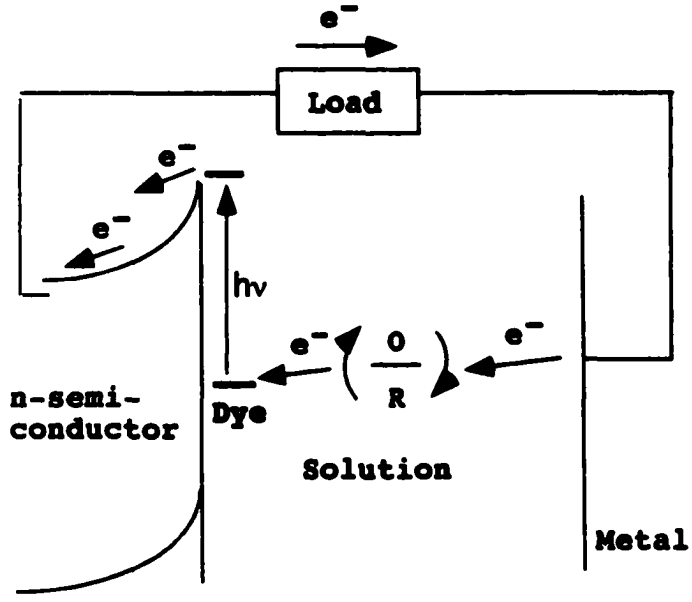

Figure 1.4. Schematic representation of a dye-sensitized photovoltaic cell with an n-type semiconductor.

Reproduced with permission of the copyright owner. Further reproduction prohibited without permission.

The enhancement of light absorption by dye-sensitization was, however, limited by the fact that only a monolayer of dye adjacent to the semiconductor surface can inject electrons efficiently into the semiconductor.[34] Single crystal semiconductors do not have large surface areas and so cannot adsorb large quantities of dye. Therefore, dye-sensitized solar cells were of only scientific interest until a breakthrough was achieved by the use of nanocrystalline semiconductor films.

1.1.5. Evaluation of Efficiency

There are several "efficiencies" used to evaluate photovoltaic cells. The most frequently used efficiencies are the incident photon to current efficiency (IPCE) and the overall efficiency for light to electricity conversion (η). The IPCE is defined as the following.

$$IPCE(\lambda) = \frac{\text{Number of collected electrons}}{\text{Number of incident photons}} \qquad \text{(Equation 1)}$$

The IPCE is obtained spectroscopically by measuring the photocurrent collected by illumination with monochromatic light and calculating IPCE with the following equation.

$$IPCE(\lambda) = \frac{\text{Photocurrent (A) x photon energy (V)}}{\text{Light intensity (W)}} \qquad \text{(Equation 2)}$$

The overall efficiency of light to electricity conversion (η) of a photovoltaic cell is evaluated with the following equation.

$$\eta = P_{out} / P_{in} \qquad \text{(Equation 3)}$$

Reproduced with permission of the copyright owner. Further reproduction prohibited without permission.

where P_{out} is the maximum output power of the cell, and P_{in} is the power of the incident light. The determination of the P_{out} is illustrated in Figure 1.5. Since the power delivered by the cell is the product of the photocurrent and the photovoltage, the maximum power that the cell can deliver (P_{out}) is represented with the maximum rectangle area (Figure 1. 5, the gray square: $I_{sc}' \times V_{oc}'$). P_{out} is described as the following using the concept called the fill factor.

$$P_{out} = I_{sc}' \times V_{oc}'$$

$$= (I_{sc}' / I_{sc}) \times (V_{oc}' / V_{oc}) \times I_{sc} \times V_{oc}$$

$$= ff \times I_{sc} \times V_{oc}$$

The fill factor (ff) is defined as the product of the ratio of the photocurrent for the maximum P_{out} to the short-circuit current (I_{sc}'/I_{sc}) and the ratio of the photovoltage for the maximum P_{out} to the open-circuit voltage (V_{oc}'/V_{oc}). The fill factor is an important element for the evaluation of the actual performance of the solar cell. In a photocurrent-voltage curve, the closer the curve is to rectangular shape, the greater the fill factor, consequently the higher the efficiency.

P_{in} is the incident solar energy and is defined as

$$P_{in} = \int (\text{flux}(\lambda) \times V(\lambda)) \, d\lambda \qquad \text{(Equation 4)}$$

where the flux (λ) is the photon flux at a given wavelength, and V (λ) is the energy of the photon of that wavelength.

Reproduced with permission of the copyright owner. Further reproduction prohibited without permission.

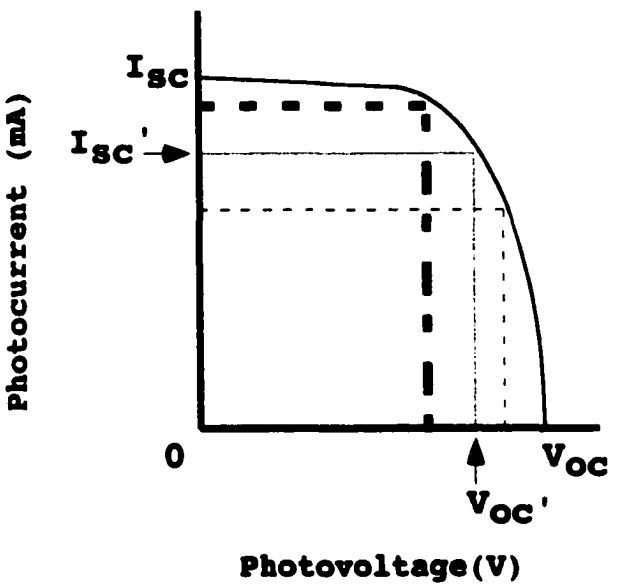

Figure 1.5. Relationship between the output power, the short-circuit current, the open-circuit voltage, and the fill factor.

Reproduced with permission of the copyright owner. Further reproduction prohibited without permission.

1.2. Dye-Sensitized Nanocrystalline TiO_2 Solar Cells

In 1991, O'Regan and Grätzel's[35] letter to *Nature* reinvigorated the community of photoelectrochemists. The paper reported a potentially commercially viable energy conversion efficiency for a dye-sensitized nanocrystalline TiO_2 film. Because of the high surface area of the nanocrystalline films and the very good absorption spectrum of the dye, this solar cell can utilize almost half of the solar energy flux and shows an exceptionally high efficiency for the conversion of incident photons to electrical current. The overall light-to-electron energy conversion efficiency was 7.9 % under one sun illumination and 12 % in diffuse daylight.[35] Furthermore, the potentially low production cost and the stability of the system[36] make practical applications of this device quite possible.

1.2.1. Operation and Energetics of the Dye-Sensitized Nanocrystalline TiO_2 Solar Cell

A schematic representation of the dye-sensitized nanocrystalline TiO_2 solar cell is shown in Figure 1.6. This system consists of a nanocrystalline TiO_2 film electrode on transparent conductive glass with the ruthenium-based dye chemically adsorbed to the TiO_2, a platinum coated conductive glass counter electrode, and I^- / I_3^- redox couple in acetonitrile. The reducing species (I^-) of the redox couple regenerates the dye molecules that are oxidized by injecting an electron into the TiO_2, and becomes I_3^- (Reaction 4), that is reduced at the counter electrode (Reaction 5).

$$3I^- + 2S^+ \longrightarrow I_3^- + 2S \qquad \text{(Reaction 4)}$$

Reproduced with permission of the copyright owner. Further reproduction prohibited without permission.

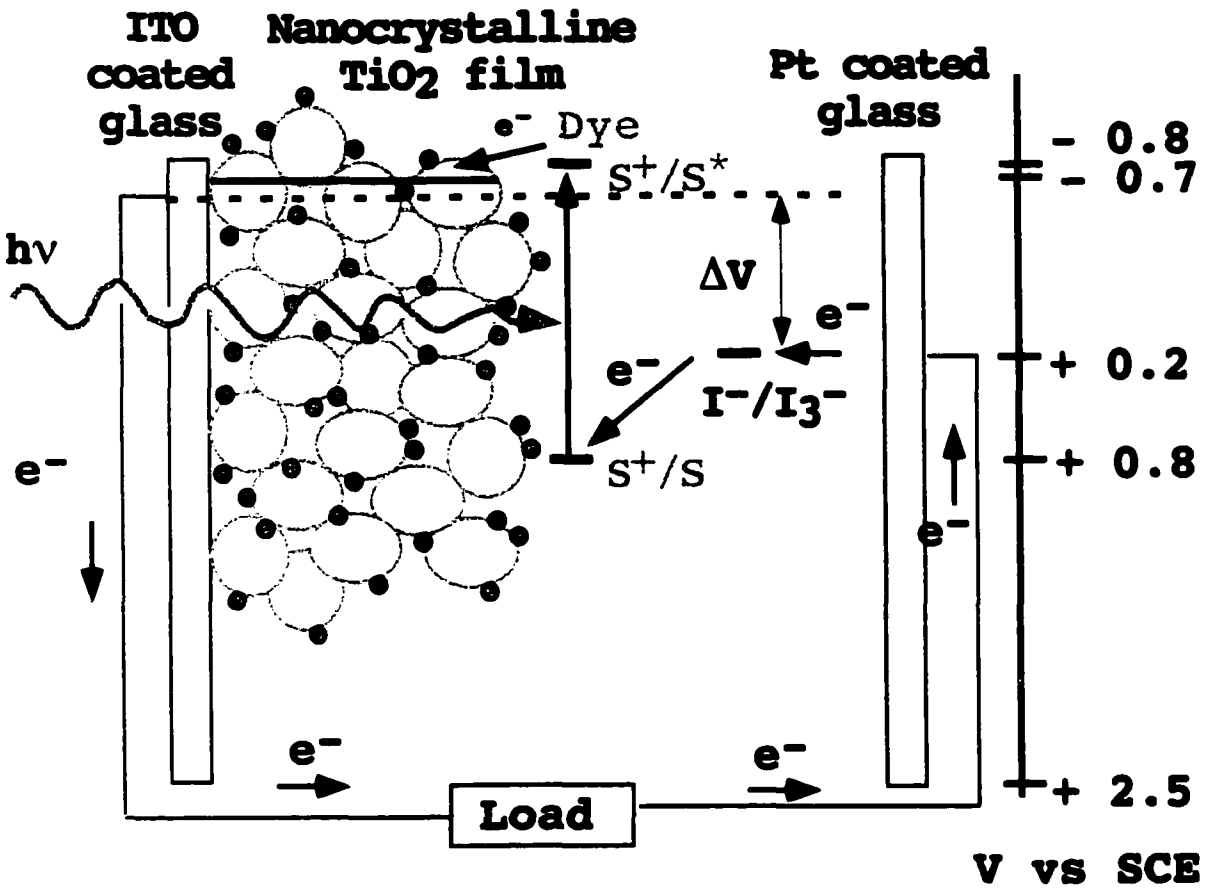

Figure 1.6. Schematic of sensitized nanocrystalline TiO_2 solar cell. Large circles: TiO_2 nanocrystallites; small black circles: dye molecules. Dashed line: quasi Fermi level of the TiO_2 film under illumination; line above the dashed line: conduction band of TiO_2 film. S: dye (sensitizer) at the ground state; S^+: oxidized dye; S^*: electronically excited dye.

Reproduced with permission of the copyright owner. Further reproduction prohibited without permission.

$$I_3^- + 2e^- \longrightarrow 3I^- \qquad \text{(Reaction 5)}$$

where S^+ is the oxidized form of the dye, and S is the dye in the neutral form in the ground state. In this way, the circuit is completed, and the electricity can be produced as long as light energy is provided.

The long wavelength absorption threshold for the dye adsorbed on TiO_2 is about 800 nm, corresponding to a potential of 1.6 eV. Since the oxidation potential of the dye (S^+/S) is 0.8 V vs SCE, the reduction potential (S^+/S^*) is calculated to be -0.8 V vs SCE. The potential of the conduction band edge is -0.7 vs SCE. Since the driving force necessary for the rapid vectorial electron transfer is about 0.1 eV,[33] photons of up to 800 nm wavelength can theoretically be utilized with this system. The cell voltage obtained under illumination corresponds to the difference (ΔV) between the quasi-Fermi level of the nanocrystalline TiO_2 film under illumination and the redox potential of the electrolyte (I^-/I_3^-), corresponding to a potential of 0.9 V. The photocurrent-voltage curve of the cell measured under AM 1.5 illumination is shown in Figure 1.7. AM stands for air mass and is a measure of the atmospheric path length of the sunlight, where AM 1 illumination is defined as the intensity of the solar illumination at the sea level at the equator during the equinoxes. Accordingly, AM 1.5 illumination is the intensity of the solar illumination at the sea level at latitude 48.2° N and 48.2° S during the equinoxes. Under this illumination the open circuit voltage was 0.72 V, the photocurrent was 18.3 mA cm^{-2}, and the fill factor was 0.73, yielding 10% overall efficiency of the cell.[33]

Reproduced with permission of the copyright owner. Further reproduction prohibited without permission.

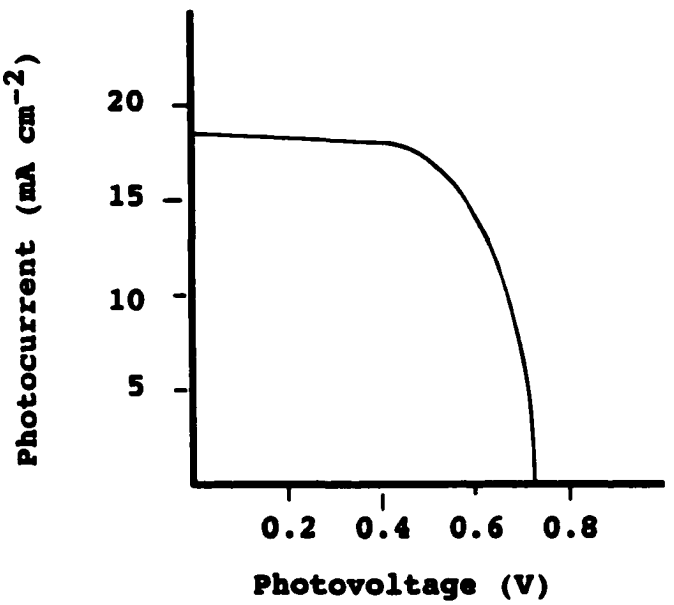

Figure 1.7. Photocurrent-voltage characteristics of the dye sensitized nanocrystalline TiO_2 solar cell.[37]

Reproduced with permission of the copyright owner. Further reproduction prohibited without permission.

In order to achieve an optimal efficiency, the energetics of the three components (dye, semiconductor, redox couple) in Figure 1.6 need to be varied. Substantial efforts have been made to synthesize new dyes for better spectral overlap with the solar spectrum and to find an alternative to the I^-/I_3^- redox couple. As shown in Figure 1.6, approximately 0.4 V is lost in the reduction of the photoexcited dye by the iodide ion since at least 0.1 to 0.2 V of overpotential is needed. Yet, so far no other redox couple has been found to be as efficient as the I^-/I_3^- for this device.

1.2.2. Nanocrystalline TiO_2 semiconductor electrodes

The distinguishing morphological properties of the nanocrystalline semiconductor electrodes are their high surface-to-volume ratio and porosity.[33] The mesoporous morphology of such a nanocrystalline semiconductor film is shown in Figure 1.8.[37] The scanning electron micrograph reveals that the TiO_2 film consists of three-dimensionally interconnected particles with an average diameter of approximately 15 nm. The thickness of the films is approximately 10 μm. The surface area was measured with N_2 adsorption and calculated using the Brunauer-Emmett-Teller (BET) isotherm.[38] The mesoporous film consisting of nanometer-sized TiO_2 particles has a 1000-fold greater surface area than its geometric area.[38] The pore size distribution was calculated as 18.5 to 19 nm by applying the Barret-Johner-Halenda (BJH) treatment to the isotherm.[38, 39] The porosity is defined as the following equation.

Reproduced with permission of the copyright owner. Further reproduction prohibited without permission.

Figure 1.8. Scanning electron micrograph of nanocrystalline TiO_2 film.[38]

Reproduced with permission of the copyright owner. Further reproduction prohibited without permission.

$$\text{porosity} = V_{pore} / (V_{pore} + V_{TiO_2})$$

where V_{pore} is the volume of the voids, and V_{TiO_2} is the volume of the TiO_2 particles. The porosity was calculated to be 0.64 for the neat film and 0.42 after dye adsorption, assuming the height of the dye is 1.4 nm.[37, 38]

The pore size of the nanocrystalline film also plays a critical role. The pore must be large enough so that the dye can reach the TiO_2 surface and the redox couple can diffuse through the pore without depleting the reducing species of the redox couple around the photooxidized dye. Yet, the pore size needs to be small to enhance the total surface area of the TiO_2 film. This high surface area is one of the most significant advantages of the nanocrystalline film. Only the first monolayer of adsorbed dye efficiently injects electrons into the semiconductor, and the light harvesting efficiency of a monolayer dye is very small (approximately 0.05 to 0.1 % of the incident light). Therefore, the enhancement of photon-to-electricity efficiency of the earlier flat semiconductor electrodes by dye-sensitization was severely limited because of the small surface areas of the electrodes.

One method of preparing nanocrystalline TiO_2 films is by spreading colloidal TiO_2 solution on a conductive transparent glass substrate and then sintering in air for 30 min at 450 °C in order to form electrical contact between the TiO_2 particles that allows charge transport to the substrate.[33] The colloidal TiO_2 dispersions are prepared by hydrolysis of titanium tetraisopropoxide, $(Ti(OCH(CH_3)_2)_4$, illustrated in Figure 1.9, or by dissolving commercial TiO_2 (P25, Degussa AG, Germany), which is produced by flame hydrolysis of $TiCl_4$ and consists of aggregated particles. The thickness of the films after annealing

Reproduced with permission of the copyright owner. Further reproduction prohibited without permission.

[Hydrolysis]

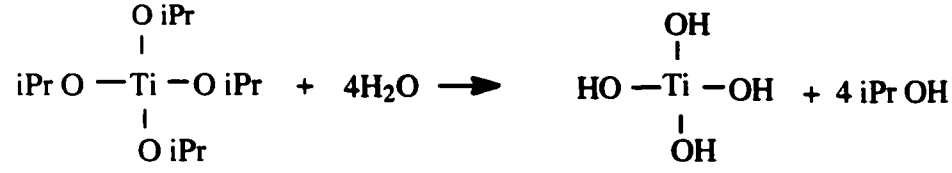

[Condensation]

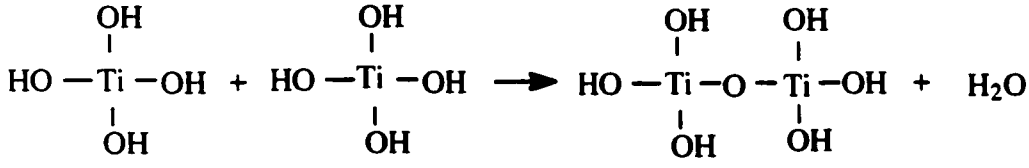

[Further Condensation]

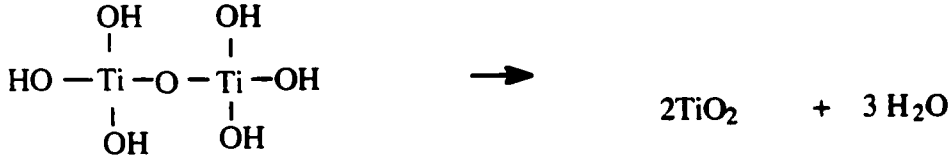

[Overall Reaction]

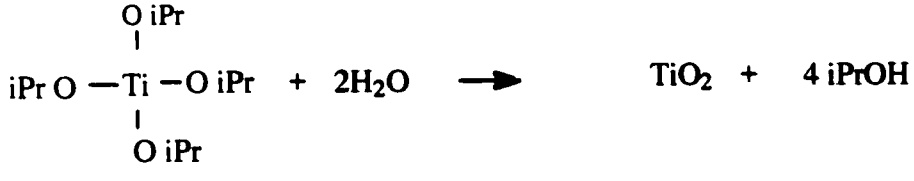

Figure1.9. TiO_2 synthesis by hydrolysis of titanium isopropoxide.

Reproduced with permission of the copyright owner. Further reproduction prohibited without permission.

was approximately 10 μm. X-ray diffraction analysis of the films produced by hydrolysis of titanium tetraisopropoxide revealed that they consist entirely of the anatase form of TiO_2[40] while the commercial TiO_2 is a mixture of ca. 30 % rutile form of TiO_2 and 70 % anatase.[41] As described above, the production of the semiconductor electrodes is a quite simple and low cost process. This is one of the major advantages of this solar cell.

The absorption spectrum of a TiO_2 nanocrystalline film prepared by hydrolysis of titanium tetraisopropoxide is shown in Figure 1.10.[40] The film was supported on conducting glass. The film exhibits the band edge transition at approximately 390 nm, corresponding to the bandgap of 3.2 eV. The absorption below 400 nm rising slowly to the red is due to free carrier absorption in the fluorine-doped tin oxide.[42]

1.2.3. Efficient sensitizer

The dye molecule most widely used for the sensitization of the nanocrystalline TiO_2 is *cis*-di(thiocyanato)bis(2,2'-bipyridyl-4,4'-dicarboxylate) ruthenium(II). The molecular structure of this dye is shown in Figure 1.11. The advantages of this dye for efficient sensitization are: a wide range of visible light absorption and a relatively long-lived excited state.[41] The absorption spectrum of the dye dissolved in ethanol is shown in Figure 1.12. This dye is often called "N3" in honor of the chemist, M. K. Nazeeruddin, who synthesized this efficient dye as his third sensitizer candidate. The maximum absorption coefficients of the N3/ethanol solution are reported to be

Reproduced with permission of the copyright owner. Further reproduction prohibited without permission.

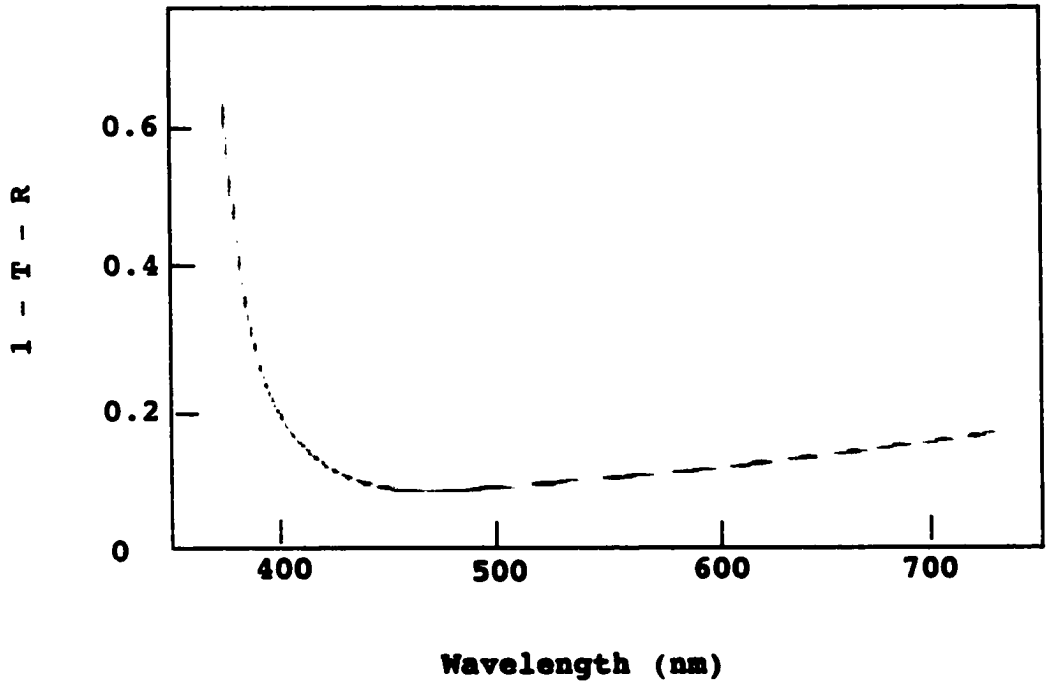

Figure 1.10. Absorption spectrum of a TiO_2 nanocrystalline film. [40]

Reproduced with permission of the copyright owner. Further reproduction prohibited without permission.

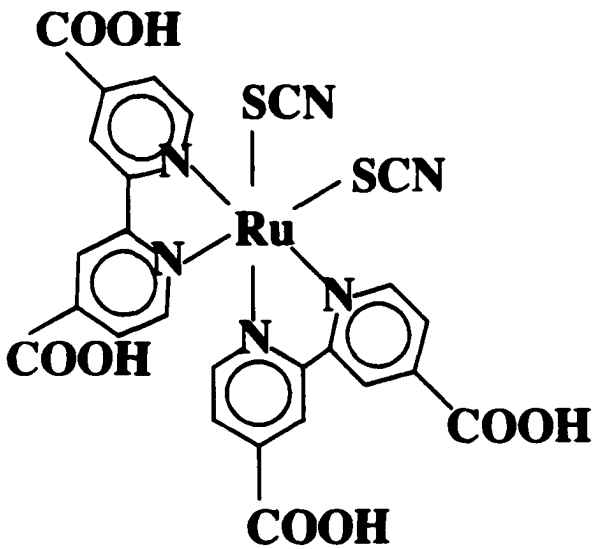

Figure 1.11. Molecular structure of the sensitizer of the nanocrystalline TiO_2.

Reproduced with permission of the copyright owner. Further reproduction prohibited without permission.

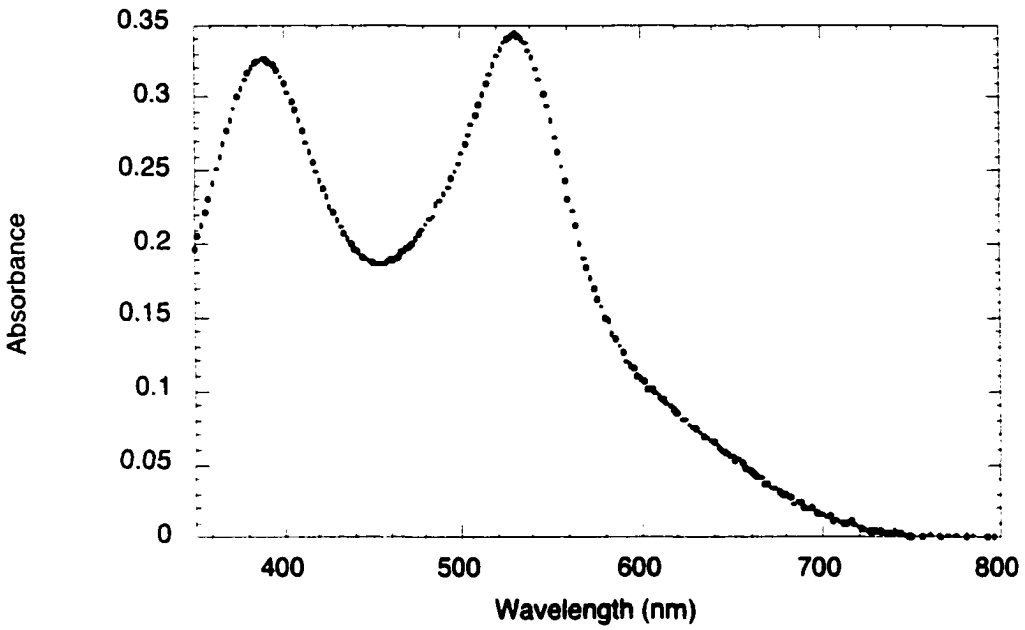

Figure 1.12. Absorption spectrum of N3 dissolved in ethanol. The concentration of the N3 solution is 2.4×10^{-5}M.

Reproduced with permission of the copyright owner. Further reproduction prohibited without permission.

$1.42 \times 10^4\ M^{-1}\ cm^{-1}$ at 534 nm, $1.40 \times 10^4\ M^{-1}\ cm^{-1}$ at 396 nm, and $3.12 \times 10^4\ M^{-1}\ cm^{-1}$ at 313 nm.[41] The absorption peaks in the visible region (at 534 nm) and near-UV region (at 396 nm) are assigned to two $t_2 \rightarrow \pi^*$ metal to ligand charge transfer (MLCT) transition, and the absorption peak in the UV region (at 313 nm) is assigned to $\pi \rightarrow \pi^*$ intraligand transition.[41] The carboxylate groups are chemically bound to the surface, forming a strong electronic coupling between the N3 and the TiO_2. The molecular orbital diagram for the N3 attached to the TiO_2 and the electron transfer from the N3 to the TiO_2 are illustrated in Figure 1.13.

In addition to the wide range of the visible light absorption, another advantage of N3 is its much greater forward electron transfer (i.e. injection) rate (k_f) compared to the backward electron transfer rate (k_b). The backward transfer involves the recapture of electrons injected into the TiO_2 conduction band by the oxidized N3 and the oxidized half of the redox couple (I_3^-). These kinetics measurements were conducted by using a flash photolysis method, which is described later. The ratio of the injection to recapture rates is greater than 10^3. The rationale for the much smaller rate of back transfer to the oxidized N3 is the less favorable overlap of the molecular orbitals involved in the back transfer with the wave function of the conduction band than those involved in the injection transfer.[33] The carboxylate groups interact directly with the surface Ti^{4+} ions, forming good electronic coupling of the π^* wave function with the titanium 3d orbitals of the conduction band of the TiO_2. Therefore, the electron injection from the excited sensitizer into the semiconductor is extremely rapid, less than a picosecond. On the other hand,

Reproduced with permission of the copyright owner. Further reproduction prohibited without permission.

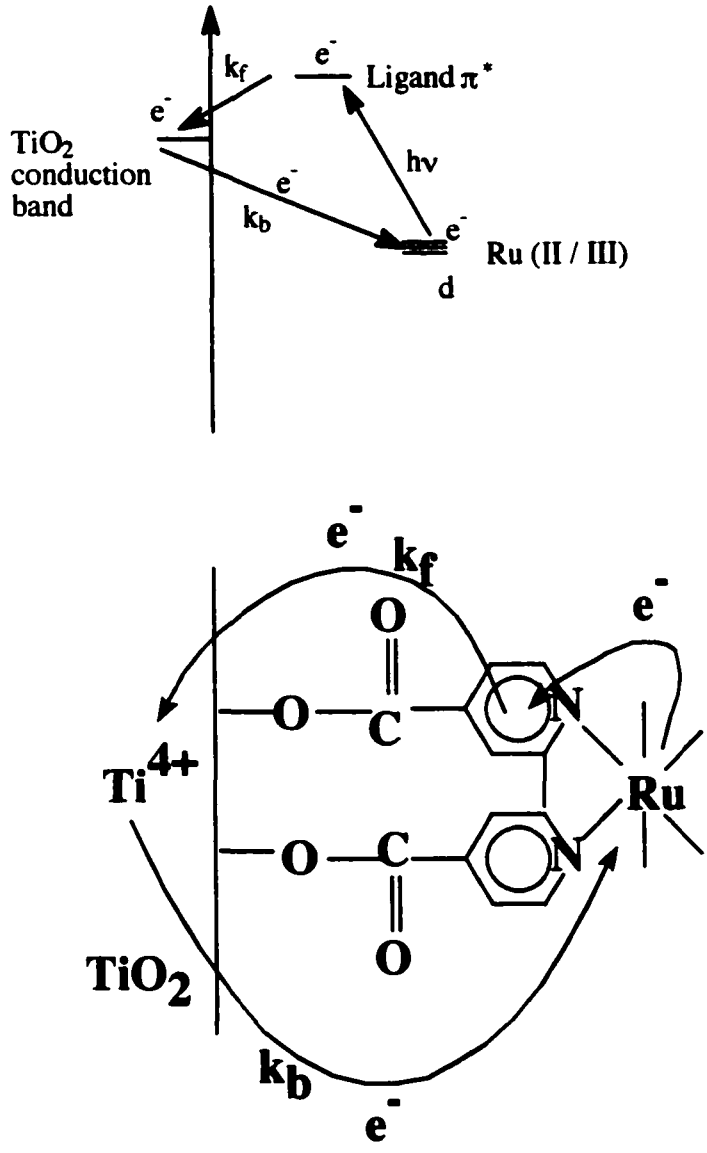

Figure 1.13. The molecular orbital diagram for the N3 attached to the TiO_2 surface and the charge transfer between them.[33]

Reproduced with permission of the copyright owner. Further reproduction prohibited without permission.

the back transfer of the electrons to the oxidized ruthenium complex involves a d orbital localized on the ruthenium metal whose electronic overlap with the TiO_2 conduction band is small. Furthermore, the wave function of ruthenium contracts upon oxidation from Ru^{2+} to Ru^{3+}, resulting in further reduction of electronic coupling.

The photocurrent action spectrum (IPCE spectrum) of the nanocrystalline TiO_2 film sensitized with the N3 is shown in Figure 1.14.[41] The cell was constructed in a sandwich configuration. The photocurrent was obtained at short circuit. The TiO_2 film was illuminated from the back side of the nanocrystalline film. As seen in Figure 1.14, the IPCE of this cell is impressive particularly in the wavelength range between 510 and 570 nm (85 to 90 %).[41] A sensitizer for solar cells have to be stable for many years. The N3 sustained more than 5×10^7 redox cycles without noticeable loss of performance, corresponding to approximately 10 years of continuous operation in natural sunlight.[35, 36]

1.2.4. Charge Transport in Nanocrystalline TiO_2 Film

An intriguing feature of the nanocrystalline TiO_2 film is the high efficiency of the transport and collection of photoinjected electrons through the TiO_2 particles and the grain boundaries between the particles.[41, 43] For bulk semiconductors, the space charge layer provides the driving force for charge transport through the semiconductor. However, due to their small size

Reproduced with permission of the copyright owner. Further reproduction prohibited without permission.

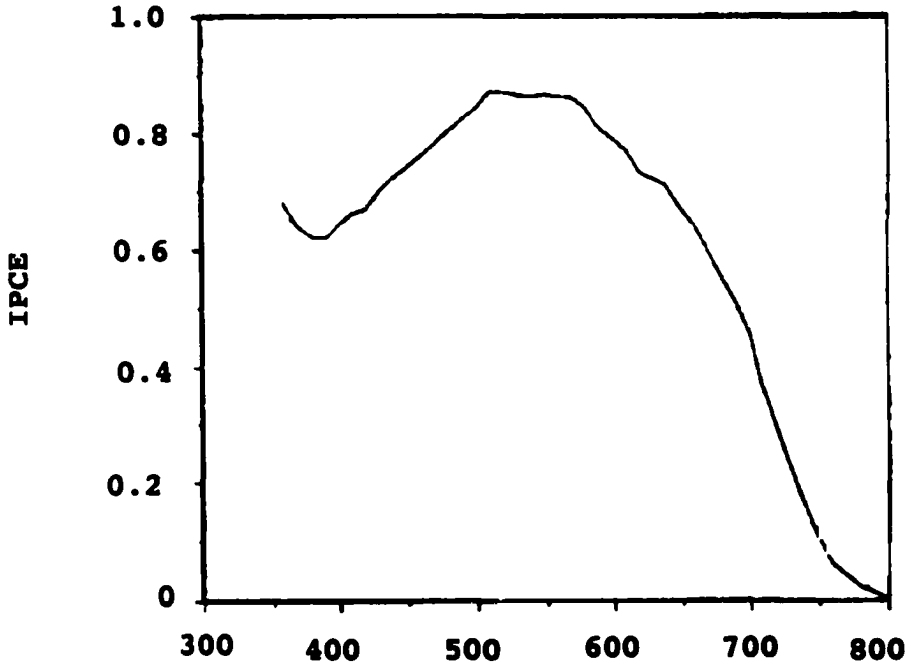

Figure 1.14 Photoaction spectrum of a nanocrystalline TiO_2 film sensitized with N3. The nanocrystalline TiO_2 film was prepared from a colloidal solution of P25 (Degussa) on a transparent conductive glass. The electrolyte was 0.03 M I_2 and 0.3 M LiI in acetonitrile. The counter electrode was platinum coated conducting glass.[41]

Reproduced with permission of the copyright owner. Further reproduction prohibited without permission.

there is no significant space charge layer formation in nanocrystalline semiconducting films. The transfer of charge carriers between the semiconductor and the electrolyte is necessary for the formation of a space charge layer. Nano-sized particles are too small to contain enough charged species to form a space charge layer.[33] Therefore, diffusion is considered to be the driving force for charge transport through the semiconductor films. The electron concentration profile inside of the film has been calculated and is shown in Figure 1.15.[44] The steep electron concentration gradient near the back contact provides the driving force for electrons to flow toward the back contact. Therefore, the assumption that the driving force of electron transport is solely diffusion seems to be justified for the nanocrystalline film.

Reproduced with permission of the copyright owner. Further reproduction prohibited without permission.

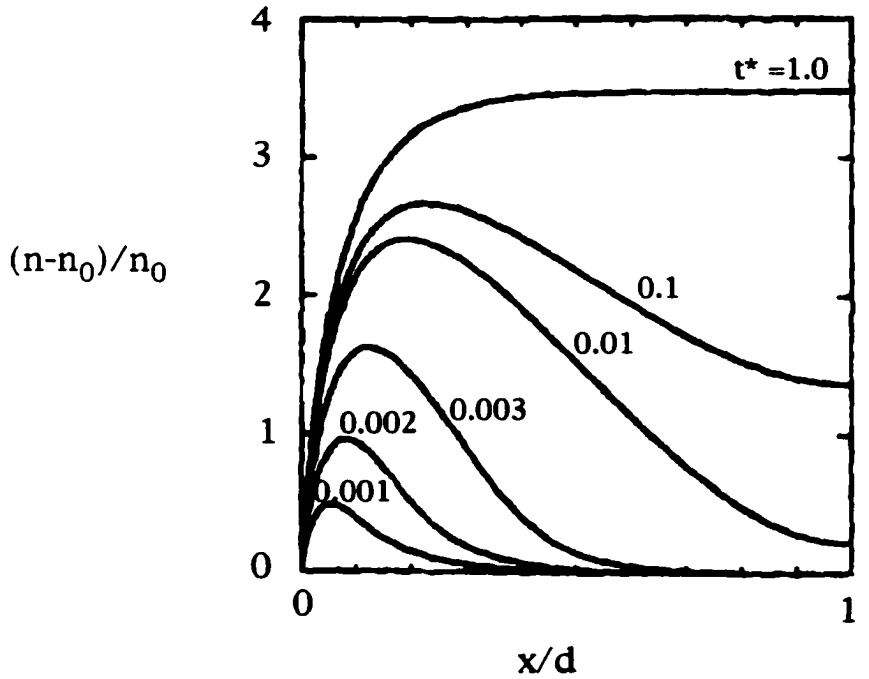

Figure 1.15. Electron concentration profile inside of the dye-sensitized nanocrystalline TiO_2 film.[44] n is the electron density under illumination. n_0 is the electron in the dark. x is the distance from the back contact. d is the thickness of the TiO_2 film. t* is dimensionless time.

This figure was constructed based on a numerical solution for a transport equation for electrons, which is obtained using a forward time central space (FTCS) algorithm. The transport equation for electrons was obtained as the following. Carrier transport in the semiconductor film is described as the following.[44]

$$\frac{\partial n}{\partial t} = \frac{1}{e}\frac{\partial J}{\partial x} + G - R \qquad \text{(equation 1)}$$

where n is the electron density under illumination, J is current density in the film, t is time, x is the distance from the back contact, and G and R are the carrier generation rate and recombination rate, respectively. For the dye-sensitized nanocrystalline TiO_2 film, the carrier generation rate G can be written as:

Reproduced with permission of the copyright owner. Further reproduction prohibited without permission.

$$G = \frac{\partial(\Gamma \times LHE)}{\partial x} \qquad \text{(equation 2)}$$

where Γ is the photon flux, LHE is light harvesting efficiency, that is a fraction of absorbed photons to incident photons, and written as the following.

$$LHE = 1 - 10^{-\alpha x} \qquad \text{(equation 3)}$$

where α is the wavelength-dependent absorption coefficient of the dye-sensitized film. By substituting equation 3 into equation 2,

$$G = \Gamma\alpha \exp(-\alpha x) \qquad \text{(equation 4)}$$

Since the dye-sensitized nanocrystalline TiO_2 film is considered to be lack of a space charge layer, the contribution of migration to the current density is ignored. Then, J is written as the following,

$$J = eD \frac{\partial n}{\partial x} \qquad \text{(equation 5)}$$

where D is the diffusion coefficient of electron. Assuming that the recombination is negligible, which will be explained to be a fair assumption in later chapter, the time-dependent transport equation for electrons is obtained by substituting equations 4 and 5 into equation 1.

$$D \frac{\partial^2 n(x, t)}{\partial x^2} - \frac{\partial n(x, t)}{\partial t} + \Gamma\alpha \exp(-\alpha x) = 0 \qquad \text{(equation 6)}$$

The diffusion coefficient D for electrons in the film is assumed to be proportional to the electron concentration, and written as the following,

$$D = D_0 \frac{n(x, t)}{n_0} \qquad \text{(equation 7)}$$

where D_0 is the diffusion coefficient in the dark, and n_0 is the electron density in the dark. Substituting equation 7 into equation 6, the transport equation for electrons becomes,

$$\frac{\partial}{\partial x}\left(\frac{D_0 n(x, t)}{n_0}\frac{\partial(n(x, t))}{\partial x}\right) - \frac{\partial n(x, t)}{\partial t} + \Gamma\alpha \exp(-\alpha x) = 0$$

(transport equation for electrons)

Reproduced with permission of the copyright owner. Further reproduction prohibited without permission.

1.2.5. Kinetics of the reactions in the dye-sensitized nanocrystalline TiO_2 solar cell.

The charge separation in the dye-sensitized nanocrystalline solar cell is controlled by the kinetics of the charge transfer between the dye, semiconductor, and the redox couple. The electron transfer rates in this system are shown in Figure 1.16. Following the light absorption by the dye (Figure 1.16 (1)), the time scale of the electron injection into the TiO_2 conduction band (Figure 1.16 (2)) was measured to be in the picosecond range by flash photolysis.[45, 46] In this experiment colloidal TiO_2 with adsorbed dye was pulsed with a 450 nm dye laser, then the absorbance change was examined. A bleaching signal at 530 nm, absorption peaks at 380 nm and 650 nm were observed and assigned to the dye ground state, the dye cation radical, and the conduction band electrons, respectively. The absorbance changes observed immediately after the laser pulse indicate that the electron injection from the dye into the conduction band happens during and/or within the laser pulse, in a picosecond time scale. Also, a much shorter time scale for the electron has been reported by monitoring the transient absorption signal at 1100 nm after excitation at 415 nm and 550 nm for an N3-covered colloidal TiO_2 electrode in ultrahigh vacuum.[47] This signal was assigned to the intraband absorption of the injected electrons. From the less than 25 fs rise time of this signal the electron injection rate was analyzed to be in femtosecond range.

The subsequent recombination of the conduction band electron with the oxidized dye (Figure 1.16 (3)) was observed to occur over several microseconds

Reproduced with permission of the copyright owner. Further reproduction prohibited without permission.

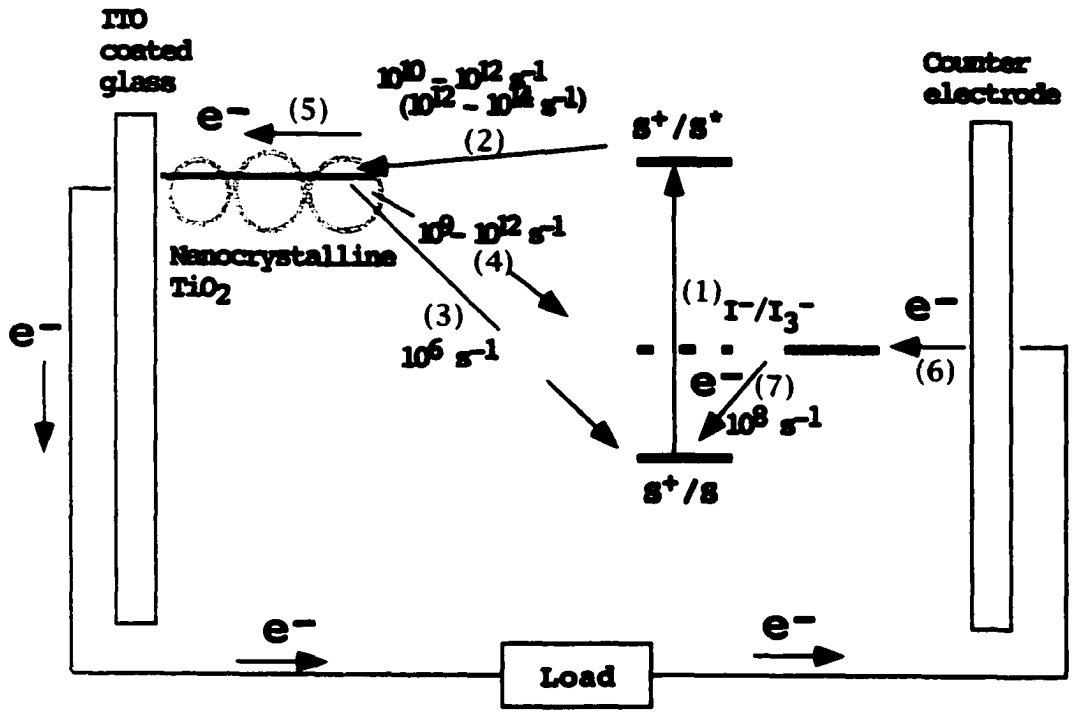

Figure 1.16. Rates for the electron transfer reactions in the dye-sensitized nanocrystalline TiO_2 electrode.[33] Step (4): 10^{-11} to 10^{-9} A cm^{-2}; Step (6): 10^{-2} to 10^{-1} A cm^{-2}.

Reproduced with permission of the copyright owner. Further reproduction prohibited without permission.

by monitoring the time dependence of the absorbance at the three different wavelengths. Another recombination process is the reduction of I_3^- in the electrolyte by conduction band electrons (Figure 1.16 (4)). The exchange current density of this process has been measured to be 10^{-11} to 10^{-9} A cm^{-2}, depending on the electrolyte.[48] This exchange current density corresponds to the electron back transfer rate of 10^{9} to 10^{12} s^{-1} for a nanocrystalline TiO_2 film with 1 cm x 0.5 cm x 10μm dimensions. This recombination rate of 10^{10} to 10^{12} s^{-1} is competitive with the injection rate of 10^{10} to 10^{12} s^{-1} that was reported by Grätzel et al. On the other hand, the recombination rate of 10^{10} to 10^{12} s^{-1} is negligible if the injection rate is in femtosecond time scale as reported by Willig et al.

The electron transport in the nanocrystalline TiO_2 film to the back contact (Figure 1.16 (5)) is significantly slower than in single crystal TiO_2.[49-51] The decay of the photocurrent from UV excitation of the TiO_2 film with a nanosecond pulse laser was observed to be in the millisecond to second range.[52] The exchange current density for reduction of triiodide at the counter electrode (Figure 1.16 (6)) has been measured to be 10^{-2} to 10^{-1} A cm^{-2}.[53] This exchange current density is equivalent to an electron transfer rate of 10^{16} to 10^{17} s^{-1} for a 1 cm^2 counter electrode. Finally, the regeneration of the oxidized dye by iodide ion (Figure 1.16 (7)) occurs in a time scale of 10^{-8} s.[41]

As presented above, the high efficiencies and high stability of the dye-sensitized nanocrystalline TiO_2 solar cell can be attributed to the favorable kinetics for the desired pathway of the photoexcited electron.

Reproduced with permission of the copyright owner. Further reproduction prohibited without permission.

1.3. Unknown Aspects of the Dye-Sensitized Nanocrystalline TiO_2 Solar Cells

Despite progress in improving the efficiency[35, 41] and stability[36] of the dye-sensitized nanocrystalline TiO_2 solar cells, there are many unknown aspects of their operation. The goal of this project is investigating some of these unknown aspects. The first aspect is the dye/semiconductor interface. Recent publications have discussed some theoretical views of the binding of the ruthenium complex sensitizers to the anatase surface.[37, 54, 55] Yet, very few experimental data that provide information on the dye/semiconductor interface have been published.[56] Our approach to this unexplored aspect is to examine the relationship between the binding geometry, dye coverage, and the efficiency of photon to electricity conversion. We would like to answer the following questions to provide information on the dye/semiconductor interface (Figure 1.17, Aspect(1)). 1) How does dye coverage affect the efficiency of photon to electricity conversion? 2) How does dye coverage affect the binding geometry of the dye? 3) How does the binding geometry affect the efficiency?

The second aspect relates to the diffusion of the redox species in the nanocrystalline film. The limitation of the regeneration of oxidized N3 due to the restricted diffusion of the regenerating species (I^-) in the matrix of the nanoporous TiO_2 film has been overlooked. A study with a mathematical model showed that the diffusion of I^- was affected very little by the presence of the solid nanocrystalline TiO_2.[38] However, we expect that the tortuous path for I^- diffusion through the TiO_2 nanocrystalline film will considerably hinder the

Reproduced with permission of the copyright owner. Further reproduction prohibited without permission.

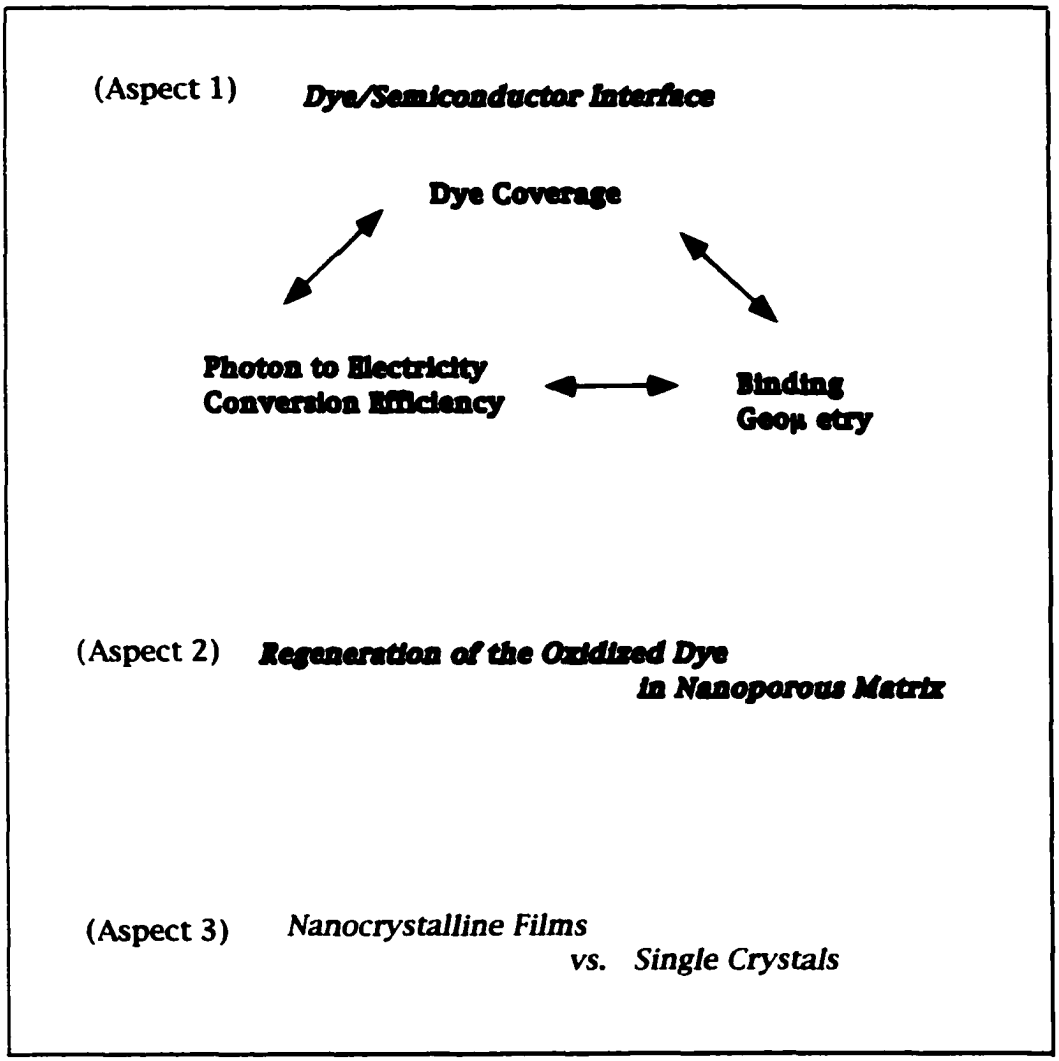

Figure 1.17. Goals of this project.

Reproduced with permission of the copyright owner. Further reproduction prohibited without permission.

diffusion. This aspect is addressed with the results of the investigation on the relationship between the dye coverage and the conversion efficiency.

The third aspect is the correlation of the enhanced efficiency of the dye-sensitized nanocrystalline TiO_2 to the increased surface area compared to a single crystal system. In other words, is the enhancement in the efficiency proportional to the increase in the surface area? If so, is the enhanced efficiency simply an attribute of the increased surface areas? Is there any special effect due to the nanometer size structure?

In the next chapter (Chapter 2), the experiments using nanocrystalline TiO_2 films are reported, and aspects of the dye/semiconductor interface and the regeneration of oxidized dye are discussed. In Chapter 3, the experiments utilizing natural anatase single crystals are presented, and a comparison of nanocrystalline films and single crystals is presented. In the last chapter (Chapter 4), the data taken with surface imaging techniques are shown in an attempt to provide direct information on the dye/semiconductor interface.

Reproduced with permission of the copyright owner. Further reproduction prohibited without permission.

References cited in Chapter 1

1. E. Becquerel. *Acad. Sci. Paris*, **9**, 561 (1839).

2. W. H. Brattain and C. G. B. Garrett. *Bell System Tech. J.*, **34**, 129 (1955).

3. J. F. Dewald. *Bell System Tech. J.*, **39**, 615 (1960).

4. J. F. Dewald. in Semiconductors, B. Hannay, ed., 727. Reinhold, NY (1957).

5. P. J. Boddy and W. H. Brattain. *J. Electrochem. Soc.*, **109**, 1053 (1962).

6. P. J. Boddy. *J. Electrochem. Soc.*, **115**, 199 (1968).

7. D. R. Turner. *J. Electrochem. Soc.*, **108**, 561 (1962).

8. D. R. Turner. *J. Electrochem. Soc.*, **103**, 252 (1956).

9. H. Gerischer. in Advances in Electrochemistry and Electrochemical Engineering. P. Delahay, ed., 139. Interscience. New York (1961).

10. H. Gerischer. in Physical Chemistry-An Advanced Treatise. H. Eyring. D. Henderson and W. Jost. ed., 463. Academic Press. New York (1970).

11. R. Memming and G. Schwandt. *Electrochem Acta.*, **13**, 1299 (1968).

12. R. Memming. *J. Electrochem. Soc.*, **116**, 785 (1969).

13. V. A. Myamlin and Y. Pleskov. *Electrochemistry of Semiconductors*. Plenum. New York (1967).

14. A. Bard and L. Faulkner. *Electrochemical Methods*. 636. Wiley. New York (1980).

15. M. Wrighton. A. Ellis. P. Wolczanski. D. Morse. H. Abrahamson. and D. Ginley. *J. Am. Chem. Soc.*, **98**, 2774 (1976).

16. G. Porter. in a Source Book in Photochemistry. J. D. Coyle. R. R. Hill and D. R. Roberts. ed., 355. Open University Press. Milton Keynes (1982).

17. A. Fujishima and K. Honda. *Nature*, **238**, 37 (1972).

Reproduced with permission of the copyright owner. Further reproduction prohibited without permission.

18. K. W. Frese, in Semiconductor Electrodes, H. O. Finklea, ed., 373, Elsevier Science, New York (1988).

19. R. D. Rauh, in Semiconductor Electrodes, H. O. Finklea, ed., Elsevier, New York (1987).

20. H. Gerischer, *J. Electroanal. Chem.*, **82**, 133 (1977).

21. A. J. Bard and M. S. Wrighton, *J. Electrochem. Soc.*, **124**, 1708 (1977).

22. A. B. Parkinson, A. Heller, and B. Miller, *J. Electrochem. Soc.*, **126**, 955 (1979).

23. A. Heller, B. Miller, and F. Thiel, *Appl. Phys. Lett.*, **38**, 282 (1981).

24. G. Kline, K. Kam, D. Canfield, and B. A. Parkinson, *Solar Energy Materials*, **4**, 301 (1981).

25. G. Kline, K. Kam, R. Ziegler, and B. A. Parkinson, *Solar Energy Materials*, **6**, 337 (1982).

26. K. Bachmann and E. Buehler, *J. Electrochem. Soc.*, **121**, 835 (1974).

27. G. W. Isler, *J. Crystal Growth*, **54**, 16 (1981).

28. M. A. Russak and J. Reichman, *J. Electrochem. Soc.*, **129**, 542 (1982).

29. B. Miller, A. Heller, M. Robbins, S. Menezes, K. C. Chang, and J. Thompson, *J. Electrochem. Soc.*, **124**, 1019 (1977).

30. M. Tomkiewicz, I. Ling, and W. S. Parsons, *J. Electrochem. Soc.*, **129**, 2016 (1982).

31. A. Heller, H. Lewerenz, and B. Miller, *Bunsenges Phys. Chem.*, **84**, 592 (1980).

32. M. Russak, J. Reichman, C. Creter, and J. De-Garlo, *Fifth Photoelectrochemical Cell Contractors' Review*, ed., Golden, Colorado (1982).

33. A. Hagfeldt and M. Grätzel, *Chem. Rev.*, **95**, 49 (1995).

34. A. Mills and S. Le Hunte, *J. Photochem. Photobiol. A.*, **108**, 1 (1997).

35. B. O'Regan and M. Grätzel, *Nature*, **353**, 737 (1991).

36. O. Kohle, M. Grätzel, A. F. Meyer, and T. B. Meyer, *Advanced Materials*, **9**, 904 (1997).

Reproduced with permission of the copyright owner. Further reproduction prohibited without permission.

37. V. Shklover, M.-K. Nazeeruddin, S. M. Zakeeruddin, C. Barbé, A. Kay, T. Haibach, W. Steurer, R. Hermann, H.-U. Nissen, and M. Grätzel, *Chem. Mater.*, **9**, 430 (1997).

38. N. Papageorgiou, C. Barbé, and M. Grätzel, *J. Phys. Chem. B*, **102**, 4156 (1998).

39. P. C. Heimenz, *Principles of Colloid and Surface Chemistry*, 2 nd, Dekker, New York (1986).

40. B. O'Regan, J. Moser, M. Anderson, and M. Grätzel, *J. Phys. Chem.*, **94**, 8720 (1990).

41. M. K. Nazeeruddin, A. Kay, I. Rodicio, R. Humphry-Baker, E. Müller, P. Liska, N. Vlachopoulos, and M. Grätzel, *J. Am. Chem. Soc.*, **115**, 6382 (1993).

42. E. Shanthi, A. Banrjee, and K. L. Chopra, *Thin Solid Films*, **88**, 93 (1982).

43. A. Hagfeldt, U. Björkstén, and S.-E. Lindquist, *Sol. Energy Mat. Sol. Cells*, **27**, 293 (1992).

44. F. Cao, G. Oskam, J. G. Meyer, and P. Searson, *J. Phys. Chem.*, **100**, 17021 (1996).

45. J. Desilvestro, M. Grätzel, K. L., J. Moser, and J. Augustynski, *J. Am. Chem. Soc.*, **107**, 2988 (1985).

46. N. Vlachopoulos, P. Liska, J. Augustynski, and G. M., *J. Am. Chem. Soc.*, **110**, 1216 (1988).

47. T. Hannappel, Burfeindt, B. and Willig, F., *J. Phys. Chem.*, **101**, 6799 (1997).

48. G. Smestad, *Sol. energy Mater. Solar Cells*, **32**, 273 (1994).

49. F. W. Schmidlin, *Phys. Rev.*, **16**, 2362 (1977).

50. K. Schwarzburg and F. Willig, *Appl. Phys. Lett.*, **58**, 2520 (1991).

51. L. M. Peter and D. Vanmaekelberg, *Adv. Electrochem. Sci. Eng.*, **6**, 77 (1999).

52. U. Björkstén, A. Hagfeldt, J. Moser, and G. M., *Book of Abstracts*, ed., 209, Interlaken, Switzerland (1994).

53. N. Papas and M. Grätzel, *Manuscript in preparation*

Reproduced with permission of the copyright owner. Further reproduction prohibited without permission.

54. V. Shklover, T. Haibach, B. Bolliger, M. Hochstrasser, M. Erbudak, H.-U. Nissen, S. M. Zakeeruddin, M. K. Nazeeruddin, and M. Grätzel, *J. Solid State Chem.*, **132**, 60 (1997).

55. V. Shklover, Y. E. Ovchinnikov, L. S. Braginsky, S. M. Zakeeruddin, and M. Grätzel, *Chem. Mater.*, **10**, 2533 (1998).

56. K. S. Finnie, J. R. Bartlett, and J. L. Woolfrey, *Langmuir*, **14**, 2744 (1998).

Reproduced with permission of the copyright owner. Further reproduction prohibited without permission.

Preface to Chapter Two

In this chapter, the dye adsorption behavior and the relationship between photon to current efficiency and the dye coverage are investigated in nanocrystalline films to examine these relationships in the actual solar cell. I am presenting my first publication as chapter 2 of my dissertation. This paper was published in the Journal of the Electrochemical Society, vol. 146, p 4559-4564 (1999).

Reproduced with permission of the copyright owner. Further reproduction prohibited without permission.

CHAPTER TWO

The Adsorption Behavior of a Ruthenium Based Sensitizing Dye to Nanocrystalline TiO_2 : Coverage Effects on the External and Internal Sensitization Quantum Yields

ABSTRACT

The adsorption of the ruthenium based dye molecules, *cis*-di(thiocyanato)bis(2,2'-bipyridyl-4,4'-dicarboxylate)ruthenium(II) (N3), to nanocrystalline TiO_2 (70 % anatase and 30 % rutile) was studied. Adsorption and desorption kinetics were measured, then adsorption isotherm and "desorption isotherm" were obtained. A two-step dye adsorption mechanism is postulated where initial binding is with one carboxyl group, with subsequent binding of two carboxyl groups. Dye (N3) coverage effects on the photon to current conversion efficiencies were investigated by measuring the photocurrent action spectra and the optical absorbance of nanocrystalline TiO_2 films sensitized with various N3 coverages. The incident photon to current efficiency (IPCE) and the absorbed photon to current efficiency (APCE) showed abrupt increases at a coverage just above 30%. In order to explain the nonlinear increases in the IPCE and the APCE, the onset of a hole hopping mechanism was proposed where at greater than 30% coverage hole transfer between adjacent N3 molecules becomes possible. This percolation of holes through the N3 network facilitates the regeneration of oxidized N3 molecules by redox species (I^-) in the matrix of nanoporous structure resulting in the sudden increases in the IPCE and the APCE. Other mechanisms for this effect including a role of N3 clusters in two-electron oxidation of I^- are also discussed.

Reproduced with permission of the copyright owner. Further reproduction prohibited without permission.

2.1. Introduction

Dye sensitized nanocrystalline anatase solar cells have generated much recent interest due to advances in both their efficiency[1, 2] and stability.[3] Despite progress in the efficiency and stability of these solar cells there are many fundamental aspects of their operation that are still unknown. The detailed structure of the dye/semiconductor interface is a central problem for which there is little information. Recent publications have discussed some theoretical aspects of the binding of the favored ruthenium complex sensitizers to the anatase surface.[4-6] Another fundamental process, for which there is limited information, is the regeneration reaction between the photooxidized dye and the iodide ion that is commonly used to regenerate the adsorbed dye.

Herein we report studies of the adsorption and desorption kinetics of N3 to nanocrystalline anatase films. At long adsorption times the isotherm for the adsorption of N3 to the film is then determined and compared with a "desorption isotherm". Insights into the structure of the dye/semiconductor interface are obtained and are discussed in terms of models for the adsorption process. Knowing the optimal N3 dye coverage for efficient solar conversion is important because the relatively expensive N3 dye may be a large contributor to the total cost of sensitized nanocrystalline TiO_2 solar cells. The optimal dye coverage can be found by probing the quantum yield of the TiO_2 films sensitized at various N3 coverages. Diffuse reflectance spectroscopy is then used to measure the absorbance of the film in the visible region of the spectrum. The absorbance coupled with the measurements of the quantum yields, as a function of dye coverage and wavelength in a photoelectrochemical device, allows us to calculate the

Reproduced with permission of the copyright owner. Further reproduction prohibited without permission.

quantum yields per absorbed photon (APCE) at all wavelengths and at various dye coverages. The dependence of APCE on wavelength and dye coverage is obtained and discussed as it relates to the regeneration process of oxidized dye molecules.

2.2. Experimental

Nanocrystalline TiO_2 films were prepared by spreading a colloidal TiO_2 solution on conductive transparent indium tin oxide (ITO) coated glass. The TiO_2 colloidal solution was prepared as described in the literature as Method B.[2] TiO_2 powder (P25, Degussa; 3 g) was ground in a mortar with water (1 ml) containing acetylacetone (0.1 ml). After the TiO_2 particles were dispersed by the applied shear forces, the viscous solution was diluted with water (4 ml). Then, a surfactant (Triton X-100, Aldrich; 0.05 ml) was added. The ITO-coated glass was covered with two parallel adhesive tapes 1 cm apart to control the thickness and the area of the TiO_2 film (1.8 cm X 1.0 cm). The colloidal solution was applied between the tapes on the ITO-coated glass by rolling a glass rod on the surface. After air drying, the TiO_2 film was fired at 500 °C for 1 hour. The average film thickness was measured to be 13 μm from a scanning electron micrograph.

Adsorption of dye molecules, *cis*-di(thiocyanato)bis(2,2'-bipyridyl-4,4'-dicarboxylate)ruthenium(II) (N3; purchased from Solaronix SA, Switzerland), on a TiO_2 film was carried out by soaking TiO_2 films in N3/ethanol solutions (10 ml each). Three concentrations of N3/ethanol solutions were prepared (0.16 mM, 0.013 mM and 2.7 μM). To monitor the uptake of the N3 by the TiO_2 films, the absorbance of the N3/ethanol solutions was measured (Hewlett Packard, 8452A Diode Array

Reproduced with permission of the copyright owner. Further reproduction prohibited without permission.

Spectrophotometer) as a function of time. The amount of adsorbed N3 was calculated from the difference between the initial absorbance and the ones at subsequent time using the absorption coefficient of N3 in ethanol 1.42 x 10^4 M^{-1} cm^{-1} at 534 nm^2. Desorption experiments were done by placing the N3-coated TiO_2 films into ethanol. The TiO_2 films were dried by wicking with a piece of tissue (Kimwipes®, Kimberly-Clark) prior to the desorption experiments. This treatment minimized the amount of N3 trapped within the matrix of the TiO_2 film, but not bound to TiO_2 surface. As in the adsorption experiment, the absorbance of the N3 was monitored over time.

The configuration of the sensitized TiO_2 film solar cell was similar to the one described in reference 2. The counter electrode was platinum plate. The sensitized TiO_2 film and the platinum plate were sandwiched with a clip with a spacer (Teflon® film, 50μm thick) in-between. The redox couple (0.3 M LiI and 0.03 M I_2 in acetonitrile) was injected to the space between the electrodes with a syringe.

The action spectra of the TiO_2 films sensitized at various N3 coverages were taken using a Newport 75W tungsten halogen lamp, Jarrel-Ash 0.25-m monochromater and PAR 174 Polarographic Analyzer linked to a computerized control and data acquisition system. The absorbance of nanocrystalline TiO_2 films with various N3 coverages was measured with diffuse reflectance spectroscopy (Hitachi U-3501 spectrophotometer) due to the high scattering of TiO_2 nanoparticles.

Reproduced with permission of the copyright owner. Further reproduction prohibited without permission.

2.3. Results and Discussion

2.3.1. N3 Adsorption and Desorption

To investigate the kinetics of the adsorption of N3 onto nanocrystalline TiO_2 surfaces, the quantity of adsorbed N3 was monitored as a function of time (Figure 2.1) by following the disappearance of N3 from the solution as was described in the experimental section. A fast rate of adsorption was measured in the first 4 hours for all initial N3 concentrations. The initial fast adsorption rate from a 0.16 mM N3 solution was followed by a much slower adsorption rate. This trend was also observed but less apparent at lower concentrations. Stirring the N3 solutions did not affect the adsorption rates, which suggests that diffusional limitations were not important in the adsorption of N3 onto nanocrystalline TiO_2 for these N3 concentrations. Equilibration was reached after about 60 hours for all the N3 concentrations since no further adsorption was observed after this time. The Figure 2.2 shows the desorption of N3 into pure ethanol solutions as a function of time for samples where the initial adsorption was from various N3 concentrations. A fast desorption rate of N3 was also observed in the first 10 hours for all samples. Equilibration was reached after about 350 hours for all the samples since no further desorption was observed after this time. The ratio of the quantity of the desorbed N3 to the initially adsorbed N3 was calculated for all samples, and these values are shown in Table 2.1. Interestingly, the ratio of the desorbed N3 to the initially adsorbed N3 became greater as the quantity of the adsorbed N3 increased. Assuming that equilibrium conditions are achieved in the adsorption and desorption experiments, the isotherms for adsorption and desorption of N3 were obtained (Figure 2.3).

Reproduced with permission of the copyright owner. Further reproduction prohibited without permission.

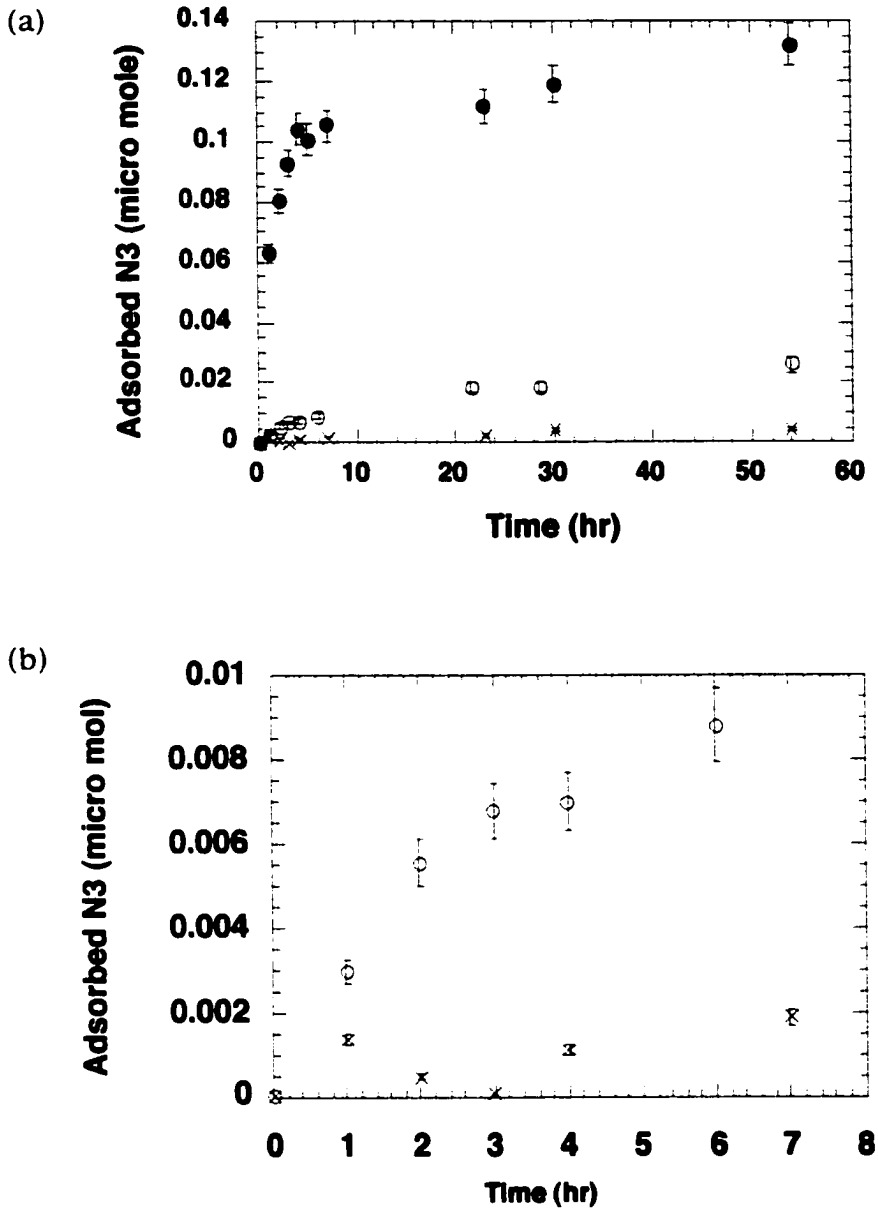

Figure 2.1. Adsorption of N3 to nanocrystalline TiO_2 as a function of time. Initial N3 concentrations are black circles: 0.16 mM; white circles: 0.013 mM; crosses: 2.7 μM. The initial adsorption from 0.013 mM and 2.7 μM N3 solutions are shown in (b).

Reproduced with permission of the copyright owner. Further reproduction prohibited without permission.

(a)

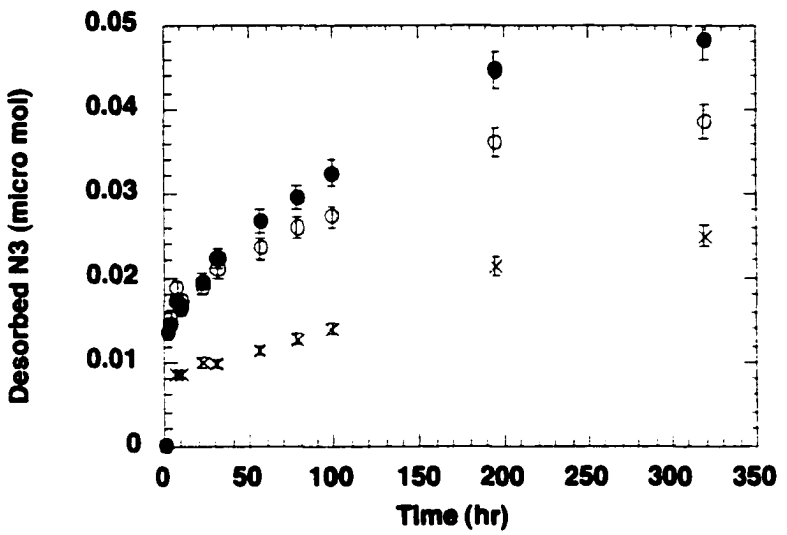

(b)

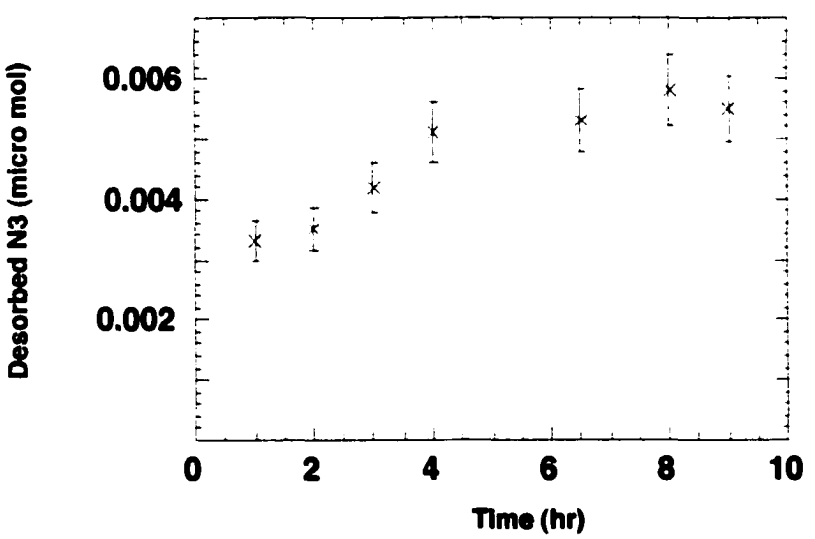

Figure 2.2. Desorption of N3 from nanocrystalline TiO_2 as a function of time. Quantities of adsorbed N3 prior to the desorption are black circles: 0.16 μmol; white circles: 0.12 μmol; crosses: 0.09 μmol. The initial desorption from the sample with 0.09 μmol N3 adsorbed is shown in (b).

Reproduced with permission of the copyright owner. Further reproduction prohibited without permission.

Table 2.1. Ratio of desorbed N3 to initially adsorbed N3.

Initially adsorbed N3 (μmole)	Desorbed N3 (μmole)	Ratio of desorbed N3 to initially adsorbed N3
0.056	0.014	0.25
0.090	0.025	0.28
0.12	0.038	0.32
0.15	0.068	0.45

Reproduced with permission of the copyright owner. Further reproduction prohibited without permission.

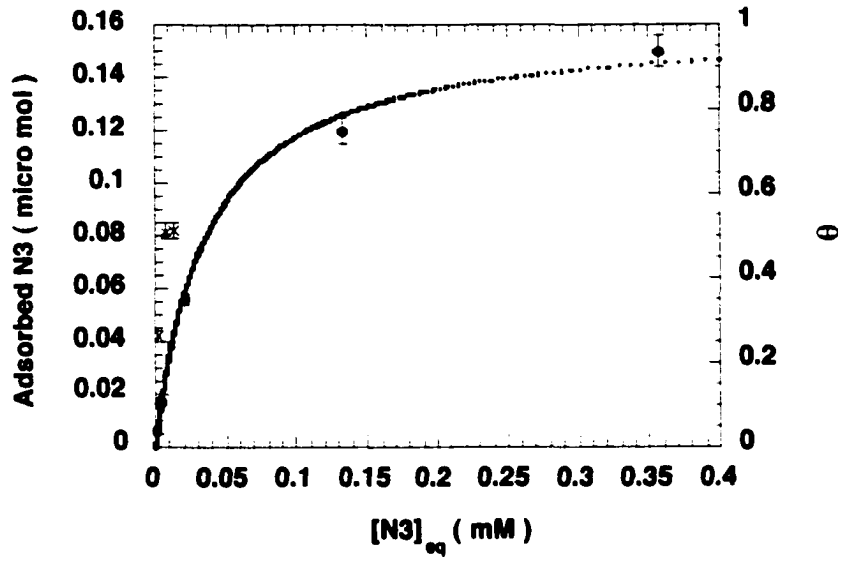

Figure 2.3. N3 adsorption and desorption isotherms. Black circles: adsorption; white circles: desorption; line: the best fit of the Langmuir adsorption equation.

Reproduced with permission of the copyright owner. Further reproduction prohibited without permission.

Although many of the assumptions inherent in the Langmuir isotherm are not valid, such as the equivalence of all sites and independence of the occupation of sites with coverage, the experimental data were fit to a Langmuir adsorption isotherm (dashed line in Figure 2.3), as stated by equation 1,

$$\Theta = \frac{KC}{1 + KC} \qquad [1]$$

where Θ is the fractional coverage, K is the adsorption constant, and C is the concentration of N3 in solution. The best fit was obtained with $K = 2.8 \times 10^{4}$ M^{-1} and the full coverage of N3 was found to be 0.16 μmol. Assuming a molecular area of N3 projecting on TiO_2 to be 180 $Å^2$ from the molecular axes of N3 (~14.2 Å and ~12.6 Å), a surface area of the TiO_2 film was calculated to be 30 m^2/g_{TiO_2}. Other groups have reported a value of 40.2 m^2/g_{TiO_2} from krypton adsorption measurements.[7] Our smaller value for the surface area may be the result of unoccupied adsorption sites due to what may well be imperfect packing of N3 molecules. Inaccessible sites for N3 molecules because of small pores may also contribute to the smaller value for the surface area. Figure 2.3 also shows that the isotherm measured for the desorption process is different from the isotherm measured for the adsorption process, bringing the assumption of equilibrium conditions into question.

2.3.2 Model for N3 Binding to Nanocrystalline TiO_2

The binding of N3 to a nanocrystalline TiO_2 film has been studied by other groups. The three possible coordination modes of the carboxyl group

Reproduced with permission of the copyright owner. Further reproduction prohibited without permission.

were discussed in these studies. Those coordinations are unidentate (ester-like linkage),[8] bidentate chelating or bridging (i.e. two Ti^{4+} sites bound to one carboxyl group).[9] We are interested in how many carboxyl groups are involved in the binding of N3 to TiO_2. Since there are four carboxyl groups present in one N3 molecule, up to four attachments are in principal possible. One, two or three-site binding by up to three carboxyl groups on a flat surface seems reasonable when considering the geometry of N3 molecule[6]. Some of the possible binding modes of N3 to TiO_2 surface are shown in Figure 2.4. Additional binding geometries at step sites and kink sites may also be possible.

The adsorption and desorption kinetic measurements provide some insights into the nature of N3 binding to anatase. A scheme consistent with the kinetic measurements for the binding of N3 to TiO_2 surface is shown below.

$$N3_{soln} \rightleftharpoons N3_{surf\ (1)} \rightleftharpoons N3_{surf\ (2)}$$

Less strongly bound *Strongly bound*

According to the scheme a N3 molecule attaches to the TiO_2 surface first with one carboxyl group ($N3_{surf(1)}$) followed by the second carboxyl group ($N3_{surf(2)}$). The forward rate in the first step is much greater than the back rate. The large difference in the rates is consistent with the initial fast adsorption. The initial fast adsorption can be explained as the rapid binding of one carboxyl group of a $N3_{soln}$ to a Ti^{4+} site on the TiO_2 surface in the $N3_{surf(1)}$ mode. The difference between the forward and back rates in the

Reproduced with permission of the copyright owner. Further reproduction prohibited without permission.

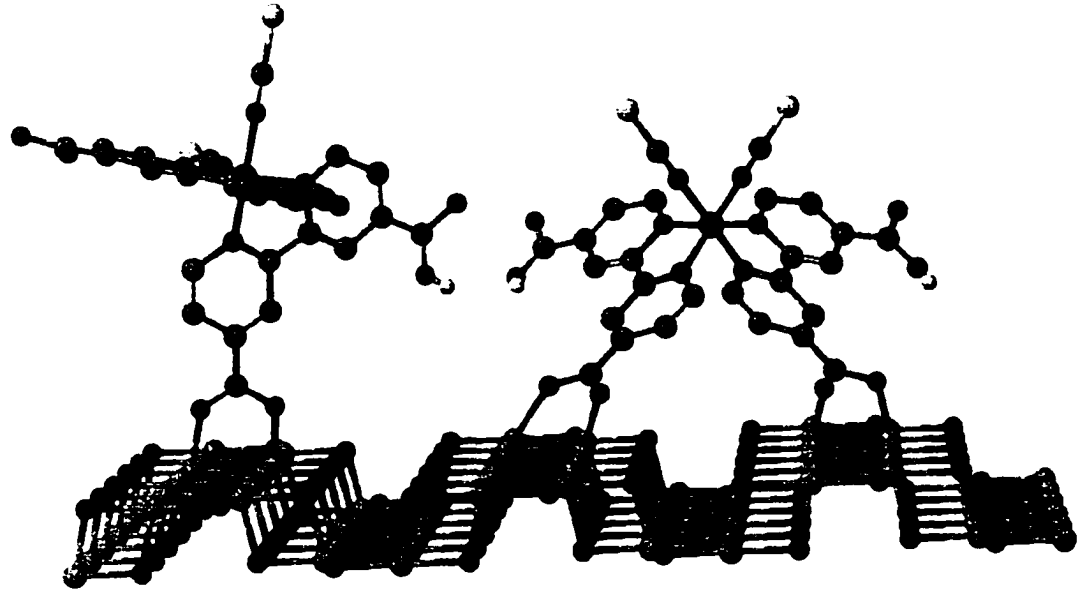

Figure 2.4. Possible binding modes of N3 to TiO_2 (101) surface. The left N3 is bound to the TiO_2 with one carboxyl group. The right N3 is bound with two carboxyl groups. Light blue: titanium; red: oxygen; grey: carbon; blue: nitrogen; pink: ruthenium; yellow: sulfur; light grey: hydrogen.

Reproduced with permission of the copyright owner. Further reproduction prohibited without permission.

second adsorption step is also very large. These large differences in the rates in each step suggest stability of N3 binding to anatase. This stability is similar to the one formed by the chelate effect. In other words, the probability of simultaneous dissociation of two carboxyl groups is very low. Also, it is quite unlikely that two carboxyl groups bind simultaneously to TiO_2 surface, so we favor a sequential binding of the two carboxyl groups. The two-step binding mechanism is consistent with the observation that the ratio of the amount of desorbed N3 to the amount of initially adsorbed N3 becomes greater as the coverage increases (Table 2.1). At a higher coverage more N3 molecules are bound with one carboxylate because of the difficulty of finding a second binding site due to blockage of surface sites by adjacent N3 molecules. Consequently, a greater ratio of the adsorbed N3 desorbs from TiO_2. This explanation is also dependent on a limited surface mobility of the bound N3 molecules.

Desorption kinetics from anatase films were compared between rapidly and slowly adsorbed N3. The rapid adsorption was carried out by using a concentrated N3 solution while the slow adsorption was done by using a less concentrated N3 solution. The anatase film with more rapidly adsorbed N3 was prepared by soaking in a 0.19 mM N3 solution in ethanol for one hour. The film with slowly adsorbed N3 was prepared by soaking in a 0.039 mM N3 solution for 17 hours. The quantities of the adsorbed N3 were calculated to be 0.075 μmol for the rapid adsorption film and 0.083 μmol for the slow adsorption film. These amounts of N3 correspond to approximately 50% coverage. The desorption experiments were carried out immediately after the completion of each adsorption step. The quantities of the desorbed N3 during the initial 25 hours were found to be 0.0082 μmol from the film with

Reproduced with permission of the copyright owner. Further reproduction prohibited without permission.

rapidly adsorbed N3 and 0.0070 μmol from the film with slowly adsorbed N3. More desorption was observed for the rapidly adsorbed N3 even though the quantity of the adsorbed N3 was smaller. This observation was reproduced with another set of anatase films. The greater initial desorption rates and desorption ratios for the rapidly adsorbed N3 add support to the stepwise binding model of the carboxyl groups. The rapidly adsorbed N3 did not have time for completing the second binding step. As a result, more N3 desorbed via the weaker binding mode ($N3_{surf(1)}$).

2.3.3. Dye Coverage Effects on Incident Photon to Current Efficiency

The action spectra of TiO_2 films sensitized at various N3 coverages were taken to determine the optimal dye coverage and examine the effects of N3 coverage on the incident photon to current efficiency (IPCE) (Figure 2.5.a). Generally, the IPCE is expected to increase linearly with dye coverage because more adsorbed dye molecules will absorb proportionally more photons thus generating a greater photocurrent. Figure 2.5.a shows that the IPCE increases as a dye coverage increases. A saturation of the IPCE at a value of about 0.62 is reached at wavelengths from 450 to 500 nm. This value (0.62) is below the best value observed in the most efficient solar cells,[2] but it is high enough to demonstrate that we are studying an efficient light to electron converting system. Additional dye adsorption results in further increases only in the longer wavelength region (550 ~ 800 nm). The dependence of the IPCE on dye coverage for wavelengths of 550 nm and 700 nm is plotted in Figure 2.5.b. The anticipated linear dependence of IPCE on dye coverage was not observed. Instead Figure 2.5.b indicates a rapid increase in the IPCE at 550 nm at a N3 coverage of about 0.05 μmol. This

Reproduced with permission of the copyright owner. Further reproduction prohibited without permission.

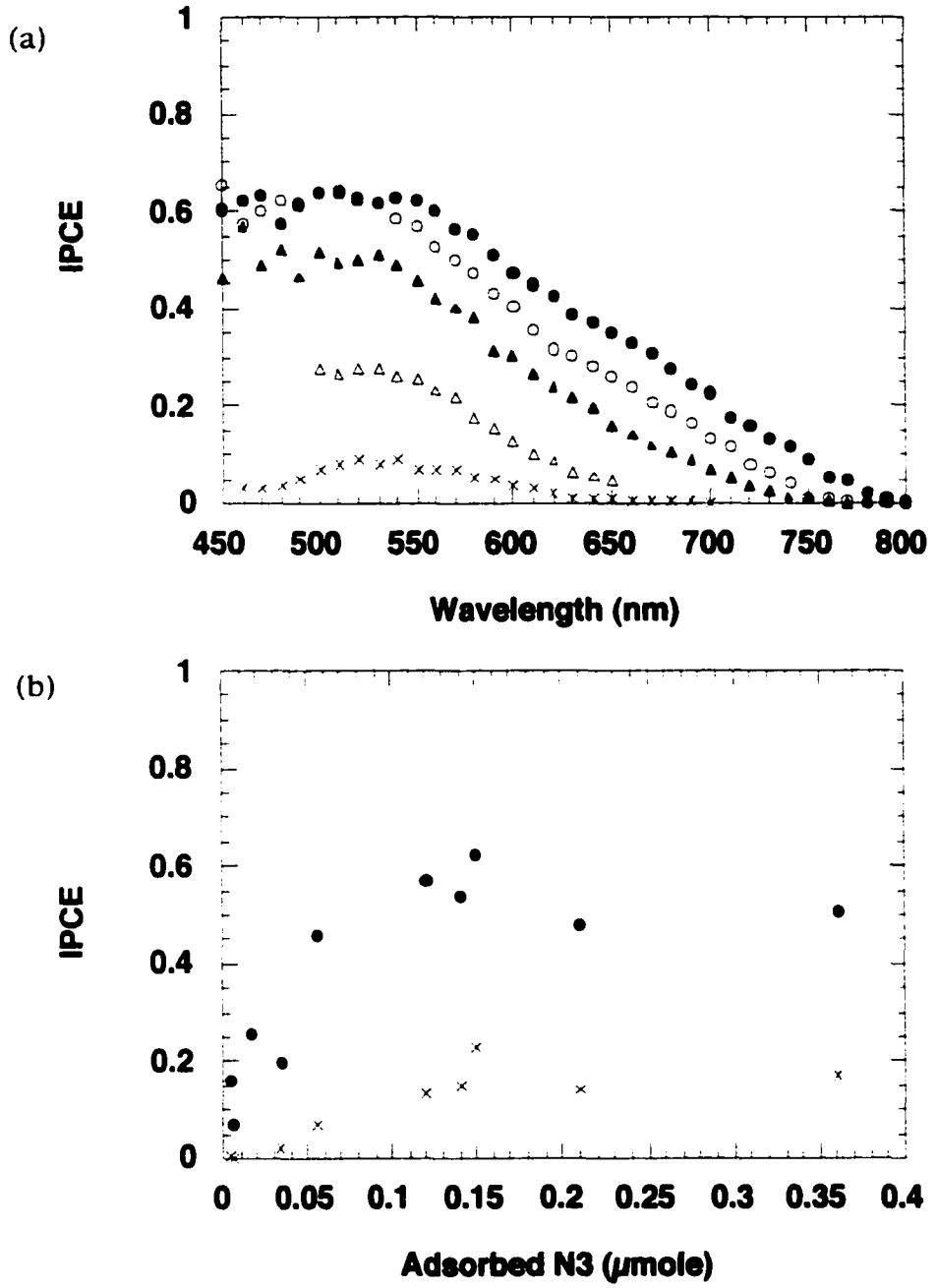

Figure 2.5. Incident photon to current efficiency of nanocrystalline TiO_2 films sensitized with N3 at a various coverage(a). Adsorbed N3 is black circles: 0.15 μmol; white circles: 0.12 μmol; black triangles: 0.056 μmol; white triangles: 0.017 μmol; crosses: 0.006 μmol. (b) IPCE at 550 nm (black circles) and at 700 nm (crosses).

Reproduced with permission of the copyright owner. Further reproduction prohibited without permission.

abrupt increase in the IPCE at about 0.05 μmol N3 coverage will be discussed later.

2.3.4. Absorbance of N3 Adsorbed to a Nanocrystalline TiO_2 Film

The absorbance of the N3 on TiO_2 films needs to be determined in order to calculate the absorbed photon to current efficiency (APCE). Radiation reflected by a diffusive surface consists of two parts, "regular reflection" and "diffuse reflection". The absorbance converted from only regular reflection, under the condition of no transmittance, obeys Beer's law in a certain range of concentrations. However, the absorbance converted from the both types of reflection with no transmittance does not obey Beer's law. The reason for this phenomenon is explained in reference 10 as follows: "the diffuse reflection comes about through penetration of a portion of the incident flux into the interior of the sample. A part of this radiation is returned to the surface of the sample, following partial absorption and multiple scattering at the boundaries of the individual particles of which the sample is composed." Therefore, the absorbance of N3 adsorbed to TiO_2 nanoparticles is expected to deviate from Beer's law. The measured reflectance was converted directly to absorbance (log(1/R)). Since the purpose of the reflectance measurements was not to determine the N3 concentration but to measure the absorbance of the N3 adsorbed to TiO_2 nanoparticles, the Kubelka-Munk function, a common method to convert reflectance involving diffusive media to the concentration,[10] was not used. The absorbance of N3 on the TiO_2 films was then obtained from subtracting the absorbance of the TiO_2 film as described in equation 2.

Reproduced with permission of the copyright owner. Further reproduction prohibited without permission.

$$\log(1/R)_{N3} = \log(1/R)_{N3/TiO_2} - \log(1/R)_{TiO_2} \quad [2]$$

The resulting wavelength dependence is shown in Figure 2.6.a. The absorbances of N3 in ethanol and N3 anchored to a TiO_2 surface were compared at 534, 600, 650 and 700 nm(Figure 2.6.b). Figure 2.6.b shows that the absorption coefficient determined for N3 adsorbed to TiO_2 is almost twice of that for N3 dissolved in ethanol[2] at 600, 650 and 700 nm. The discrepancy is greater at 534 nm when the coverage is low. At low coverages the absorbance of adsorbed N3 is greater than that of solution phase N3, but approaches that of the solution as the coverage increases. The origin of this phenomenon is considered to be related to Rayleigh scattering within the TiO_2 film. The actual path length for light in a TiO_2 film with a low N3 coverage is much longer than in a homogeneous N3 solution because the TiO_2 particles scatter light. Rayleigh scattering is greater for shorter wavelength light and becomes smaller as the N3 coverage increases since more light is initially absorbed.

2.3.5. Dye Coverage Effects on Absorbed Photon to Current Efficiency

The absorbed photon to current efficiency (APCE) of each film was calculated from the IPCE and the measured absorbance of the film in order to investigate the effects of dye coverage on APCE (Figure 2.7.a). One would expect that the APCE would be independent of the quantity of adsorbed N3 and the wavelength of incident light because APCE evaluates the efficiency only after the absorption of light. It is notable that the APCE as a function of wavelength for TiO_2 films with 0.15, 0.12 and 0.056 μmol N3 coverages almost overlay each other. However, a drop-off in the APCE was observed below a

Reproduced with permission of the copyright owner. Further reproduction prohibited without permission.

(a)

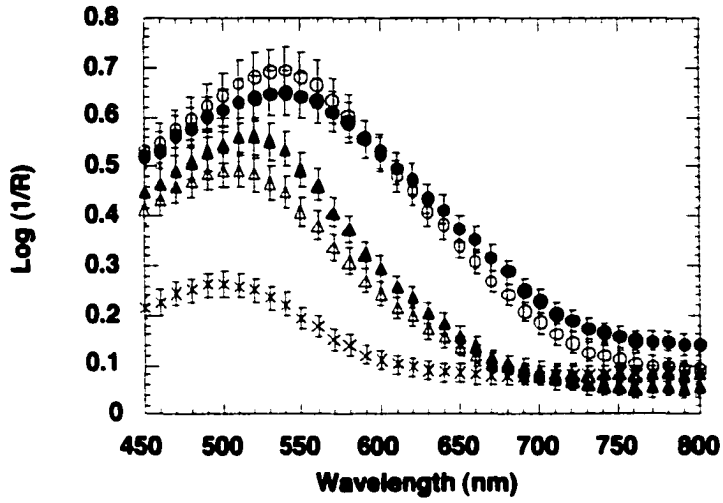

(b)

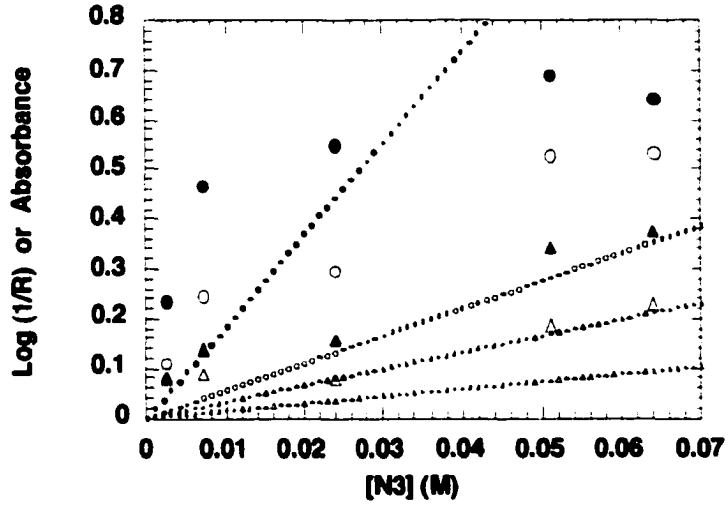

Figure 2.6. Absorbance spectra (log(1/R)) of N3 adsorbed to a nanocrystalline TiO2 film at various coverage(a). Adsorbed N3 is black circles: 0.15 μmol; white circles: 0.12 μmol; black triangles: 0.056 μmol; white triangles: 0.017 μmol; crosses: 0.006 μmol. (b)Absorbance (log(1/R)) of adsorbed N3 and absorbance (A) of N3 in ethanol at certain wavelengths. Black circles: at 534 nm; white circles: at 600 nm; black triangles: at 650 nm; white triangle: at 700 nm; black circle line: at 534 nm; white circle line: at 600 nm; black triangle line: at 650 nm; white triangle line: at 700 nm. The published value 1.42×10^4 M^{-1} cm^{-1} was used for the absorption coefficient of N3 in ethanol at 534 nm.[2] The absorption coefficients at 600 nm, 650 nm and 700 nm were obtained from an absorption spectrum.

Reproduced with permission of the copyright owner. Further reproduction prohibited without permission.

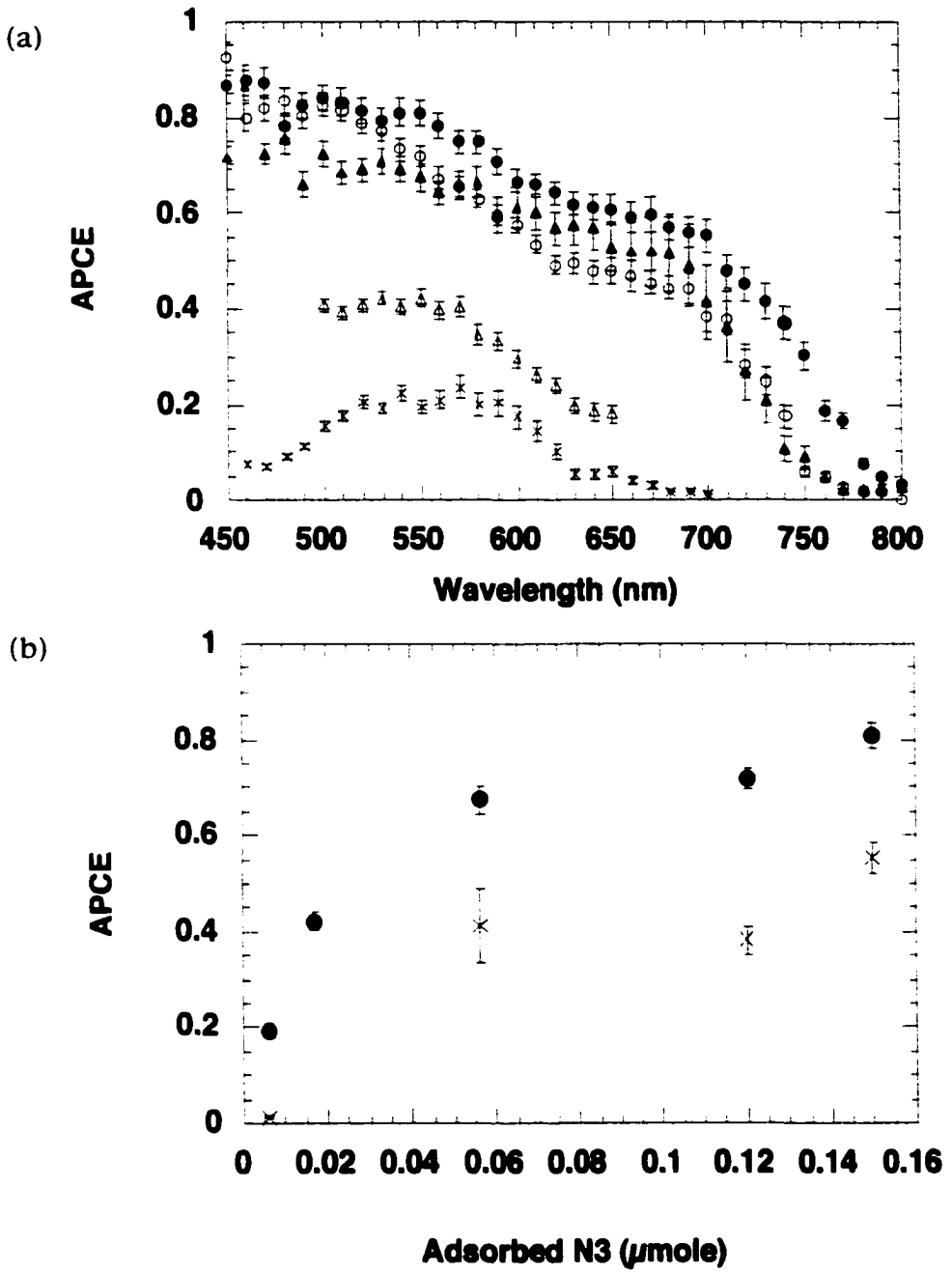

Figure 2.7. Absorbed photon to current efficiency of a nanocrystalline TiO_2 film at various coverage(a). Adsorbed N3, black circles: 0.15 μmol; white circles: 0.12 μmol; black triangles: 0.056 μmol; white triangles: 0.017 μmol; crosses: 0.006 μmol. (b) APCE at 550 nm and (c) at 700 nm.

Reproduced with permission of the copyright owner. Further reproduction prohibited without permission.

coverage of 0.056 μmol of N3. The variation of the APCE with the quantity of adsorbed N3 at two wavelengths of incident light is shown in Figure 2.7.b. The APCE for coverages above 0.05 μmol N3 is 0.6 ~ 0.8 at 550 nm and 0.25 ~ 0.55 at 700 nm while the APCE for less than 0.05 μmol N3 coverage is about 0.2 ~ 0.4 at 550 nm and less than 0.1 at 700 nm. These variations of the APCE with the quantity of adsorbed N3 and the wavelength of incident light are contradictory to the original expectation.

2.3.6. Possible Explanations for the Dye Coverage Effects on APCE

There are a few possible reasons to explain why the APCE is smaller in the longer wavelength region. (1) Since we have back illumination, the electrons generated by longer wavelength light have longer paths to be collected at the back contact. The absorption coefficient of the adsorbed N3 is greater for shorter wavelengths between 534 and 700 nm. For instance, according to Figure 2.6.b when the adsorbed N3 concentration is 0.05 M, the absorption coefficient of the adsorbed N3 is calculated to be 1.0×10^4 $M^{-1}cm^{-1}$ at 534 nm and 2.7×10^3 $M^{-1}cm^{-1}$ at 700 nm, using the 13 μm film thickness. The relation between light intensity at some distance from incident surface and the incident light intensity I_0 is shown in equation 3.

$$I = \frac{I_0}{10^{\varepsilon c x}} \qquad [3]$$

where ε is absorption coefficient, c is the N3 concentration and x is the distance from the film surface. The majority of electrons generated by short wavelength light are present near the illuminated surface that is also a back contact. On the other hand, electrons generated by longer wavelength light are distributed more evenly from the illuminated surface to the back side of

Reproduced with permission of the copyright owner. Further reproduction prohibited without permission.

the film. Consequently, a larger fraction of the electrons generated by longer wavelength light must travel longer paths to the back contact than ones generated by shorter wavelength light. Longer paths result in more trapping[11] and recombination of the electrons injected to TiO_2 conduction band and subsequently lower APCEs.

(1) The electrons generated by longer wavelength light may have a smaller driving force for transport to the back contact than ones generated by shorter wavelength light. The driving force for electron movement in the film is from diffusion due to the electron concentration gradient in the film since there is no space charge field inside of nanocrystalline TiO_2.[12] The less strongly absorbed long wavelength light produces a smaller electron concentration gradient near the back contact, resulting in a smaller driving force for the collection of electrons generated near the contact. Again more trapping and recombination occur for electrons generated by longer wavelength light, resulting in the lower APCE.

The lower APCE at low dye coverages can be explained by several scenarios: (1) Back electron transfer from the TiO_2 conduction band to the redox species (I_3^-) may be faster at low N3 coverages because more TiO_2 surface is exposed to the redox species. This assumes that the exchange current for I^- / I_3^- reaction is higher on the TiO_2 surface rather than through mediation by N3 complexes.

(2) N3 clusters may be necessary for two electron oxidation of I^- (i.e. $3I^-$ -----> $I_3^- + 2e^-$). The oxidation of I^- to I_3^- without generating high energy free iodine radicals requires adjacent oxidation sites and coupling of the adsorbed one-electron transfer intermediates to form I-I bond as occurs on clean Pt electrodes. If iodide oxidation is mediated by adsorbed N3, then

Reproduced with permission of the copyright owner. Further reproduction prohibited without permission.

the coupling reaction needs adjacent N3 molecules to avoid free iodine radicals. Hence, the regeneration of oxidized N3 is less efficient at low N3 coverages.

(3) The electron path to back contact is longer at lower dye coverages since the light penetrates more deeply into the TiO_2 film. Longer electron paths may result in a lower APCE as previously described for the long wavelength effect.

(4) The driving force for the transport of the injected electrons to the back contact may be smaller at a low coverage. This was also previously described by the electron concentration profiles in a TiO_2 film for the long wavelength effect.

(5) The injection efficiency of electrons from adsorbed N3 into the TiO_2 conduction band may be lower at low coverages. We see no reason why this should be true, and recent experiments by Willig et al.[13] are shown that the injection efficiency is independent of dye coverage.

(6) Another explanation for the abrupt increase in the APCE at around 0.05 μmol N3 coverage is that a hole hopping mechanism can occur through N3 molecules at that coverage. The hole hopping is a successive oxidation of N3 molecules by adjacent N3 molecules. This mechanism facilitates the regeneration of oxidized N3 molecules, resulting in the sudden enhancement of conversion efficiencies (Figure 2.7 a. & b.). Limitation of the regeneration of oxidized N3 molecules due to the restricted diffusion of the regenerating species (I^-) in the matrix of a nanoporous TiO_2 film has been overlooked. In a mathematical model of the nanocrystalline solar cell, the diffusion of I^- has been assumed to be affected very little by the presence of the solid nanocrystalline TiO_2.[14] However, we expect that the tortuous path

Reproduced with permission of the copyright owner. Further reproduction prohibited without permission.

for I^- diffusion through the TiO_2 nanocrystalline film will considerably hinder the diffusion. The resulting iodide concentration polarization in the nooks and crannies within the nanoporous film should inhibit the regeneration of dye molecules bound to the surface in these regions unless there is some mechanism to help the regeneration. We propose that one mechanism can be a hole hopping through the N3 molecular network (Figure 2.8). We propose that thus network is formed at about 0.05 μmol N3 coverage, close to a percolation threshold. Assuming that full coverage of a TiO_2 film corresponds to 0.16 μmol (from the adsorption isotherm), the onset of the hole transport mechanism appears at about 30 % of the full coverage. A lower than theoretical percolation threshold may be the result of the condition that only local networks need to exist, that is, percolation through the entire film is not necessary.

A phenomenon similar to the hole hopping was discussed in recent publications.[15, 16] Bonhôte et al. studied a phosphonated triarylamine adsorbed on a nanocrystalline metal oxide film and explained their results with lateral electron transport inside the monolayer of the triamine molecules[15]. The percolation threshold for the lateral electron transport was reported to be about 50 % of the full coverage. Trammell and Meyer studied an osmium complex adsorbed on a nanocrystalline TiO_2 film and reported electron transfer in the monolayer of the osmium complexes.[16] The percolation threshold for this system was found to be about 60 % of the full coverage. Yet, another group reported that some ruthenium complexes grafted on nanocrystalline layers do not display lateral charge transport, at least not to a comparable extent[17].

Reproduced with permission of the copyright owner. Further reproduction prohibited without permission.

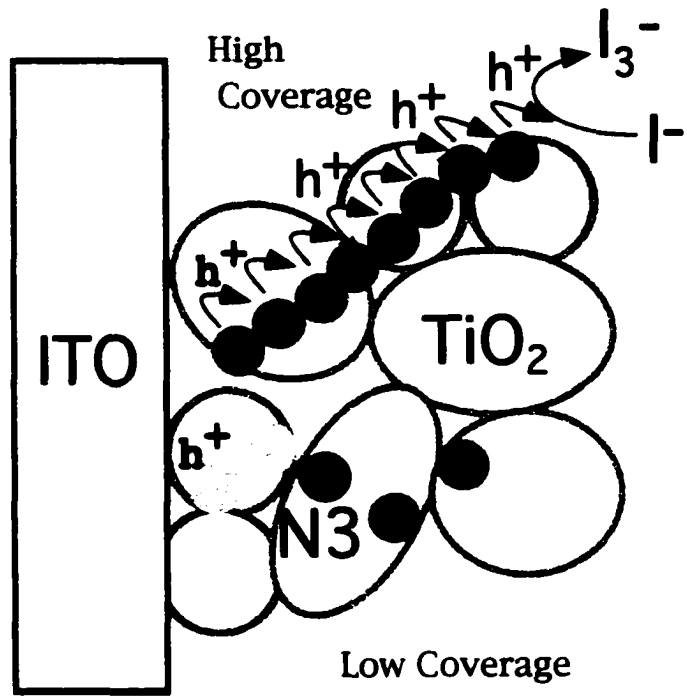

Figure 2.8. Hole hopping mechanism. Small black circles: N3 (small gray circles: oxidized N3); large gray circles: nanocrystalline TiO_2. At a coverage above 30%, hole hopping is possible through the adjacent N3 molecules, resulting in the facilitation of the regeneration of oxidized N3. At coverage below 30 %, there is no such facilitation due to the lack of the N3 network.

Reproduced with permission of the copyright owner. Further reproduction prohibited without permission.

The APCE dependence on dye coverage and the abrupt enhancement of the APCE at around the 0.05 μmol dye coverage may not be a consequence of a single mechanism but a combination of the scenarios described above. Especially, the role of N3 clusters in two electron oxidation of I^-, as was discussed as scenario(2), is equally reasonable with the hole hopping mechanism in order to rationalize the abrupt increases. For clarification of the mechanism, further experiments are needed.

2.4. Conclusions

The measured adsorption and desorption kinetics suggest a two-step adsorption mechanism for the binding of N3 to nanocrystalline TiO_2. The difference between the adsorption isotherm and "desorption isotherm" is consistent with a two-step adsorption mechanism. The dye coverage dependence of the IPCE and APCE shows an abrupt increase in these parameters at about 30 % dye coverage. The abrupt increase in the IPCE and the APCE suggests the possibility of limited regeneration of the oxidized N3 at low coverages. The limited regeneration may be due to the limited diffusion of the reducing species in the matrix of a nanoporous TiO_2 film. In order to explain the abrupt increase at 30 % coverage, the onset of a hole hopping mechanism at the coverage was proposed as well as the necessity of N3 clusters for the two-electron oxidation of I^-. Further work needs to be done to clarify the exact mechanism for these effects.

Reproduced with permission of the copyright owner. Further reproduction prohibited without permission.

References cited in Chapter 2

1. B. O'Regan and M. Grätzel, *Nature*, **353**, 737 (1991).

2. M. K. Nazeeruddin, A. Kay, I. Rodicio, R. Humphry-Baker, E. Müller, P. Liska, N. Vlachopoulos, and M. Grätzel, *J. Am. Chem. Soc.*, **115**, 6382 (1993).

3. O. Kohle, M. Grätzel, A. F. Meyer, and T. B. Meyer, *Adv. Mater.*, **9**, 904 (1997).

4. V. Shklover, M.-K. Nazeeruddin, S. M. Zakeeruddin, C. Barbé, A. Kay, T. Haibach, W. Steurer, R. Hermann, H.-U. Nissen, and M. Grätzel, *Chem. Mater.*, **9**, 430 (1997).

5. V. Shklover, T. Haibach, B. Bolliger, M. Hochstrasser, M. Erbudak, H.-U. Nissen, S. M. Zakeeruddin, M. K. Nazeeruddin, and M. Grätzel, *J. Solid State Chem.*, **132**, 60 (1997).

6. V. Shklover, Y. E. Ovchinnikov, L. S. Braginsky, S. M. Zakeeruddin, and M. Grätzel, *Chem. Mater.*, **10**, 2533 (1998).

7. L. Kavan, M. Grätzel, J. Rathousky, and A. Aukal, *J. Electrochem. Soc.*, **143**, 394 (1996).

8. K. Murakoshi, G. Kano, Y. Wada, S. Yanagida, H. Miyazaki, M. Matsumoto, and S. Murasawa, *J. Electroanal. Chem.*, **396**, 27 (1995).

9. K. S. Finnie, J. R. Bartlett, and J. L. Woolfrey, *Langmuir*, **14**, 2744 (1998).

10. W. Wendlandt and H. Hecht, *Reflectance Spectroscopy*, Jon Wiley & Sons, New York (1966).

11. P. E. de Jongh and D. Vanmaekelbergh, *Physical Review Letters*, **77**, 3427 (1996).

12. A. Hagfeldt and M. Grätzel, *Chem. Rev.*, **95**, 49 (1995).

13. F. Willig, *private communication* (1998).

14. N. Papageorgiou, M. Grätzel, and P. P. Infelta, *Solar Energy Materials and Solar Cells*, **44**, 405 (1996).

15. P. Bonhôte, E. Gogniat, S. Tingry, C. Barbé, N. Vlachopoulos, F. Lenzmann, P. Comte, and M. Grätzel, *J. Phys. Chem. B*, **102**, 1498 (1998).

Reproduced with permission of the copyright owner. Further reproduction prohibited without permission.

16. S. A. Trammell and M. T. J. Meyer, *J. Phys. Chem. B*, **103**, 4156 (1999).

17. T. A. Heimer, S. T. D'Arcangelis, F. Farzad, J. M. Stipkala, and G. J. Meyer, *Inorg. Chem.*, **35**, 5319 (1996).

Reproduced with permission of the copyright owner. Further reproduction prohibited without permission.

Preface to Chapter Three

In the previous chapter, the dye adsorption behavior and the relationship between photon to current efficiency and the dye coverage were investigated in nanocrystalline films. In this chapter, the dye/TiO_2 interface is investigated by utilizing natural single crystals to circumvent the complexity of nanoporous structure of the TiO_2 film.

I am presenting my second publication as chapter 3 of my dissertation. This paper will be submitted for publication. The preliminary work on sensitization of natural anatase crystals was done by our previous post doctoral researcher, Dr. David Soltz, and our summer undergraduate research assistant, Stephanie Hamilton. However, almost all the data presented in this publication are solely my own experiments.

Reproduced with permission of the copyright owner. Further reproduction prohibited without permission.

CHAPTER THREE

Dye Sensitization of Natural Anatase Crystals with a Ruthenium-Based Dye

ABSTRACT

Semiconducting natural anatase crystals from two different sources were sensitized with a ruthenium-based dye (*cis*-di(thiocyanato)-bis(2,2'-bipyridyl-4,4'-dicarboxylate)ruthenium(II):N3). The maximum incident photon to sensitized photocurrent conversion yield was 3.2×10^{-4}. A crystal face dependence of sensitization efficiency was also observed. Variation in sensitization yields of (101) faces, by up to a factor of 4, were also observed. The efficiency of sensitization on the (101) face was approximately one order of magnitude more than the (001) face. Examination of the morphology of the crystal surfaces with atomic force microscopy and scanning electron microscopy indicated that these differences in sensitization by the different faces and by the crystals were not solely the result of the differences in the microscopic surface areas. Natural anatase crystals had millisecond rise time for the sensitization photocurrent: The rise time decreased with greater light intensity and greater dye coverage, suggesting that trapping and detrapping of injected electrons at traps in the crystals is involved in the electron transport in the natural anatase. The comparison of the sensitization behavior between anatase single crystals (natural and synthetic) and anatase nanocrystalline films revealed that the absorbed photon to current efficiency of the nanocrystalline films was approximately 3 to 7 times greater than that of the single crystals.

Reproduced with permission of the copyright owner. Further reproduction prohibited without permission.

3.1. Introduction

Dye sensitized nanocrystalline anatase solar cells have recently made great progress in both efficiency[1, 2] and stability.[3] Despite this rapid progress, there is still relatively little known about the adsorption of the ruthenium-based dyes onto the anatase surface. The most popular sensitizing dye, *cis*-di(thiocyanato)bis(2,2'-bipyridyl-4,4'-dicarboxylate) ruthenium (II), also known as N3, has four pendant carboxyl groups and it is thought that it can bind to a planar anatase surface with at least two but up to three of these groups.[4-6] In principle all four carboxyl groups could be involved in bonding at step, kink or defect sites. In a previous paper we studied the adsorption isotherm and the kinetics of adsorption and desorption of N3 onto nanocrystalline anatase/rutile films.[7] A two-step dye adsorption mechanism was postulated, where the initial binding is through one carboxyl group with subsequent binding by a second carboxyl group. Dye (N3) coverage effects on the photon to current conversion efficiencies were also investigated by measuring the photocurrent action spectra and the optical absorbance of nanocrystalline TiO_2 films sensitized with various N3 coverages. The large surface area, the heterogeneous surface structure, the effect of electron transport through the films and the porous nature of the films made it difficult to make definitive conclusions about coverage effects on the quantum yields and spectral response of the dye/anatase interface itself.

Herein we present results on N3 adsorption on natural crystals of anatase. There has been considerable work on the sensitization of rutile single crystals with adsorbed dyes.[8-11] Often very low quantum yields per

Reproduced with permission of the copyright owner. Further reproduction prohibited without permission.

incident or absorbed photon have been measured.[12-14] Most of the dyes studied on rutile surfaces have not been covalently attached to the surface, and so the low quantum yield in this case may be due to poor electronic overlap with the conduction band states in the rutile. There has been one study of N3 sensitization on synthetic anatase and rutile.[15] The (101) face of an anatase crystal and the (001) face of a rutile crystal had similar sensitization efficiencies from adsorbed N3.[15] The small size and difficulty of growing the anatase crystals prompted us to exploit the existence of natural anatase crystals for studying dye-sensitized photocurrents. The bulk electrical properties of these crystals are likely dominated by the naturally occurring impurities in the crystals, however the surface composition and structure is expected to be less perturbed by even a few parts per thousand of impurities. The adsorption behavior of the N3 is also expected to be similar to that on a nanocrystalline film since, on a molecular scale, a 40 nm square face of a nanocrystal is indistinguishable from an anatase terrace on a bulk single crystal.

One distinct difference between the nanocrystalline and bulk crystal is the existence of a space charge field in the bulk crystal. The nanocrystalline anatase particles are too small to support a depletion layer resulting from dopants since many of the particles will not have any dopant atoms. Therefore, it will be interesting to compare the quantum yields obtained for the two systems.

Reproduced with permission of the copyright owner. Further reproduction prohibited without permission.

3.2. Experimental

Natural anatase crystals were obtained from sources in Tyssedal, Norway and Minas Gerais, Brazil. The crystal form and orientation were determined with angular x-ray diffraction and Laue back reflection. The Norwegian anatase crystals were an acute bipyramidal configuration and had a black luster. One of the Norwegian crystals is shown in Figure 3.1.a. All of the Norwegian crystals exhibited clearly defined (101) faces as shown in Figure 3.1.a. The Brazilian anatase crystals were a tabular habit and were translucent reddish brown. One of the Brazilian crystals is shown in Figure 3.1.b. All of the Brazilian crystals exhibited one or two (001) faces and several (101) faces as shown in Figure 3.1.b.

The crystals were prepared for electrodes by insulating with silicone sealant (RTV). Ohmic contacts were obtained by rubbing indium-gallium eutectic alloy onto the backs of the crystals, and then securing them to copper disks with silver epoxy (Tricon). Mott-Schottky measurements were performed with a PAR 173 potentiostat/galvanostat, Stanford Research Systems SR 530 lock-in amplifier, and a computerized control and data acquisition setup. Photocurrent–voltage curves were obtained with a PAR 174 polarographic analyzer linked to an AD Instruments MacLab® running Electro-Lab® data collection software. The light source for some of the quantum yield measurements was an Ion Laser Technology model 450 ASL argon ion laser at 514 nm. The diameter of the beam was 1.0 mm. The intensity of the beam illuminating the sample surface was varied from 1.0 W cm^{-2} to 1.9 mW cm^{-2} by using neutral density filters. Acetonitrile (analytical grade) with 15 mM KI and 1.5 mM I_2 was used as an electrolyte solution for all

Reproduced with permission of the copyright owner. Further reproduction prohibited without permission.

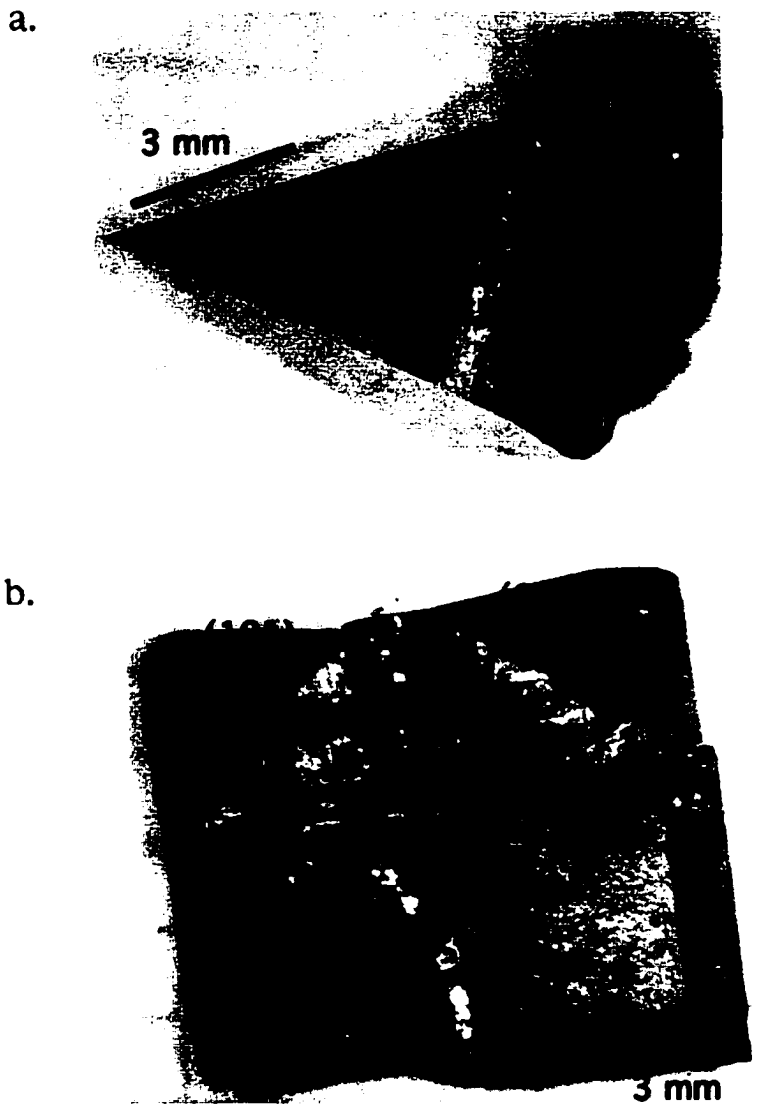

Figure 3.1. Optical micrographs of the natural anatase crystals. (a) The Norwegian anatase. (b) The Brazilian anatase.

Reproduced with permission of the copyright owner. Further reproduction prohibited without permission.

the experiments. The reference electrode was a Ag/AgCl electrode in acetonitrile or a Ag/Ag^+ in acetonitrile with 0.1 M tetrabutylammonium perchlorate and 0.01 M $AgNO_3$. The counter electrode was a cylindrical section of platinum gauze.

The anatase crystals were sensitized with *cis*-di(thiocyanato)-bis(2,2'-bipyridyl-4,4'-dicarboxylate)ruthenium(II) (N3; purchased from Solaronix SA, Switzerland) dissolved in ethanol. The purchased N3 was purified in order to eliminate impurities (the 1 to 2 % of dimer and trimer).[16] The purification procedure is as follows:[16] The received N3 (0.2 g) was dispersed in water (4 ml) and tetrabutylammonium thiocyanate (0.2 g). Tetrabutylammonium hydroxide 30-hydrate (0.82 g) was added to the N3 solution with stirring, and then filtered. The filtered N3 solution was charged on to the column with Sephadex' LH 20 (70 g) gel and eluted with distilled water. The main fraction was collected into a conical flask, and the pH of the solution was adjusted to pH 4.2 with a 0.5M HNO_3. After keeping the solution in a refrigerator at 0°C for 12 hours, the separated solid (N3) was collected by filtration. The solid was dried under vacuum for 12 hours. Yield was approximately 80 %. Stock dye solutions were prepared in various concentrations from 0.37 mM to 38 μM in ethanol. The electrodes were heated in the air to 100 °C overnight prior to the treatment with N3 to remove adsorbed water from the crystal surface. We found that without this procedure the quantity of the adsorbed N3 on the TiO_2 surface was smaller in the previous experiments using nanocrystalline TiO_2 films.[7] After heating, the electrodes were cooled for one minute and then immersed in the dye solution. After soaking overnight, the electrodes were rinsed with ethanol in order to wash out non-chemisorbed N3 and N3 adsorbed to the

Reproduced with permission of the copyright owner. Further reproduction prohibited without permission.

silicon sealant surface. Several experiments demonstrated that longer soaking times in the dye solutions were not found to increase the coverage of N3 on the anatase crystal.

Photocurrent spectra were measured with a Newport 75-W tungsten halogen lamp, a Jarrel Ashe 0.25-m monochromater, a Stanford Research SR 530 lock-in amplifier, SR 540 chopper, and a PAR 174 polarographic analyzer linked to a computerized control and data acquisition system. The light spot from the monochromater was focused down to 0.06 cm^{-2}, and the resulting light intensity was 13 mW cm^{-2} at 530 nm. Between sensitization experiments, adsorbed N3 was removed from the crystal surface by scrubbing with a cotton swab dipped in 2 M NaOH. Photocurrent transients were measured with the argon ion laser by utilizing an AD Instruments MacLab® with Chart® data collection software.

The surface morphology of the crystals was examined with scanning electron microscopy (SEM) and atomic force microscopy (AFM). The atomic force microscope was a Digital Instruments/Veeco with a Nanoscope® IIIA controller and a multimode base. Scanning was done in tapping mode with a J or A piezo scanner. The tips were Ultralever® (Park Scientific Instruments) silicon tips of the force constants of approximately 1.9 N/m. The scan size for surface roughness determination was 500 nm with 512 pixels per scan. The resulting resolution was approximately 1 nm, about the same scale of the N3 molecules.

Reproduced with permission of the copyright owner. Further reproduction prohibited without permission.

3.3. Results and Discussion

3.3.1. Sensitization behavior and surface morphology of the natural anatase crystals

The photocurrent action spectra of the anatase crystals sensitized with N3/ethanol solutions of various concentrations are shown in Figure 3.2. The maximum $IPCE_{max}$ obtained for the Norwegian anatase was 3.2×10^{-4} at 525 nm when the crystal was sensitized with a 0.37 mM N3/ethanol solution. For comparison, the maximum IPCE reported for a synthetic anatase crystal was 1.1×10^{-4} on the (101) face when treated with a 0.3 mM N3/ethanol solution.[15]

More concentrated N3/ethanol solutions could not be used since this is near the maximum N3 solubility. The maximum $IPCE_{max}$ for the Brazilian anatase was measured to be 8.0×10^{-5} on the (101) face at 535 nm when the crystal was sensitized with a 0.2 mM N3/ethanol solution. This is about one quarter of the yield of the (101) face of the Norwegian crystal. Increases in IPCE were not observed when the Brazilian anatase was sensitized with more concentrated N3/ethanol solutions. Also, the same $IPCE_{max}$ value as the $IPCE_{max}$ for the Brazilian anatase (8.0×10^{-5} with a 0.2 mM N3/ethanol solution) was obtained for the Norwegian crystal using a 38 μM N3 solution, an amount almost one fifth of the concentration needed for equivalent sensitization yield for the Brazilian anatase.

The relationship between the concentration of the sensitizing N3 solution that the crystal was treated with and the IPCE is plotted in Figure 3.3.a and b for the Norwegian and Brazilian crystals. The $IPCE_{max}$ data for the Norwegian anatase (Figure 3.3.a) is from Figure 3.2. The relationship

Reproduced with permission of the copyright owner. Further reproduction prohibited without permission.

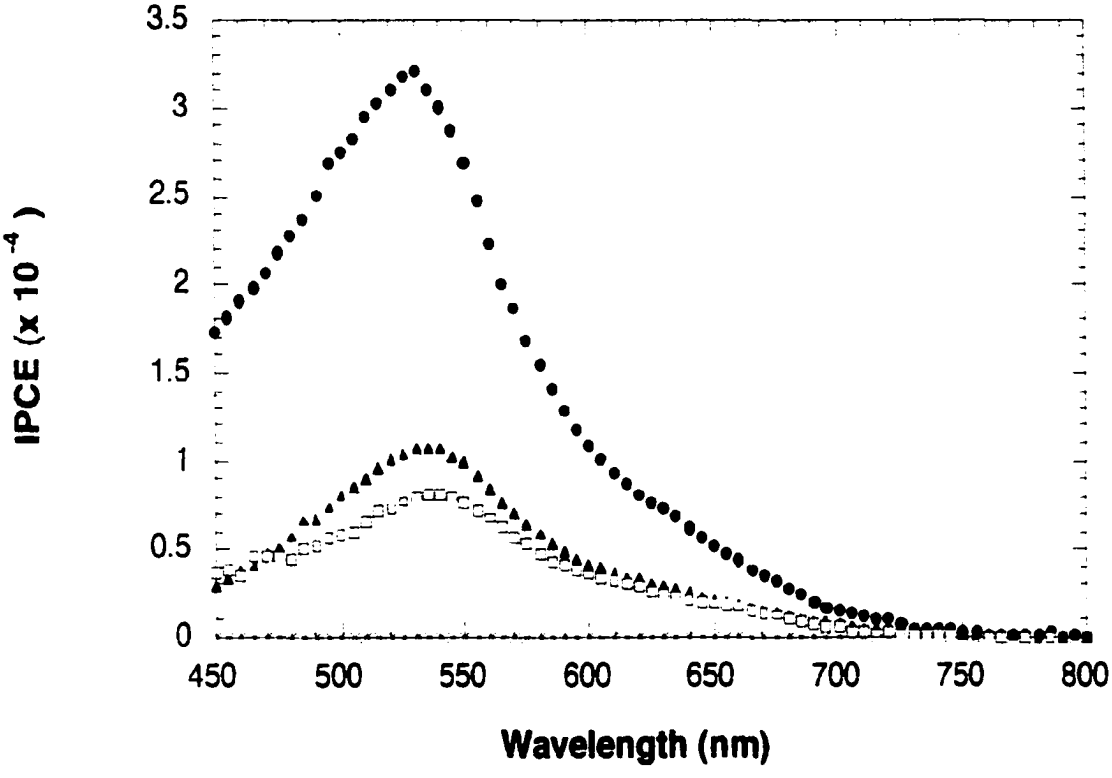

Figure 3.2. Photocurrent spectra of the anatase crystals sensitized with N3 solutions of various concentrations. The top three spectra were taken from the Norwegian anatase, and the spectrum graphed with squares was taken from the Brazilian anatase (the (101) face). The concentrations of the N3/ethanol solutions are the black circles: 0.37 mM, white circles: 0.13 mM, black triangles: 38 μM, and squares: 0.20 mM. The blank spectrum (i.e. without N3) is shown with the crosses taken on the Norwegian anatase. The blank spectrum for the Brazilian anatase is almost identical to this spectrum.

Reproduced with permission of the copyright owner. Further reproduction prohibited without permission.

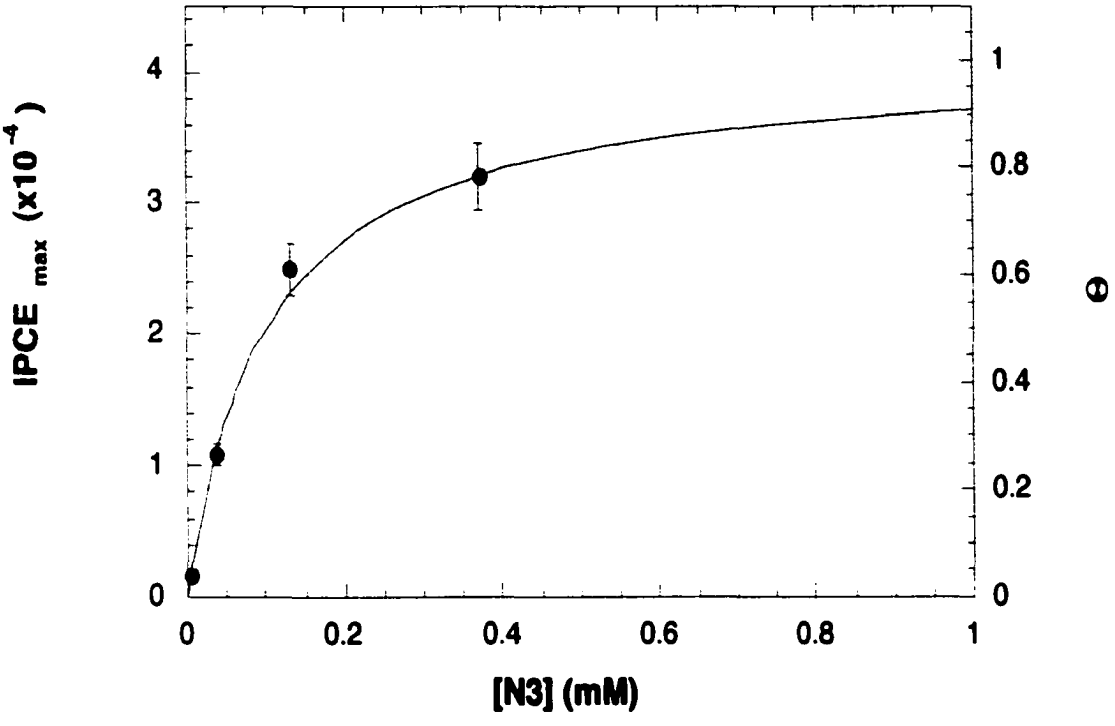

Figure 3.3.a. Plot of the IPCE of the Norwegian anatase vs. the concentration of the N3 solution. The line is the best fit of the Langmuir adsorption equation.

Reproduced with permission of the copyright owner. Further reproduction prohibited without permission.

between the quantity of adsorbed N3 and the concentration of N3 in solution for nanocrystalline TiO_2 films has been described with a Langmuir isotherm.[7] Extending this relationship to the single crystal TiO_2 and assuming that the IPCE is proportional to the quantity of adsorbed N3, the experimental data were fit to a Langmuir adsorption isotherm (Figure 3.3.a) as stated by equation 1.

$$\Theta = KC/(1 + KC) \qquad [1]$$

where Θ is the fractional coverage, K is the adsorption coefficient (M^{-1}), and C is the concentration of N3 in solution (M). Use of a Langmuir isotherm is probably an oversimplification since the assumptions for the derivation of this isotherm are that all sites are equivalent, there is one molecule per site, and there are no interactions between the adsorbed molecules. N3 most likely adsorbs to two or three surface sites.[4-6] Despite these limitations a Langmuir K value is useful for comparing the strength of binding of the different crystals and the nanocrystalline films. The best fit for the Norwegian crystal (101) face was obtained with $K = 9.9 \times 10^3\ M^{-1}$. This value is reasonably close to the value of the adsorption coefficient of N3 to a nanocrystalline TiO_2 film ($2.3 \times 10^4\ M^{-1}$)[7] that has predominately a (101) orientation. Since the relationship between the IPCE and the concentration of N3 in solution fits a Langmuir isotherm reasonably well, if all the adsorbed N3 are equally active for sensitization of the TiO_2, this supports the assumption that the IPCE is proportional to the quantity of adsorbed N3. However, for a dye sensitized nanocrystalline TiO_2 system, we found that the IPCE is not linearly proportional to the quantity of adsorbed N3.[7]

Reproduced with permission of the copyright owner. Further reproduction prohibited without permission.

IPCE values obtained for the Brazilian anatase (Figure 3.3.b) by illuminating with an argon ion laser at 514 nm show that the (101) face of the Brazilian anatase was sensitized about an order of magnitude more than the (001) face of the same crystal. The crystal face dependence of the sensitization efficiency will be discussed later.

One possible explanation for differences in sensitization yield between the different crystals and faces is that the microscopic surface area could be different. Therefore, the surface morphology of the Norwegian and Brazilian anatase crystals was investigated with scanning electron microscopy and atomic force microscopy in order to examine their surface roughness. The scanning electron micrographs of the surfaces of the anatase crystals are shown in Figure 3.4.a and b. The surface of the Norwegian crystal exhibits a step-terrace structure (Figure 3.4.a and b). According to the Laue back reflection measurement, the majority of the surface is composed of terraces of the (101) face. The steps are thought to be the (001) faces judging from the angle between the two faces. The Brazilian crystal habit contains both (101) and (001) faces. The (101) face of the Brazilian crystal also has a step-terrace structure, but it looks different than the Norwegian crystal (Figure 3.4.c and d). The (001) face has a flat surface with many block-like protrusions (Figure 3.4.e and f).

The surfaces of the anatase crystals were also probed with the atomic force microscope by scanning a 500 x 500 nm area. A Digital Instruments software routine was applied to the data in order to determine the roughness on a small scale. The Norwegian anatase had a microscopic surface area for a 500 x 500 nm scan that ranged from 0.251 to 0.267 μm^2 with an average of 0.254 μm^2 for 10 randomly selected spots. The (101) face of the Brazilian

Reproduced with permission of the copyright owner. Further reproduction prohibited without permission.

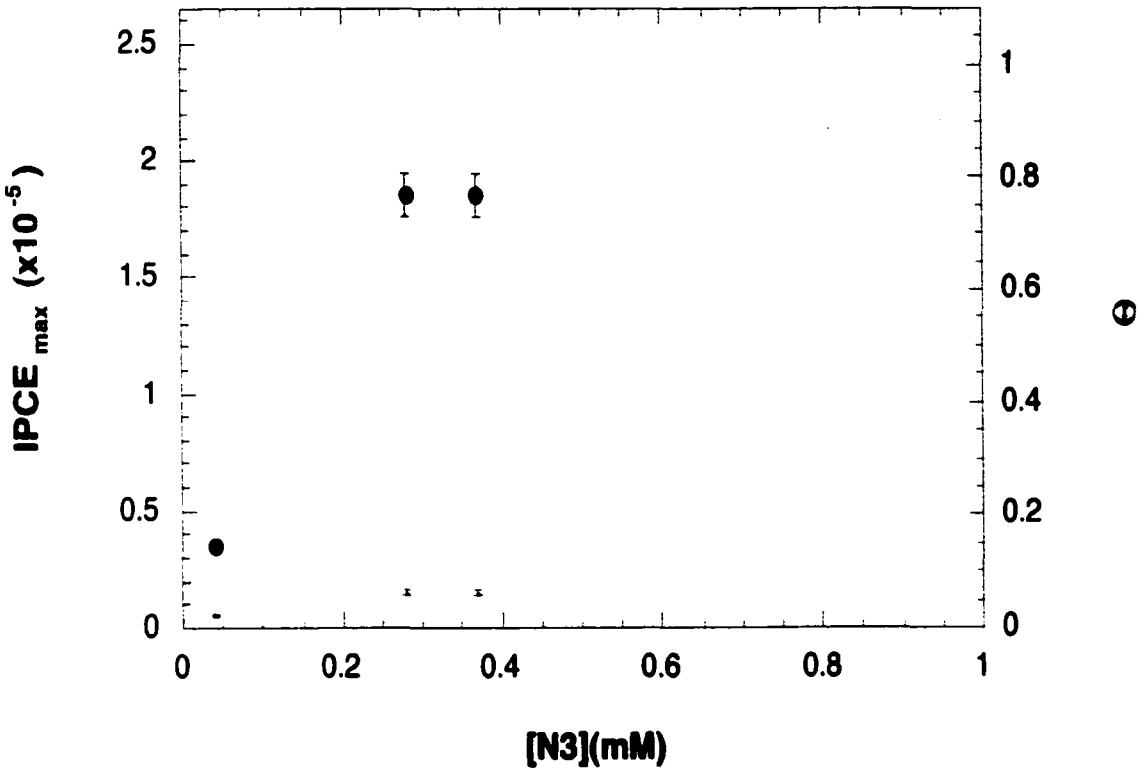

Figure 3.3.b. Plot of the IPCE of the Brazilian anatase vs. the concentration of the N3 solution. Black circles: the (101) face, dots: the (001) face. The line is the best fit of the Langmuir adsorption equation.

Reproduced with permission of the copyright owner. Further reproduction prohibited without permission.

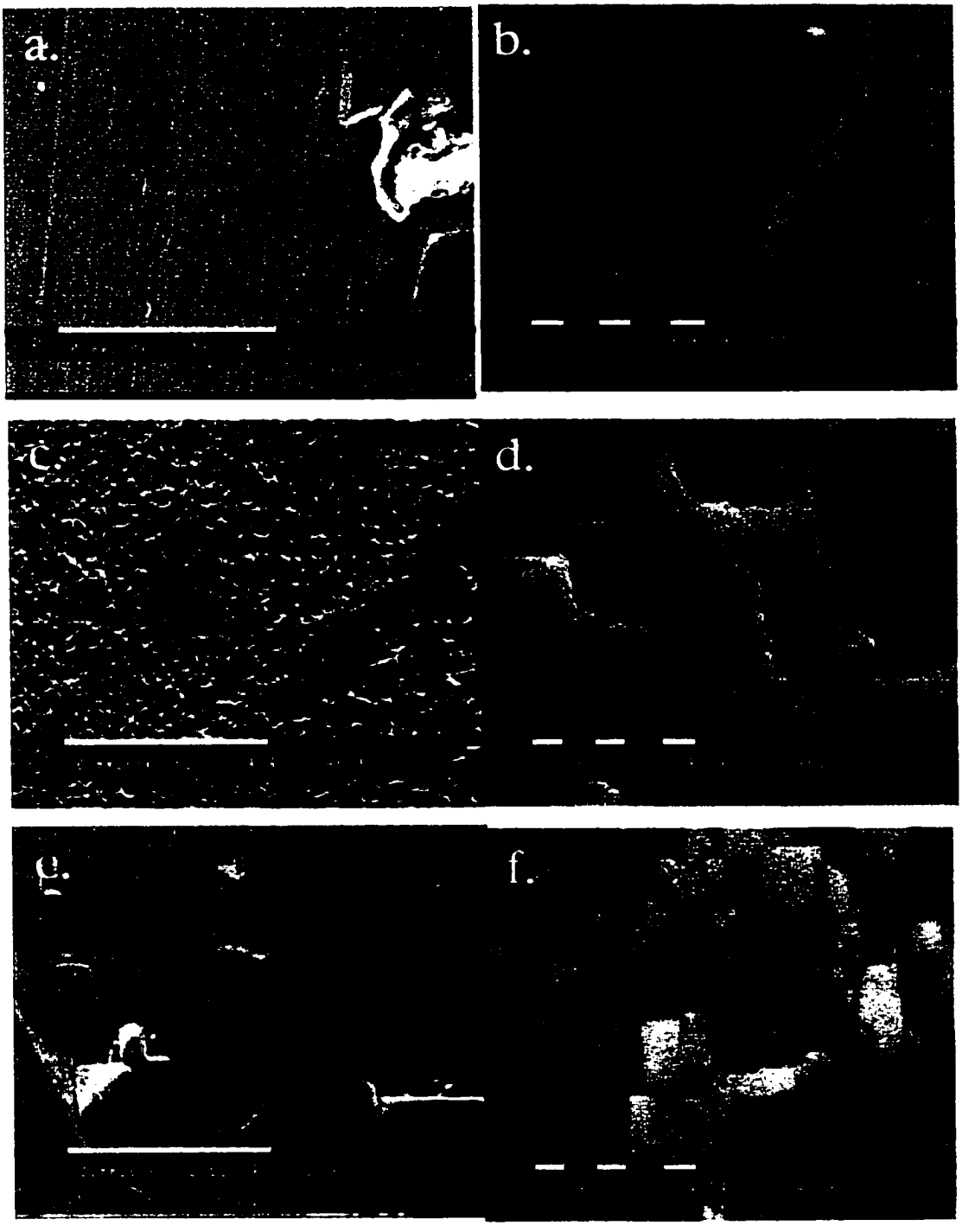

Figure 3.4. Scanning Electron Micrographs of the natural anatase crystals. (a, b) The Norwegian anatase. (c, d) The (101) face of the Brazilian anatase. (e, f) The (001) face of the Brazilian anatase.

Reproduced with permission of the copyright owner. Further reproduction prohibited without permission.

anatase had a microscopic surface area for a 500 x 500 nm scan that ranged from 0.265 to 1.00 μm^2 with an average of 0.395 μm^2 for 15 randomly selected spots. Hence, the surface area of the (101) face of the Brazilian anatase is about 1.56 times on average that of the (101) face of the Norwegian anatase. The (001) face of the Brazilian anatase had a microscopic surface area for a 500 x 500 nm scan that ranged from 0.260 to 0.508 μm^2 with an average of 0.276 μm^2 for 10 randomly selected spots. Thus, the surface area of the (101) face of the Brazilian anatase is about 1.43 times on average that of the (001) face of the same crystal.

The morphological examination indicates that the differences in sensitization efficiency between the crystals and the different faces are not solely the result of the differences in the microscopic surface areas. The (101) face of the Norwegian anatase had a sensitization efficiency four times greater than the (101) face of the Brazilian anatase despite the smaller surface roughness. Also, the (101) face of the Brazilian anatase face was sensitized two to five times more than the (001) face even when considering the surface roughness factors.

The (101) surface of another Norwegian anatase crystal was polished using a series of smaller mesh aluminas with a final polish with colloidal silica. An AFM study revealed that the polishing with colloidal silica did not change the roughness of the crystal surface. Treating the polished surface with a 0.35 mM N3 solution showed an $IPCE_{max}$ of 4.1 x 10^{-4} at 520 nm, slightly greater than that of the unpolished Norwegian anatase crystal (3.2 x 10^{-4} at 525 nm, when treated with 0.37 mM N3 solution).

The adsorption rate of N3 to Norwegian anatase was studied by adding 4.0 μM of N3 directly to the electrolyte (acetonitrile with 15mM KI

Reproduced with permission of the copyright owner. Further reproduction prohibited without permission.

and 1.5 mM I_2). Photocurrent spectra of the Norwegian crystal were then monitored periodically. The purposes of this experiment is to probe the adsorption rate of N3, and to examine in detail if increasing N3 coverage influences the photo action spectrum by monitoring the exact spot on the crystal. At this N3 concentration, the absorption of the incident light by the N3 molecules dissolved in the electrolyte is negligible (less than 1.3 % of the incident light is absorbed by the N3 dissolved in the electrolyte). The electrolyte with N3 added was constantly stirred to promote mass transfer to the surface. A stable photoresponse was achieved in approximately 10 min after N3 addition. The $IPCE_{max}$ versus time after the N3 addition is plotted in Figure 3.5. The $IPCE_{max}$ after about 10 min was approximately one third of the final $IPCE_{max}$. Half of the final $IPCE_{max}$ was reached in 2 hours, and the $IPCE_{max}$ leveled off after about 10 hours. The increase in IPCE observed in this experiment is similar to the adsorption kinetics of N3 to the nanocrystalline TiO_2 film,[7] that was monitored by the disappearance of N3 from an N3/ethanol solution. The similarity of these two rates provides additional support for the assumption that the sensitization yield is proportional to N3 coverage. In our previous paper,[7] we proposed a two step adsorption model, as shown below, for a possible binding mechanism of N3 to nanocrystalline TiO_2.

$$N3_{solution} \rightleftharpoons N3_{surface\,1} \rightleftharpoons N3_{surface\,2}$$

Less strongly bound *Strongly bound*

This scheme illustrates that a N3 molecule attaches to the TiO_2 surface

Reproduced with permission of the copyright owner. Further reproduction prohibited without permission.

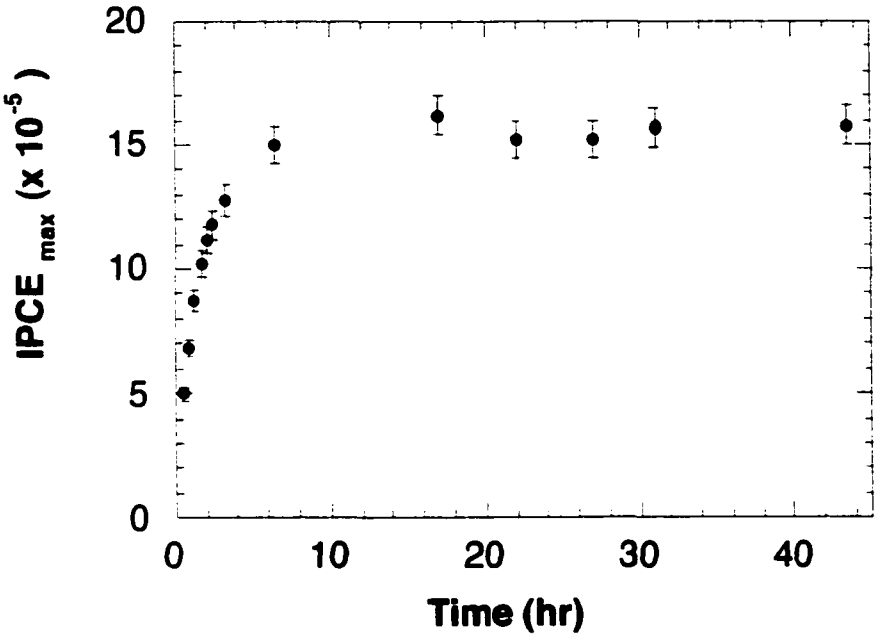

Figure 3.5. Plot of the $IPCE_{max}$ versus time after the injection of a N3/ethanol solution to the electrolyte. Initially the Norwegian crystal was not sensitized, and there was no N3 solution in the electrolyte.

Reproduced with permission of the copyright owner. Further reproduction prohibited without permission.

first with one carboxyl group ($N3_{surface(1)}$) followed by the second carboxyl group ($N3_{surface(2)}$). The initial fast increase in the IPCE (or N3 adsorption) (Figure 3.5) can be explained as the rapid binding of one carboxyl group of a $N3_{solution}$ to a Ti^{4+} site on the TiO_2 surface in the $N3_{surface(1)}$ mode. The following much slower increase in the IPCE (or N3 adsorption) can be rationalized as the increased difficulty of finding binding sites due to a sequential binding of the adsorbed N3 in the $N3_{surface(1)}$ mode with the second carboxyl group.

The IPCE of the Norwegian anatase treated with a 0.35 mM N3 solution (near saturation coverage) was also monitored over 72 hours in an electrolyte (15 mM KI and 1.5 mM I_2 in acetonitrile) containing no added N3. No change in IPCE was observed over this time period. This result indicates that the adsorption appears irreversible in the experimental time scale, even though the N3 solution and the adsorbed N3 are in equilibrium during the adsorption process. The apparently irreversible adsorption may be explained as follows: when one carboxyl group detaches from the crystal surface, the detached carboxyl group is likely to rebind at the same binding site or a different binding site. This is because there are very few species that compete with the detached carboxyl group for the binding sites, and the I^- and I_3^- have much smaller negative charge densities compared with COO^-. On the other hand, adsorbed N3 readily desorbs from a anatase surface into water at pH higher or equal to 7, where OH^- takes over the binding sites from the adsorbed N3.

The resemblance of the adsorption behavior between nanocrystalline TiO_2 films and the Norwegian anatase suggests that the adsorption rate of N3 to anatase is not greatly affected by the size of the crystallites. This resemblance also suggests that the nanoporous morphology of the films

Reproduced with permission of the copyright owner. Further reproduction prohibited without permission.

does not affect the kinetics of the N3 adsorption within the experimental time scale, as was reported in our previous paper.[7] However, the nanocrystalline TiO_2 films used for the adsorption experiments were produced from commercial TiO_2 (P25, Degussa, Switzerland, a mixture of ca. 70 % anatase and 30 % rutile). The adsorption coefficient of N3 may differ between anatase and rutile. The majority of the exposed faces of nanocrystalline anatase produced from P25 (Degussa) are the (101),[17] the predominant face of our Norwegian anatase crystal.

Aggregation of dyes on surfaces often shows large effects on the sensitization spectrum of the dye. We compared the low coverage spectra with the final sensitization spectra ($\Theta = 0.26$) by normalizing the spectra at the maximum sensitization wavelength. All action spectra were superimposible, suggesting no strong aggregation or interactions between adsorbed N3 molecules at these coverages.

3.3.2. Characterization of the bulk properties of the anatase crystals

Several characterization methods were used to investigate the Norwegian and Brazilian anatase crystals in order to investigate the origin of the sensitization differences between these crystals. Mott-Schottky measurements were conducted in order to determine the flat band potentials and dopant densities for the anatase crystals. Mott-Schottky plots within a frequency range of 200 Hz to 10 kHz were straight lines. The flat band potentials were measured to be -6.2 to -2.4 V vs. SCE for the Norwegian anatase, -4.9 to -1.1 V vs. SCE for the Brazilian anatase. Most of these values are physically unreasonable and are several volts negative of the reported value (-0.4 V vs. SCE at pH 1)[15] even after accounting for the shift due

Reproduced with permission of the copyright owner. Further reproduction prohibited without permission.

to the pH of our system (pH 6 for the KI/I_2 electrolyte). The frequency dependence of the flat band potential may be due to surface states, which have a time constant for electron trapping on the order of the frequency of the applied voltage function, or due to an oversimplified equivalent circuit.[18] Much more reasonable values for the flat band potentials were obtained from the onset of photocurrent in the photocurrent-voltage curves presented later. If the Mott-Schottky slopes are reliable, using the dielectric constant of 31,[19] the dopant density for the Norwegian and Brazilian crystals were calculated to be 1.3 to 5.7 x 10^{19} cm^{-3} and 4.3 x 10^{18} to 1.4 x 10^{19} cm^{-3}, respectively, over the frequency range of 200 Hz to 10 kHz. Even if the absolute values of the slopes are unreliable, the relative slopes show that the dopant density of the Norwegian crystal is about five times greater than that of the Brazilian crystal when measured at the same applied frequencies. The appearance of the crystals (i.e. the Norwegian anatase is deep blue-black, and the Brazilian anatase is translucent reddish brown) may be related to the difference in dopant density. Crystals from both locations were found to be n-type, and the doping densities for different crystals from each site were all the same within an order of magnitude.

Photocurrent-voltage curves were measured on natural anatase crystals before and after sensitization with N3 utilizing the argon ion laser (514 nm) as a light source. Both crystals exhibited a sub-bandgap response of 1.1 to 1.5 μA cm^{-2} at 0 V vs. SCE under 7.6 mW (i.e. 0.97 W cm^{-2}) illumination at 514 nm (IPCE: 2.7 to 3.6 x 10^{-6}), indicating the existence of bulk or surface sub-bandgap states. No significant difference in sub-bandgap response was found between the (101) and (001) faces of the Brazilian anatase. The

Reproduced with permission of the copyright owner. Further reproduction prohibited without permission.

photocurrent-voltage curves taken after sensitization are shown in Figure 3.6.a and b. The flat band potentials for the Norwegian and Brazilian crystals were estimated to be about -0.85 and -0.75 V vs. SCE from Figure 3.6.a and b, respectively. These values are reasonable compared with the reported value (-0.4 V vs. SCE at pH 1)[15] taking into account the shift due to the pH of our system (pH 6) (59 mV x ΔpH = 300 mV). Although the magnitudes of the photocurrents are almost 20 times different at 0 V vs. SCE between the crystals, the shapes of the photocurrent-voltage curves are similar; the photocurrents increase rapidly between the flatband potentials and about -0.5 V vs. SCE. At more positive potentials the photocurrents increase more gradually, and are still increasing at 1 V vs. SCE. Dark current is less than 16 nA cm^{-2} (see the caption of Figure 3.6) even at 1 V vs. SCE for both crystals.

The Energy dispersive spectroscopy (EDS) analysis was utilized to determine the impurities that may act as dopants in the crystals. Tungsten, mercury, platinum, and vanadium were detected in the Norwegian crystal in the near surface region, and aluminum, silicon, sulfur, copper, tungsten, mercury, and vanadium were detected in occlusions near the crystal surface. Due to the relatively low intensity of the signals, no attempt at quantitative measurement of the impurity concentrations was made. The EDS analysis of the Brazilian crystal did not detect any other elements besides titanium and oxygen. A dopant density of 10^{19} cm^{-3} results in a calculated percentage of the impurities of about 0.01 mol% when using the specific gravity 3.84 g cm^{-3} and molecular weight for anatase of 79.88 g mol^{-1}.[20] Even though only electrically active impurities are measured with the Mott-Schottky measurements, it is not unreasonable that the impurities for the Brazilian

Reproduced with permission of the copyright owner. Further reproduction prohibited without permission.

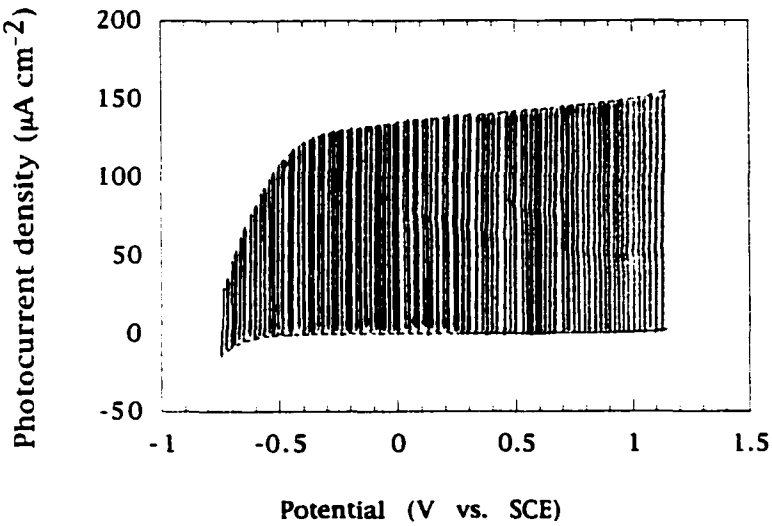

Figure 3.6.a. Photocurrent-voltage curve of the Norwegian anatase crystal sensitized with N3. The concentration of N3/ethanol solution was 0.13 mM. The light source was an argon ion laser (514nm), and the diameter of the beam was 1 mm. The intensity of the beam was 7.6 mW (i.e. 0.97 W cm^{-2}). The measured currents were multiplied with the value of 127 in order to convert to cm^{-2}. However, the dark currents were generated not only from the illuminated area (7.85 x 10^{-3} cm^{-2}) but also from the entire crystal areas exposed to the electrolyte (approximately 1 cm^{-2}). Therefore, the dark currents are inadvertently presented 127 times more than the actual values. The dark currents for both crystals, that are shown approximately 2 μA cm^{-2} at 1.0 V vs. SCE in Figure 3.6.a and b, are actually less than 16 nA cm^{-2}.

Reproduced with permission of the copyright owner. Further reproduction prohibited without permission.

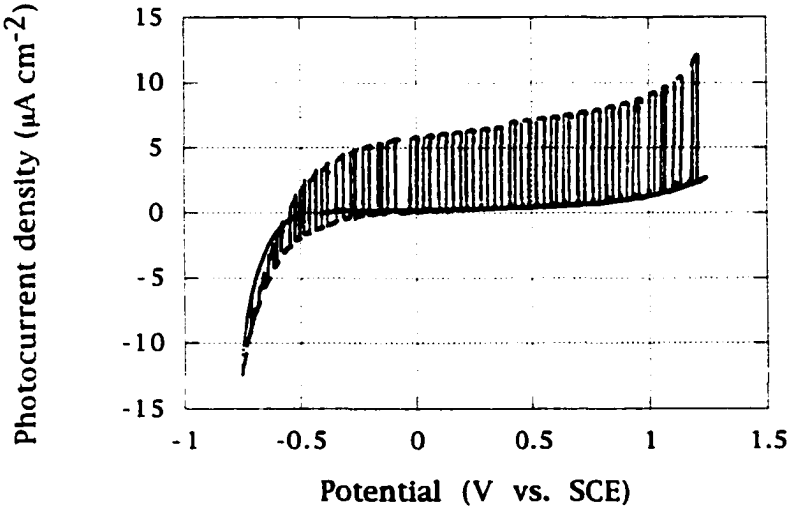

Figure 3.6.b. Photocurrent-voltage curve of the (101) face of the Brazilian crystal sensitized with N3. The concentration of N3/ethanol solution was 0.13 mM. The light source was an argon ion laser (514nm), and the diameter of the beam was 1 mm. The intensity of the beam was 5.1 mW (i.e. 0.64 W cm^{-2}). The measured currents were multiplied with the value of 127 in order to convert to cm^{-2}. However, the dark currents were generated not only from the illuminated area (7.85 x 10^{-3} cm^{-2}) but also from the entire crystal areas exposed to the electrolyte (approximately 1 cm^{-2}). Therefore, the dark currents are inadvertently presented 127 times more than the actual values. The dark currents for the both crystal, that are shown approximately 2 μA cm^{-2} at 1.0 V vs. SCE in Figure 3.6.a & b, are actually less than 16 nA cm^{-2}.

Reproduced with permission of the copyright owner. Further reproduction prohibited without permission.

crystal, 4.3×10^{18} to 1.9×10^{19} cm^{-3} with the Mott-Schottky measurements, were not detected with EDS.

One possible explanation for the greater $IPCE_{max}$ for the Norwegian (101) face over the Brazilian (101) face may be the difference in the dopant densities. According to the Mott-Schottky measurements, the Norwegian crystal has a dopant density about five times higher than the Brazilian crystal. The higher dopant density makes the space charge region narrower, resulting in higher electric field gradient and then a greater driving force for injected electrons to be driven away from the surface. The same tendency was reported for other materials and predicted by the one-dimensional Onsager model by Spitler.[21] The slow increase of sensitization current with increased depletion in the semiconductor (Figure 3.6.a and b) can be explained by increased driving force for injected electrons not to be trapped by the surface states and recombine with I_3^- or oxidized N3.

3.3.3. Discussion on the face dependence of the dye sensitization

Recently, the orientation dependence of charge transfer processes on anatase single crystals was reported.[22] Water reduction and photooxidation was found to occur at slightly more negative potentials for the (001) surface than for the (101) surface.[22] Lithium insertion was observed to be more favorable on the (001) surface than the (101) surface.[22] The difference in the reaction potentials was explained by the more negative flatband potential for the (001) surface due to the different chemisorption of water on the crystal surface.[23] The difference in

Reproduced with permission of the copyright owner. Further reproduction prohibited without permission.

lithium insertion was rationalized by the more open structure of the anatase lattice in the c axis direction.[22] The orientation dependence of photochemical reactions on rutile surfaces has also been reported.[24] The (101), (111) and (001) rutile orientations were found to have greater rates of photoreduction of Ag^+ to Ag metal from an aqueous solution than the (100) and (110) orientations.[24] The orientation dependence of the photochemical reaction rates was explained with the orientation dependence of the surface structure, surface chemistries, and space charge potentials. The surface orientation determines the microscopic surface area, the Ti site density, and the Ti coordination of the specific facets. The surface chemistries affect the mechanisms of adsorption and desorption or the surface specific reactions taking place. In studies of rutile single crystals with the (001) orientation, it was observed that the coordination environment of individual Ti ions was the primary determinant of the product distributions in the photooxidation of primary alcohols and carboxylic acids.[25, 26] Space charge potentials, which can play a significant role in determining the photochemical reaction rates, are dependent on dielectric constants, which are known to differ with crystallographic direction (*i.e.* for rutile, ε = 173 or 174 parallel to [001] and 89 or 86 parallel to [100] or 174 and 86).[27, 28]

The different sensitization yields between the (101) and (001) faces can be attributed to differences in N3 adsorption to the different faces. The adsorption could be related to the differences in the spacing of the two or more binding sites needed for strong N3 surface binding. There are several possible binding modes for the carboxyl group of N3 to the

Reproduced with permission of the copyright owner. Further reproduction prohibited without permission.

unsaturated surface Ti atoms, an ester-like linkage[29] or bridging configuration (*i.e.* two Ti^{4+} sites bound to one carboxyl group)[30]. The distances between Ti^{4+} sites are critical for the bridging mode. The (101) surface of anatase has half penta/half hexacoordinate Ti atoms (Figure 3.7.a.i) while the (001) surface of anatase has all pentacoordinate Ti atoms (Figure 3.7.a.ii). Only pentacoordinate Ti atoms can act as binding sites. The shortest distance between the pentacoordinate Ti atoms is 3.78 Å (the a-axis dimension) for the both surfaces. Judging from the bond lengths of Ti-O and C-O and the angles of Ti-O-C and O-C-O, N3 can bind in the bridging mode to both surfaces.[6] The density of pentacoordinate Ti on the (001) surface is 1.3 times higher than that of the (101) surface. When two carboxyl groups are involved in binding, there are three possible combinations of carboxyl groups.[6] These three combinations are (i) two carboxyl groups are of the same bipyridyl ligand (Figure 3.7.c.i), (ii) two carboxyl groups are in the long molecular axis (Figure 3.7.c.ii), and (iii) two carboxyl groups are in the short molecular axis (Figure 3.7.c.iii).[6] The distances between O atoms which can be involved in binding are 6.2 Å, 10.0Å, and 9.8 Å, respectively.[6] Distances between pentacoordinate Ti sites close to the distances between the O atoms of the carboxyl groups are 5.4 Å, 7.6 Å, 7.6 Å, 10.2 Å, and 10.7 Å for the (101) surface (Figure 3.7.b.i), and 5.4 Å, 7.6 Å, and 10.7 Å for the (001) surface (Figure 3.7.b.ii). By comparing the distances between O atoms and the distances between pentacoordinate Ti sites, the binding with two carboxyl groups of the same bipyridyl ligand (Figure 3.7.c.i) seems to be difficult on either surface. The smallest differences in the distances are 0.75 Å on the (101) face and 0.85 Å on the

Reproduced with permission of the copyright owner. Further reproduction prohibited without permission.

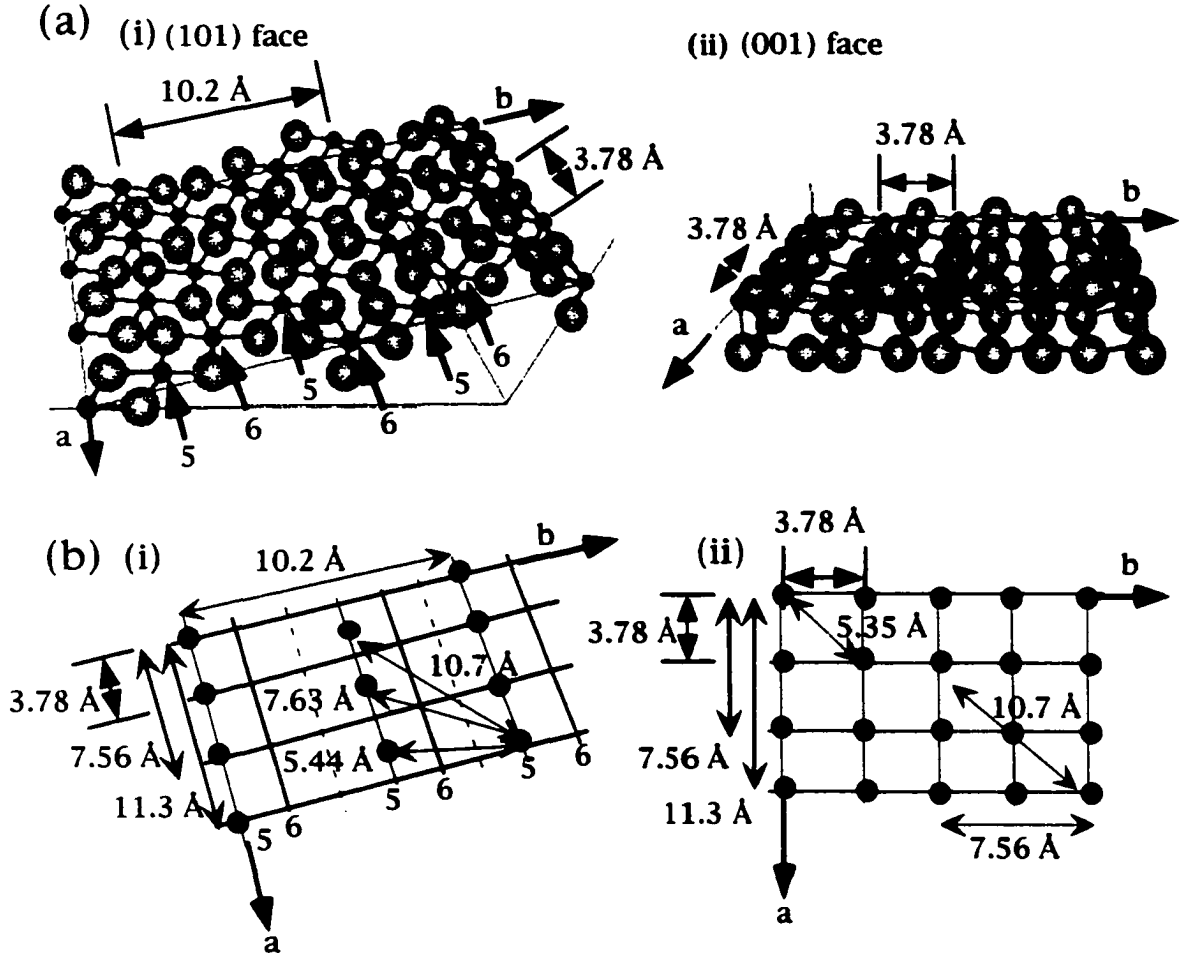

Figure 3.7.a & b. Crystal structure models of anatase and the distances between Ti sites. (a) Crystal structure models of anatase, side views. Small black spheres are Ti, and large grey spheres are O. The numbers with arrow are the coordination numbers of Ti's of the row (*i.e.*, 5: pentacoordinate Ti; 6: hexacoordinate Ti). (i) the (101) surface, (ii) the (001) surface. (b) The distances between pentacoordinate Ti sites. Black dots are pentacoordinate Ti. The numbers near the top are the coordination numbers of Ti's of the row (*i.e.*, 5: pentacoordinate Ti; 6: hexacoordinate Ti). The broken lines represent no Ti's in the row. (i) The (101) surface has a lattice of dimensions |a| = 3.78 Å (equals to a or b of the anatase crystal) and |b| = 10.2 Å (corresponds to the |a + c| of the anatase crystal).[6] Distances between adsorption sites close to the distances between the O atoms of the carboxyl groups are 5.45 Å (|0.5a + 0.5b|), 7.63 Å (|1.5a + 0.5b|), 10.2 Å (|b|), and 10.7 Å (|2.5a + 0.5b|). (ii) The (001) surface has a lattice of dimensions |a| = |b| = 3.78 Å. Distances between adsorption sites close to the distances between the O atoms of the carboxyl groups are 5.35 Å (|a + b|), 7.56 Å (|2a|), and 10.7 Å (|2a + 2b|).

Reproduced with permission of the copyright owner. Further reproduction prohibited without permission.

(c)

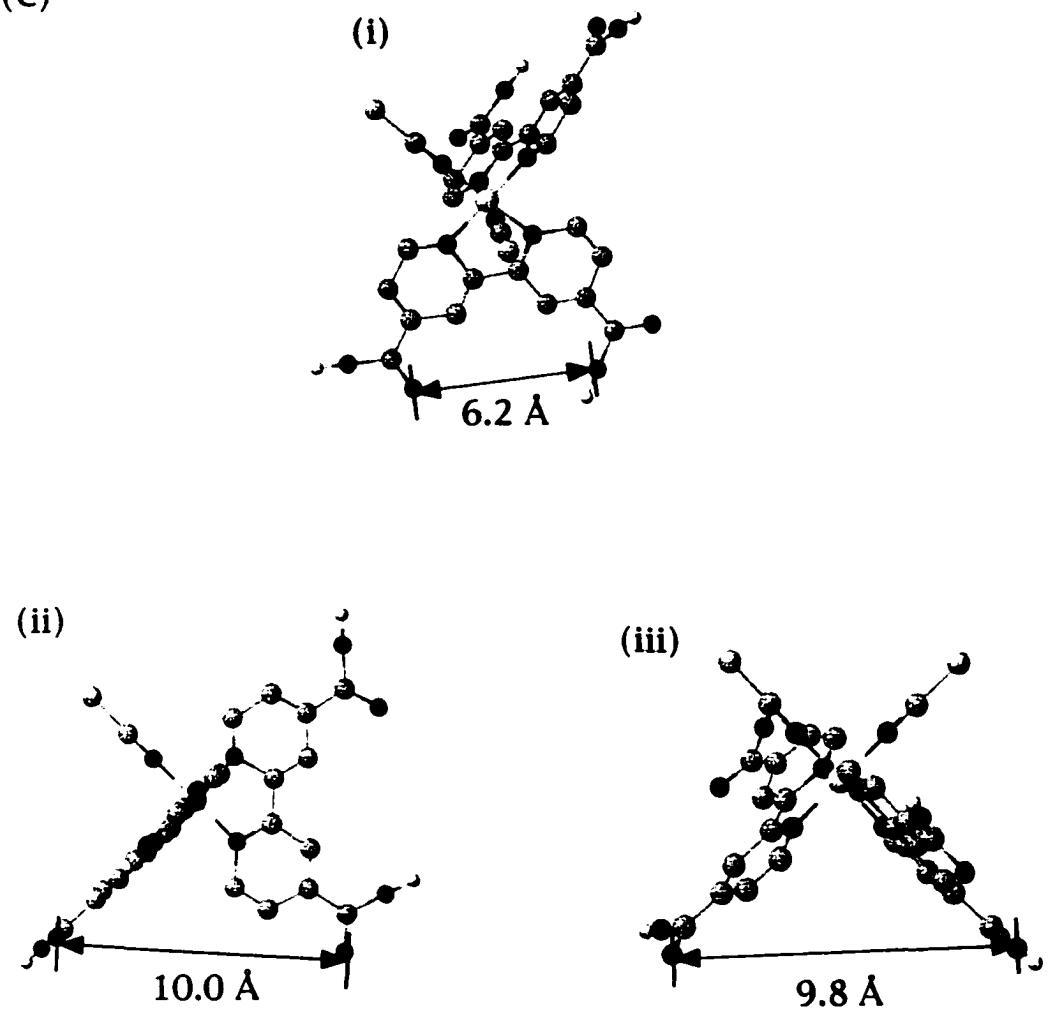

Figure 3.7.c. Possible combinations of carboxyl groups of N3 for bidentate chelating binding.[6] Gray spheres: carbon; red spheres: oxygen; blue spheres: nitrogen; yellow spheres: sulfur; light gray sphere (at the center of the molecules): ruthenium. (i) two carboxyl groups are of the same bipyridyl ligand, (ii) two carboxyl groups are in the long molecular axis, (iii) two carboxyl groups are in the short molecular axis.

Reproduced with permission of the copyright owner. Further reproduction prohibited without permission.

(001) face. These differences are too large for unstrained bond formation. Alternatively, the binding with two carboxyl groups from different bipyridyl ligands (Figure 3.7.c.ii and iii) is possible on the (101) surface. The smallest differences between the distances are 0.2 Å for binding with two carcboxyl groups along the long molecular axis (Figure 3.7.c.ii), and 0.4 Å for binding with two carboxyl groups along the short molecular axis (Figure 3.7.c.iii). The (001) surface does not easily accommodate these modes of N3 binding, since the smallest differences in the distances are 0.7 Å and 0.9 Å. Thus, the greater sensitization yield of the (101) surface may be explained with the stronger binding of N3 in bidentate modes, whereas on the (001) surface the N3 can bind predominately with only one carboxyl group.

The different faces will have different densities and energy levels of surface states due to the different termination of the surface. These differences in surface states may contribute to different surface recombination rates. However, a recent publication showed very similar efficiencies and current voltage curves for water oxidation by UV illumination of the (101) and (001) faces of synthetic anatase crystals,[22] indicating that the surface recombination velocity of photogenerated valence band holes are not radically different between the two faces.

3.3.4. Sensitization photocurrent transients

A typical rise and decay of the photocurrent for the Norwegian anatase sensitized with a 0.13 mM N3 solution, which corresponds to 0.6 monolayer N3 coverage (Figure 3.3.a), was monitored under the illumination with the argon ion laser (514 nm). The rise time was

Reproduced with permission of the copyright owner. Further reproduction prohibited without permission.

defined as the time necessary to reach 63 % (i.e. $1-e^{-1}$) of the steady state photocurrent.[31] The light was manually blocked, resulting in a rise time and decay time of 0.25 ms for the light pulse. The rise time of the sensitized photocurrent was measured to be 2 ms at 0.97 W cm^{-2} and 19 ms at 15 mW cm^{-2} (Figure 3.8.a and b). These transients are more than 6 orders of magnitude slower than those reported for single crystals, which is in the sub-picosecond time-scale.[32] These transients are in the same time scale as those reported for nanocrystalline TiO_2 films.[33-36] The slow electron transport through nanocrystalline TiO_2 films has been explained by two unique aspects of the electron transport through nanocrystalline films. The first aspect is the electron transport through nanocrystalline TiO_2 films is driven solely by the diffusion of electrons. This is because the nanocrystallites do not have enough ionized impurities to form a depletion layer inside the particles, resulting in the absence of an electrical field that drives the electron transport through the single crystals.[37] The diffusion of electrons through the nanocrystalline film is slower than in single crystals because of the scattering at grain boundaries. The second aspect is that trapping and detrapping[38, 39] of electrons in bulk or surface states plays a significant role in the electron transport process. Because of the interpenetration of the electrolyte and nanosize particles, the nanocrystalline film has a greater number of surface states when compared to a single crystal. The photocurrent reaches a steady state when the trapping and detrapping of electrons at all the surface states reaches a steady state. Therefore, the growth and decay of the photocurrent of the nanocrystalline film is very slow. It appears that the

Reproduced with permission of the copyright owner. Further reproduction prohibited without permission.

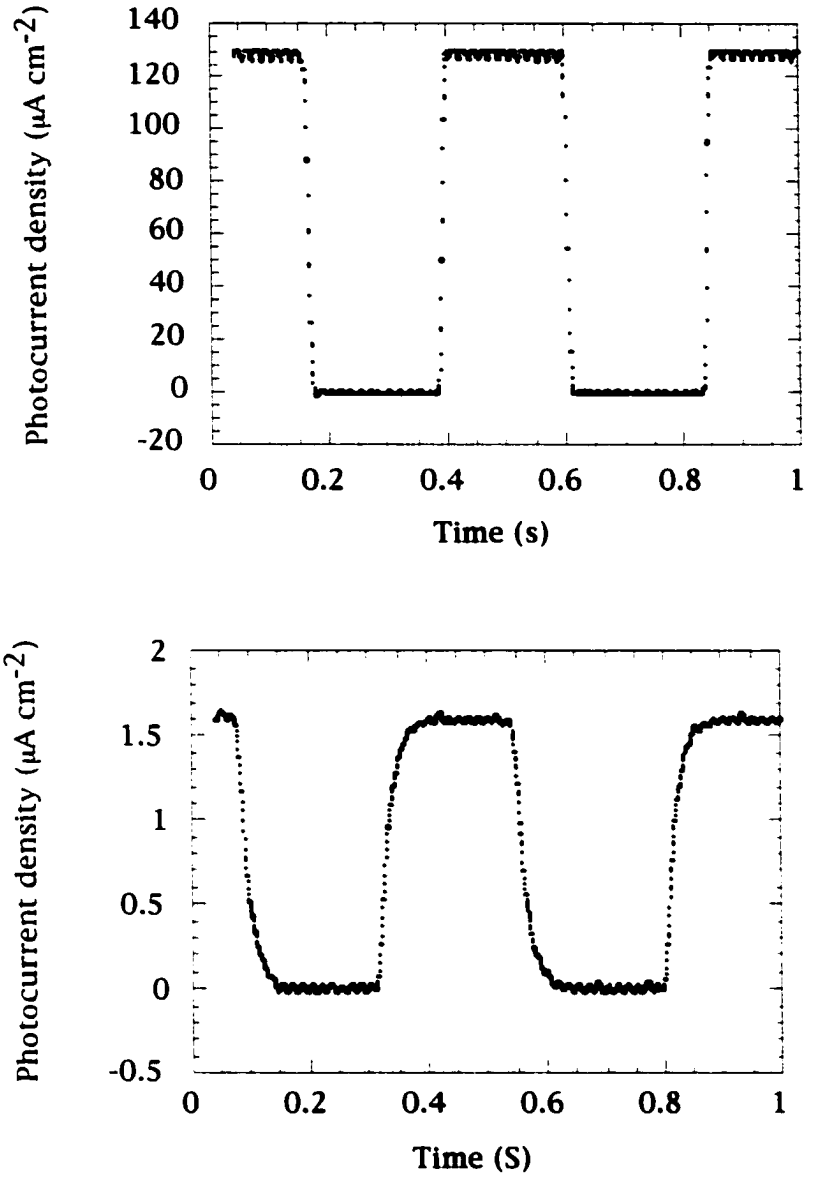

Figure 3.8. Photocurrent transients of the Norwegian anatase recorded under monochromatic (514 nm) illumination. The concentration of the N3 solution was 1.3 mM. The light intensity was 0.97 W cm^{-2} (a) and 15 mW cm^{-2} (b).

Reproduced with permission of the copyright owner. Further reproduction prohibited without permission.

slow growth and decay of the photocurrent for the Norwegian anatase indicates the involvement of trapping and detrapping mechanisms. Since the Norwegian anatase is a naturally formed crystal, the impurities or defects inside of the crystal may be acting as traps.

The relationship between the rise time and the light intensity is shown in Figure 3.9. The rise time of sub-bandgap photocurrent (i.e. without the dye) was much slower (~20 ms) because of the slow trap filling due to the low absorption of photon and subsequent low electron flux. The dye sensitization shortened the rise time, which was almost independent of surface coverage and was 2 to 2.5 ms at 0.3 W cm^{-2}. However, at lower surface coverages, the rise time was significantly longer: 6 ms at 0.3 W cm^{-2}. A light intensity dependence of rise time has also been reported for nanocrystalline TiO_2 films.[35, 40] The shortening of the rise time with the higher light intensity is explained by the faster filling of the traps with the higher photon and subsequent electron flux. The dye coverage dependence of rise time can also be explained by the faster trap filling at the higher dye coverage since there is a higher photocurrent. The observed light intensity dependence and dye coverage dependence of rise time for the Norwegian anatase is consistent with the involvement of a trapping/detrapping mechanism in the electron transport in the Norwegian anatase as illustrated in Figure 3.10. Assuming the rate of electron injection (r_{inj}) is constant, the rate of trapping the injected electrons (r_{trap}) is first order with the number of vacant traps. Therefore, during the initial stages of filling the traps, the rate of trapping (r_{trap}) will be competitive with the rate of the injected electrons escaping from the surface (*i.e.* r_{esc} is proportional to photocurrent). Since the lifetime of

Reproduced with permission of the copyright owner. Further reproduction prohibited without permission.

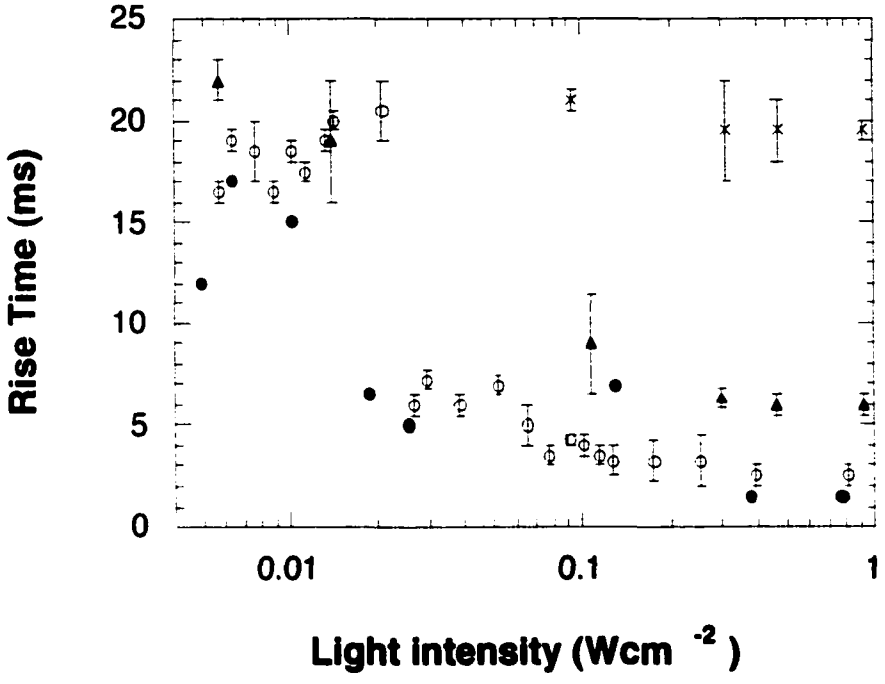

Figure 3.9. Plot of rise time of the dye sensitization photocurrent for the Norwegian anatase versus light intensity. The concentration of N3 solutions are; black circles: 0.31 mM, white circles: 0.13 mM, triangle: 20 μM, crosses: not sensitized.

Reproduced with permission of the copyright owner. Further reproduction prohibited without permission.

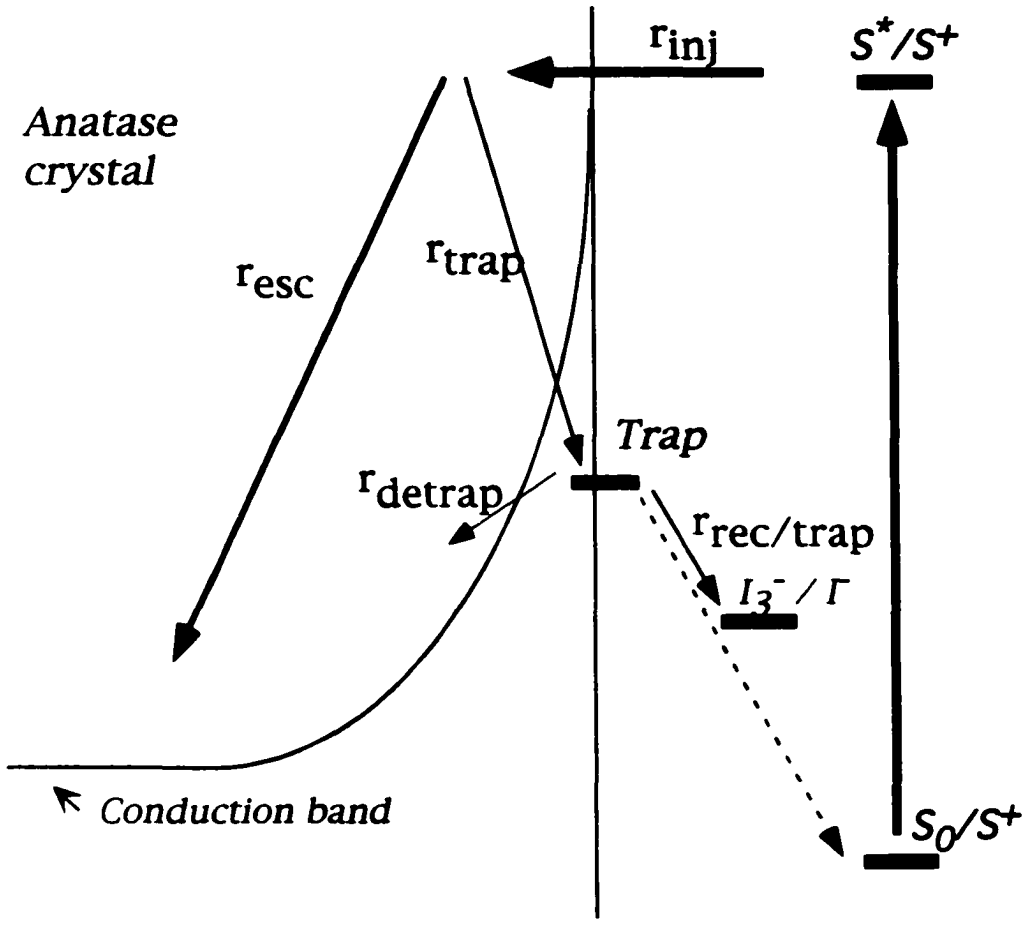

Figure 3.10. The trapping/detrapping mechanism involved in electron transport in the Norwegian anatase crystal. S^*, S^+, and S_0 are the excited state, the oxidized state, and the ground state of the dye, respectively. r_{inj}: electron injection rate to the conduction band of the anatase crystal from the excited dye; r_{esc}: escape rate of injected electrons to the bulk; r_{trap}: trapping rate of injected electrons by the traps; r_{detrap}: detrapping rate to the TiO_2 conduction band. $r_{rec/trap}$: recombination rate of trapped electron at the traps with I_3^- or oxidized dye.

Reproduced with permission of the copyright owner. Further reproduction prohibited without permission.

the electrons in the traps is rather long, the traps fill with electrons and so the number of empty traps decreases and so the rate of trapping (r_{trap}) also decreases until a steady state photocurrent is reached. Since the rate of detrapping the electrons into the TiO_2 conduction band (r_{detrap}) is first order with the number of the trapped electrons, the detrapping rate (r_{detrap}) must be considerably smaller than the rate of trapping even when all the traps are filled.

The possibility that the N3 is bleached at the higher light intensities must be considered. The linear relationship of photocurrent with light intensity, Figure 3.11, shows that bleaching is not significant in this system. Moreover, a monolayer coverage of N3 is about 9.2×10^{-11} mol cm^{-2} as explained later,[15] therefore, the quantity of N3 is calculated to be 5.5×10^{13} molecules cm^{-2}. When the light intensity is 1 W cm^{-2}, the flux of photons of 2.4 eV (514 nm) is calculated to be 2.6×10^{18} photons $s^{-1} cm^{-2}$. Since the reduction of the oxidized N3 occurs on a time scale of 10^{8} s^{-1},[2] a light intensity of 1 W cm^{-2} should not bleach the N3.

3.3.5. Comparison of sensitization behavior between the anatase natural crystals and nanocrystalline TiO_2 films

The quantity of adsorbed N3, the IPCE, the optical absorbance, the light harvesting efficiency (LHE), and the absorbed photon to current efficiency (APCE) for the Norwegian anatase and the TiO_2 nanocrystalline film were compared. This comparison is useful to see if the high performance of the TiO_2 nanocrystalline films can be simply attributed to their high surface areas. The data for the nanocrystalline films are from

Reproduced with permission of the copyright owner. Further reproduction prohibited without permission.

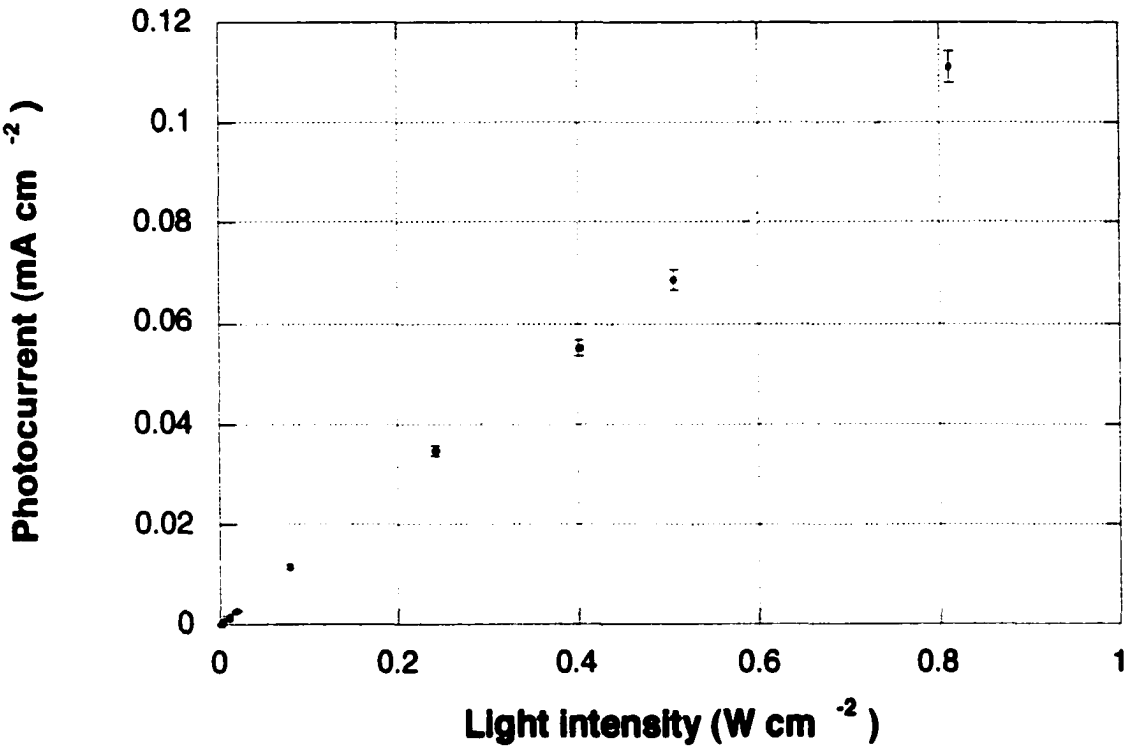

Figure 3.11. Plot of photocurrent versus light intensity. The light source was Ar ion laser (514 nm). The slope of the line corresponds to a quantum yield of 3.3×10^{-4}.

Reproduced with permission of the copyright owner. Further reproduction prohibited without permission.

our previous work.[7] These values are similar to other published values.[2] The results of the comparison are tabulated in Table 3.1. First, the relationship between the quantity of adsorbed N3 and the IPCE was examined. The maximum possible quantity of the adsorbed (and illuminated) N3 for the Norwegian anatase was calculated by dividing the illuminated area of the crystal (0.06 cm^2) with the projected molecular area of N3 (180 $Å^2$).[7, 15] This assumes a close packed monolayer of N3. The quantity of the adsorbed (and illuminated) N3 for the nanocrystalline TiO_2 films was calculated for the illuminated area (0.06 cm^2) from the quantity of the N3 adsorbed to the entire film (1.8 cm^2), which was obtained from a direct measurement of the uptake of N3 by the nanocrystalline film.[7] The comparison indicates that the nanocrystalline TiO_2 film adsorbed approximately 900 times more N3 molecules than the Norwegian anatase on a geometric surface area basis. However, the nanocrystalline TiO_2 film exhibited an $IPCE_{max}$ approximately 2300 times greater than that of the Norwegian anatase.

Second, the absorbance of adsorbed N3 and the LHE were obtained in order to examine the internal conversion efficiencies of the both systems. LHE (λ) is the fraction of the incident photons that are absorbed by the N3 and is calculated from equation 2.

$$LHE(\lambda) = 1 - 10^{-Abs(\lambda)} \qquad [2]$$

where $Abs(\lambda)$ is the optical absorbance of the adsorbed N3. The maximum absorbance of the N3 adsorbed on the nanocrystalline TiO_2 film was previously measured to be 0.7 with diffuse reflectance spectroscopy.[7] The absorbance of the N3 adsorbed on the Norwegian anatase was calculated

Reproduced with permission of the copyright owner. Further reproduction prohibited without permission.

Table 3.1. Comparison of the Norwegian anatase single crystal with anatase nanocrystalline films.

	Nanocrystalline Film	Single Crystal	Ratio (Nano-crystalline Film/ Single Crystal)
Adsorbed N3 (*mol*)	5.0×10^{-9}	5.5×10^{-12} *1	900
$IPCE_{max}$	6.2×10^{-1} (8.6×10^{-1})*2	3.2×10^{-4} (1.1×10^{-3})*3	2300 (750)
$Absorbance_{max}$	0.7	0.0013	-
LHE_{max}	0.8	0.003	260
$APCE_{max}$	0.77 (1.0)*2	0.11 (0.37)*3	7.0 (2.7)

*1 Assuming close packed monolayer coverage.

*2 The numbers in the perentheses were calculated from ref. 2.

*3 The numbers in the perentheses were calculated from ref. 15.

Reproduced with permission of the copyright owner. Further reproduction prohibited without permission.

from the following equation.

$$Abs(\lambda) = \Gamma \times \sigma(\lambda) \qquad [3]$$

where Γ is the surface coverage in mol cm^{-2}, and $\sigma(\lambda)$ is absorption cross section ($cm^2\ mol^{-1}$).[15] The surface coverage was estimated to be 9.2×10^{-11} mol cm^{-2} by using the molecular area of 180 $Å^2$.[15] The absorption cross section ($\sigma(\lambda)$) was calculated as $1.4 \times 10^7\ cm^2\ mol^{-1}$ at 534 nm by using the coefficient of the absorption maximum for N3 dissolved in ethanol ($1.42 \times 10^4\ M^{-1}\ cm^{-1}$ at 534 nm),[2] assuming that the absorption coefficient of N3 does not change upon the adsorption to the anatase surface.[1] Equation 2 yields a LHE_{max} of 0.8 for the nanocrystalline TiO_2 film and 0.003 for the crystal. The ratio of the LHE_{max} was 260, which is about one third of the ratio of the amount of adsorbed N3 to the $IPCE_{max}$. This smaller ratio was expected because the N3 on the illuminated side of the nanocrystalline film can absorb only the transmitted portion of the incident light. In

---

[1] Actually, the conduction band of TiO_2, which is a π^* orbital derived from Ti 3d orbitals, may overlap with the π and π^* orbitals of the bipyridyl ligands of N3.[41] And, the absorption peak (at 534 nm) is assigned to the electron transfer from the 3d orbitals of the Ru (II) to the π^* orbital of the bipyridyl ligands (MLCT). Therefore, the change of the absorption coefficient of N3 might be happening from the solution form to the adsorbed form. Yet, we consider that the use of the estimated values of Γ and $\sigma(534)$ is reliable for the purpose of obtaining the absorbance of the N3 adsorbed to the Norwegian anatase for the following reason. The Abs_{max} of the N3 adsorbed to the Norwegian anatase was calculated as 0.0013 from equation 2 by using the estimated values. Meanwhile, Kavan et al. spectrophotometrically measured the absorbance of ten monolayers of N3 adsorbed on five stacked rutile wafers,[15] and obtained the value of 0.0012 for one monolayer N3. Unfortunately, these types of measurements cannot be carried out for anatase because single crystal anatase wafers are not available, and our natural crystals have a significant absorbance from impurities. The agreement of the absorbance values seems to ensure the credibility of the calculated absorbance even if the adsorbed surfaces are $absorbance_{max}$ calculated from the estimated Γ and $\sigma(534)$.

Reproduced with permission of the copyright owner. Further reproduction prohibited without permission.

other words, one thousand layers of N3 will not absorb one thousand times more photons than one layer of N3 can. Also, all the adsorbed N3 in the nanocrystalline film are not equally active in absorbing light as they are on the single crystal. Finally, the APCE was compared. The APCE consists of the injection efficiency of photo-generated electrons to the conduction band of TiO_2 and the collection efficiency of the injected electrons at the back contact. Equation 4 describes the relationship between IPCE(λ), LHE(λ), and APCE(λ).

$$IPCE(\lambda) = LHE(\lambda) \times APCE(\lambda) \quad [4]$$

By substituting equation 2 into equation 4, APCE(λ) is calculated from equation 5.

$$APCE(\lambda) = IPCE(\lambda) / (1 - 10^{-Abs(\lambda)}) \quad [5]$$

The calculated $APCE_{max}$ was 0.77 for the nanocrystalline film and 0.11 for the Norwegian anatase. The ratio of the two $APCE_{max}$ is 7.0, indicating greater charge injection and/or collection efficiencies of the nanocrystalline film than those of the single crystal. The greater APCE for the nanocrystalline system is quite counterintuitive because a greater number of surface states and the absence of a space charge layer are expected to lower the APCE of nanocrystalline film. Surface states are considered to be responsible for the recombination of photo-injected electrons with the oxidized redox couple or oxidized dye.[18, 42] A space charge layer provides a driving force for photo-injected electrons to travel to the back contact, therefore, without the driving force to escape from the surface states, the injected electron in the nanocrystalline films may experience more trapping by surface states and recombination.

Reproduced with permission of the copyright owner. Further reproduction prohibited without permission.

Hence, the nanocrystalline morphology should reduce the collection efficiency of injected electrons. However, a greater APCE for nanocrystalline TiO_2 films had also been noted by Kavan, et al.[15] For comparison, the authors assumed the APCE for nanocrystalline films to be one. The ratio of $APCE_{max}$ for their data was calculated as 2.7 as shown in Table 3.1.

The high performance of sensitized nanocrystalline TiO_2 films, despite their proportionally smaller light harvesting efficiency, was theorized to involve a greater APCE than that of the single crystal. The origin of this counterintuitive result was also discussed by Kavan et al.[15] They emphasized the importance of surface morphology in the performance of these types of solar cells by referring to a study on SnS_2 single crystals.[43] The study on SnS_2 reported the increases in photo response upon etching the atomically smooth van der Waals planes. The increases were much more than the amounts explainable simply by the increased surface areas. Similarly, the increase in the IPCE upon changing the morphology of a TiO_2 crystal from a single crystal to nanocrystallites cannot be rationalized simply by the increased surface area because the light harvesting efficiency of the nanocrystalline film did not increase proportionally to the increase of the surface area.

So, why is the APCE greater for roughened surfaces or nanocrystallites? As explained previously, it is difficult to believe that the recombination of the injected electrons with the I_3^- and/or the oxidized dye occurs less frequently in a nanocrystalline film than in a single crystal. One conceivable origin of the greater APCE for the nanocrystalline films

Reproduced with permission of the copyright owner. Further reproduction prohibited without permission.

is in the electron injection process. The efficiency of injecting electron from N3 to anatase nanocrystallites may be higher than to larger anatase single crystals. The electron injection efficiency from a *cis*-diaqua bis(2,2'-bipyridyl-4,4'-dicarboxylate) ruthenium(II) to the nanocrystalline TiO_2 films has been reported to be near 100 %.[44] Therefore, the electron injection efficiency from the N3 to the nanocrystalline TiO_2 films may be close to 100 %. On the other hand, a direct measurement of the electron injection efficiency for anatase single crystals has not yet been reported. Surface atoms, especially at steps of atomic height, kinks in the steps, and defect sites, experience large changes in the electronic structure, often resulting in higher reactivity. In fact, AFM images revealed that the photoreduction of Ag^+ to Ag at the rutile occurred preferentially in the defect areas.[24] The higher reactivity may be the result of the unique electronic structure at the defect sites. These (atomic level) defects are sometimes referred to "special sites". Thus, there is a possibility that the greater APCE for the nanocrystalline system may be contributed by the nano-scaling of the TiO_2 crystallites, which increases the number of the special sites, where the electron transfer from the N3 is more efficient. Future investigation with *in situ* scanning probe microscopy is expected to reveal the relationship among the crystal surface morphology, the dye adsorption, and the electron injection efficiency (see Chapter 4, page 145).

Reproduced with permission of the copyright owner. Further reproduction prohibited without permission.

3.4. Conclusions

Natural anatase crystals were sensitized with the ruthenium-based dye (N3) and showed a maximum IPCE of 3.2×10^{-4}, about one third of the value for a synthetic anatase single crystal. The sensitization efficiency varied among the different crystals. A face dependence of sensitization efficiency was also observed. The morphological examination with atomic force microscopy indicated that these differences in sensitization by the crystals and the faces were not solely the result of surface area differences. The explanation for the face dependence of sensitization efficiency was attempted by using the surface structure of the (101) and (001) face of anatase and modeling the two site binding of the N3 molecules. The natural anatase exhibited very slow photocurrent transient of onset and decay on a millisecond time scale. The rise time became shorter with increasing light intensity and dye coverage. These observations suggest that the mechanism of trapping and detrapping of injected electrons at traps inside of the crystals plays a significant role in the electron transport in the natural anatase as well as in anatase nanocrystalline films. The comparison of sensitization behavior between the anatase single crystals (natural and synthetic) and anatase nanocrystalline films found that the calculated APCE for the nanocrystalline films was approximately 3 to 7 times greater than that for the single crystals. Although this counterintuitive result is presently unexplainable, future investigation with *in situ* scanning probe microscopy is expected to reveal the relationship among the crystal surface morphology, the dye adsorption, and the electron injection efficiency.

Reproduced with permission of the copyright owner. Further reproduction prohibited without permission.

References cited in Chapter 3

1. B. O'Regan and M. Grätzel, *Nature*, **353**, 737 (1991).

2. M. K. Nazeeruddin, A. Kay, I. Rodicio, R. Humphry-Baker, E. Müller, P. Liska, N. Vlachopoulos, and M. Grätzel, *J. Am. Chem. Soc.*, **115**, 6382 (1993).

3. O. Kohle, M. Grätzel, A. F. Meyer, and T. B. Meyer, *Adv. Mater.*, **9**, 904 (1997).

4. V. Shklover, M.-K. Nazeeruddin, S. M. Zakeeruddin, C. Barbé, A. Kay, T. Haibach, W. Steurer, R. Hermann, H.-U. Nissen, and M. Grätzel, *Chem. Mater.*, **9**, 430 (1997).

5. V. Shklover, T. Haibach, B. Bolliger, M. Hochstrasser, M. Erbudak, H.-U. Nissen, S. M. Zakeeruddin, M. K. Nazeeruddin, and M. Grätzel, *J. Solid State Chem.*, **132**, 60 (1997).

6. V. Shklover, Y. E. Ovchinnikov, L. S. Braginsky, S. M. Zakeeruddin, and M. Grätzel, *Chem. Mater.*, **10**, 2533 (1998).

7. A. Fillinger and B. A. Parkinson, *J. Electrochem. Soc.*, **146**, 4559 (1999).

8. T. Osa and M. Fujihira, *Nature*, **264**, 349 (1976).

9. M. Fujihira, N. Ohishi, and T. Osa, *Nature*, **268**, 226 (1977).

10. T. Watanabe, A. Fujushima, O. Tatsuoki, and K. Honda, *Bull. Chem. Soc. Jpn.*, **49**, 8 (1976).

11. W. D. K. Clark and N. Sutin, *J. Am. Chem. Soc.*, **99**, 4676 (1977).

12. M. T. Spitler and M. Calvin, *J. Chem. Phys.*, **66**, 4294 (1977).

13. P. D. Fleischauer and J. K. Allen, *J. Phys. Chem.*, **82**, 432 (1978).

14. R. Schmacher, R. H. Wilson, and L. A. Harris, *J. Electrochem. Soc.*, **127**, 96 (1980).

15. L. Kavan, M. Grätzel, S. E. Gilbert, C. Klemenz, and H. J. Scheel, *J. Am. Chem. Soc.*, **118**, 6716 (1996).

16. M. Nazeeruddin, *private communication* (1998).

17. G. Spoto, C. Morterra, L. Marchese, L. Orio, and A. Zecchina, *Vacuum*, **41**, 37 (1990).

Reproduced with permission of the copyright owner. Further reproduction prohibited without permission.

18. S. R. Morrison. *Electrochemistry at Semiconductor and Oxidized Metal Electrodes*, 166, Plenum Press, New York (1980).

19. H. Tang, K. Prasad, P. E. Sanjinés, P. E. Schmid, and F. Lévy, *J. Appl. Phys.*, **75**, 2042 (1994).

20. *Handbook of Chemistry and Physics*, 72nd ed., D. R. Lide, **4** 108, CRC Press, (1993).

21. M. A. Ryan, E. C. Fitzgerald, and M. T. Spitler, *J. Phys. Chem.*, **93**, 6150 (1989).

22. R. Hengerer, L. Kavan, P. Krtil, and M. Grätzel, *J. Electrochem. Soc.*, **147**, 1467 (2000).

23. A. Vittadini, A. Sellone, F. P. Rotzinger, and M. Grätzel, *Phys. Rev. Let.*, **81**, 2954 (1998).

24. P. A. M. Hotsenpiller, J. D. Bolt, W. E. Farneth, J. B. Lowekamp, and G. S. Rohrer, *J. Phys. Chem. B*, **102**, 3216 (1998).

25. V. S. Lusvardi, M. A. Barteau, and W. E. Farneth, *J. Catl.*, **153**, 41 (1995).

26. K. S. Kim and M. A. Barteau, *J. Catl.*, **125**, 353 (1990).

27. N. Daude, C. Gout, and C. Jouanin, *Phys. Rev. B*, **15**, 3229 (1977).

28. J. B. Goodenough, A. Hamnett, G. Huber, F. Hulliger, M. Leib, S. K. Ramasesha, and H. Werheit, in Landolt-Bornstein, Numerical Data and Functional Relationships in Science and Technology, K.-H. Hellwege and O. Madelung, ed., Chapter 9.15.2.1, Springer-Verlag, New York (1984).

29. K. Murakoshi, G. Kano, Y. Wada, S. Yanagida, H. Miyazaki, M. Matsumoto, and S. Murasawa, *J. Electroanal. Chem.*, **396**, 27 (1995).

30. K. S. Finnie, J. R. Bartlett, and J. L. Woolfrey, *Langmuir*, **14**, 2744 (1998).

31. D. Halliday and R. Resnick, *Fundamentals of Physics*, 3rd, 674, Wiley, New York (1988).

32. L. M. Peter and D. Vanmaekelberg, *Adv. Electrochem. Sci. Eng.*, **6**, 77 (1999).

33. S. Hotchandani and P. V. Kamat, *J. Electrochem. Soc.*, **139**, 1630 (1992).

34. P. Hoyer and H. Weller, *J. Phys. Chem.*, **99**, 14096 (1995).

35. F. Cao, G. Oskam, J. G. Meyer, and P. Searson, *J. Phys. Chem.*, **100**, 17021 (1996).

36. A. Solbrand, A. Henningsson, S. Södergren, H. Kindström, A. Hagfeldt, and S.-E. Kindquist, *J. Phys. Chem. B*, **103**, 1078 (1999).

Reproduced with permission of the copyright owner. Further reproduction prohibited without permission.

37. A. Hagfeldt and M. Grätzel, *Chem. Rev.*, **95**, 49 (1995).

38. P. E. de Jongh and D. Vanmaekelbergh, *Phys. Rev. Lett.*, **77**, 3427 (1996).

39. P. E. de Jongh and D. Vanmaekelbergh, *J. Phys. Chem. B*, **101**, 2716 (1997).

40. K. Schwarzburg and F. Willig, *Appl. Phys. Lett.*, **58**, 2520 (1991).

41. M. P. Dare-Edwards, J. B. Goodenough, A. Hamnett, K. R. Seddon, and R. D. Wright, *Trans. Faraday Soc.*, **70**, 285 (1980).

42. *Semiconductor Electrodes*, ed., H. O. Finklea, 180, Elsevier, Amsterdam (1988).

43. L. Sharp, D. Louder, and B. A. Parkinson, *Proceedings of the 19th DOE Solution Photochemistry Research Conference, 1995*, (1995).

44. R. Eichberger and F. Willig, *Chem. Phys.*, **141**, 159 (1990).

Reproduced with permission of the copyright owner. Further reproduction prohibited without permission.

CHAPTER FOUR

Imaging Crystal Surfaces

In the previous two chapters, my experimental data and discussions about how dye coverage affects the dye sensitization efficiencies in anatase (a mixture with rutile) nanocrystalline films and natural anatase crystals were presented. As described at the end of Chapter 3, the final goal of this project is to reveal the relationship between the morphology of semiconductor surface, the dye adsorption behavior, and the dye sensitization efficiency with *in situ* scanning probe microscopy. This approach allows us to connect the results obtained with conventional photoelectrochemical techniques to nanoscopic observations of the dye/semiconductor interface. Atomic force microscopy (AFM) can be performed *in situ* where a sample is contained in a cell and immersed in an appropriate liquid. With this method, the dye/anatase interface can be investigated in an electrolyte that is the actual operation condition of the dye-sensitized solar cell.

The aspects of the dye adsorption to the crystal surfaces that we are interested in are: 1) How do the dye molecules adsorb to the crystal surfaces, by forming islands or isolated monomers? If the dye molecules form islands, how does a dye coverage affect islanding? How does islanding affect the

Reproduced with permission of the copyright owner. Further reproduction prohibited without permission.

photon to current conversion efficiencies? 2) How do the dye molecules bind to the crystal surface at step and kink sites? Do the dye molecules adsorb preferentially to these sites? Do the dye molecules adsorbed to the steps or kinks sensitize differently than dyes adsorbed to flat terraces? 3) How much surface mobility do the adsorbed dyes have on the crystal surfaces? How is the surface mobility of the adsorbed dye influenced by the morphologies of the crystal surfaces?

As the first step to the *in situ* investigation, I have attempted to obtain adequately flat surfaces on the natural anatase crystals in order to image the adsorption behavior of the dye. Because the dye molecules, whose molecular height is approximately 10 Å, need to be distinguished from the crystal surface, an ideal crystal surface is a terraced surface with rather wide (> 100 Å) terraces.

In addition to the natural anatase crystals, synthetic rutile crystals were also utilized for surface imaging with AFM. High purity synthetic rutile crystals are more readily available with large surfaces and should have less roughness than natural crystals. Also, we are interested in comparing the dye adsorption behavior between anatase and rutile surfaces. A synthetic highly oriented anatase thin film was also provided by Dr. Gao at Pacific Northwest National Laboratory. Unfortunately, an atomically flat terraced surface was only found in one experiment on perhaps a special area of a crystal.

In this final chapter, I report my efforts to prepare an atomically flat, terraced surface by presenting the AFM images taken in air and *in situ* of the crystal surfaces before and after various treatments.

Reproduced with permission of the copyright owner. Further reproduction prohibited without permission.

4.1. Sample Crystals

Natural anatase crystals from the same sources as those used for the dye sensitization experiments as well as from an additional source were utilized for dye-semiconductor interface imaging with AFM. These natural crystals are from Tyssedal, Norway, from Uruacu Goias, Brazil, and from Ural Puyva, Russia. Representative crystals are shown in Figure 3.1. and Figure 4.1. The Norwegian anatase crystals were an acute bipyramidal configuration and had a black luster (Figure 3.1.a.). All of the Norwegian anatase crystals exhibited clearly defined (101) faces as shown in Figure 3.1.a. The Brazilian anatase crystals were a tabular habit and were translucent reddish brown (Figure 3.1.b.). All of the Brazilian crystals exhibited one or two (001) faces and several (101) faces as shown in Figure 3.1.b. The Russian anatase crystals had the same crystal habit as the Norwegian anatase crystals, acute bipyramids with a black luster (Figure 4.1.). The similar crystal habit of the Russian and Norwegian crystals allows us to assign their major faces to be (101).

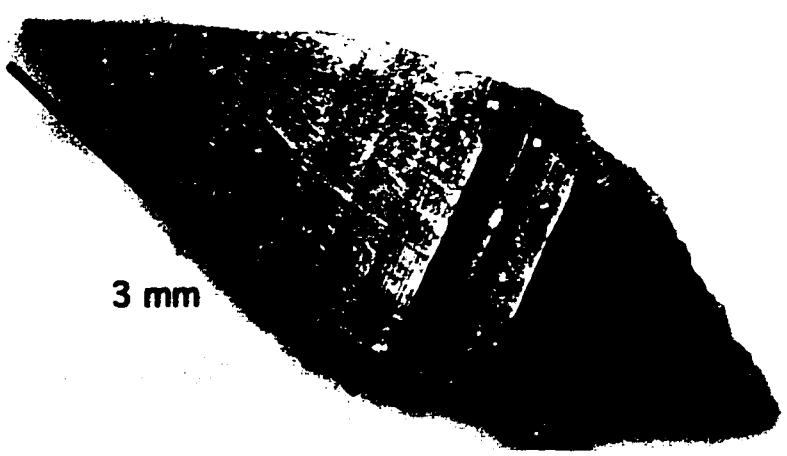

Figure 4.1. Russian anatase crystal.

Reproduced with permission of the copyright owner. Further reproduction prohibited without permission.

In addition to the natural anatase crystals, synthetic rutile crystals with (100) and (001) surfaces were purchased (MTI Corporation) and investigated. Both rutile crystals are transparent with dimensions of 1 cm x 1 cm x 1 mm. As mentioned previously, a comparison of dye adsorption behavior between anatase and rutile surfaces was one of the purposes for using the synthetic rutile crystals. The crystal structure model of rutile is illustrated in Figure 4.2.a (See Figure 3.7 for anatase). As analyzed in Chapter 3, the distances between oxygen atoms that can be involved in binding of the N3 dye are 6.2 Å, 10.0 Å, and 9.8 Å (Figure 3.7.c).[1] Therefore, the distances between Ti sites suitable for the N3 binding are 5.9 Å, 9.6 Å, and possibly 9.2 Å on the (100) surface, and 6.5 Å and possibly 9.2 Å on the (001) surface (Figure 4.2.b). So, it appears that N3 can bind to the rutile surfaces, yet perhaps with different geometries.

A synthetic anatase thin film with predominately (001) orientation was grown by metal-organic chemical vapor deposition on a $SrTiO_3$ (001) substrate.[2] Anatase thin films grown in this method are epitaxial with the $SrTiO_3$ substrate and have a lattice constant approximately equal to that of bulk anatase.[3, 4]

4.2. Atomic force microscopy

The atomic force microscope (AFM) was a Digital Instruments/Veeco with a Nanoscope® IIIA controller and a multimode base. Scanning in the air was done with tapping mode with a J or E scanner. The tips were Ultralever® (Park Scientific Instruments) silicon tips with force constants of approximately 1.9 N/m.

Reproduced with permission of the copyright owner. Further reproduction prohibited without permission.

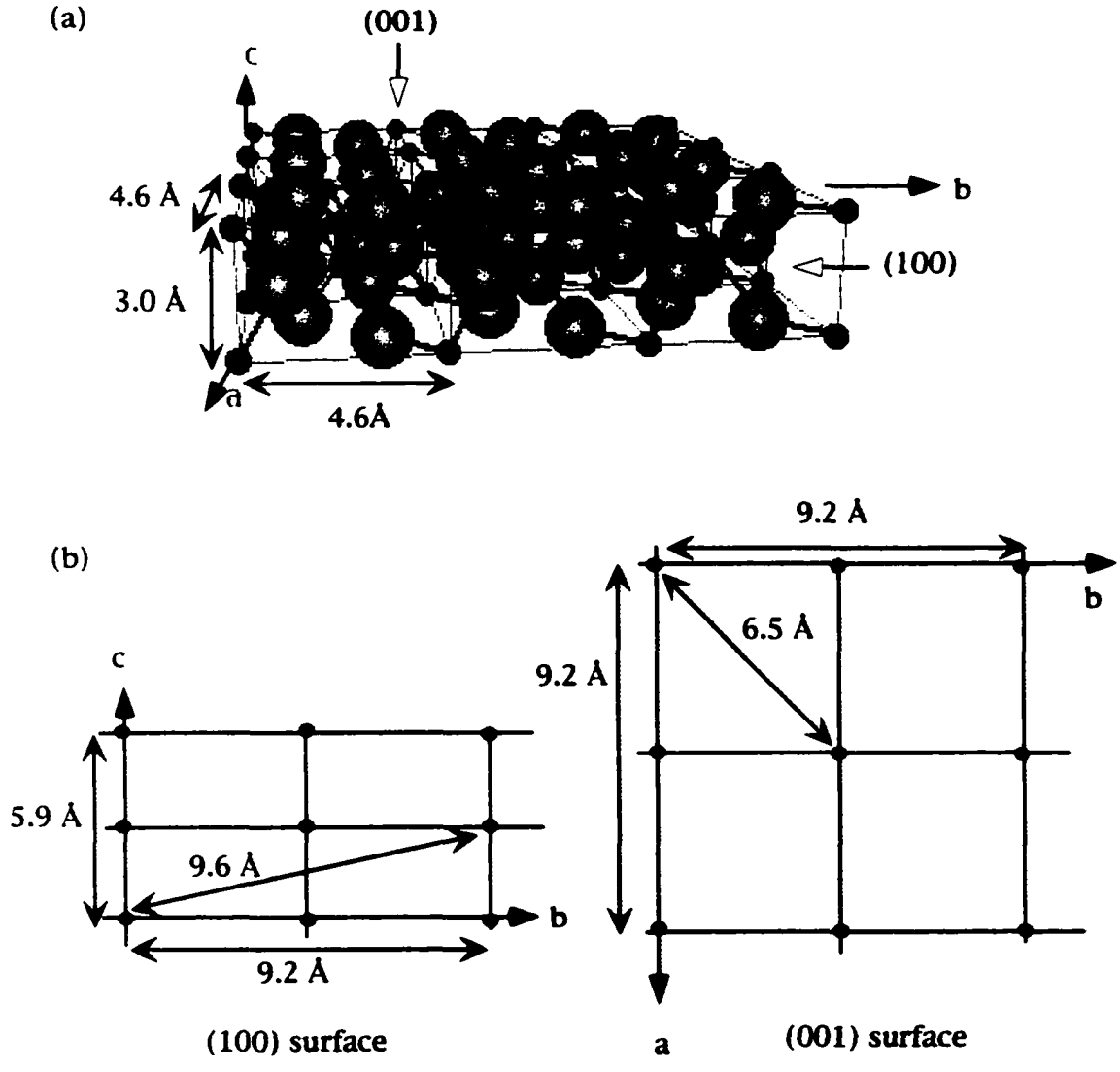

Figure 4.2. Crystal structure model of rutile and the distances between Ti sites on the (100) and (001) surfaces. (a) Crystal structure model of rutile. Large gray spheres are oxygen, and small black spheres are titanium. (b) The distance between Ti sites, that are suitable for the binding of the dye molecules with two carboxyl groups, on the (100) and (001) surfaces. Small black dots are Ti sites.

Reproduced with permission of the copyright owner. Further reproduction prohibited without permission.

The AFM was also operated in ethanol to image the adsorbed dye on the crystal surface *in situ*. Ethanol was chosen for the fluid because the dye dissolves in ethanol, and this solution is used for treating the anatase and rutile samples to adsorb the dye. Fluid imaging requires a special tip holder to contain the fluid. The fluid tip holder consists of a small glass assembly with a wire clip to hold an AFM cantilever substrate. The glass surface provides a flat, beveled interface so that the AFM laser beam may enter the fluid without being distorted by an unstable fluid surface.[5] A schematic of the fluid tip holder is shown in Figure 4.3. Scanning in a fluid was done using tapping mode with a J or E scanner. The tips were Ultralever® (Park Scientific Instruments) silicon nitride tips with force constants of approximately 1.0 N/m.

One of the difficulties encountered during the imaging in ethanol was that air bubbles are trapped near the cantilever and interfere with the laser beam's optical path. The bubbles make it difficult to get a good laser reflection from the cantilever after filling the tip holder with ethanol. Although the bubbles could be broken loose from the tip by forcing ethanol quickly through the liquid cell, this disturbed the thermal equilibration of the cell, and the drift of the image became severe. The effect of thermal drift is especially disruptive at small scan sizes (i.e. $< 1\mu m$). Since it is necessary to image the adsorption of dye at the small scan sizes, solving this "air bubble problem" is an urgent objective for the success of this project, especially for real time observation of dye adsorption.

Reproduced with permission of the copyright owner. Further reproduction prohibited without permission.

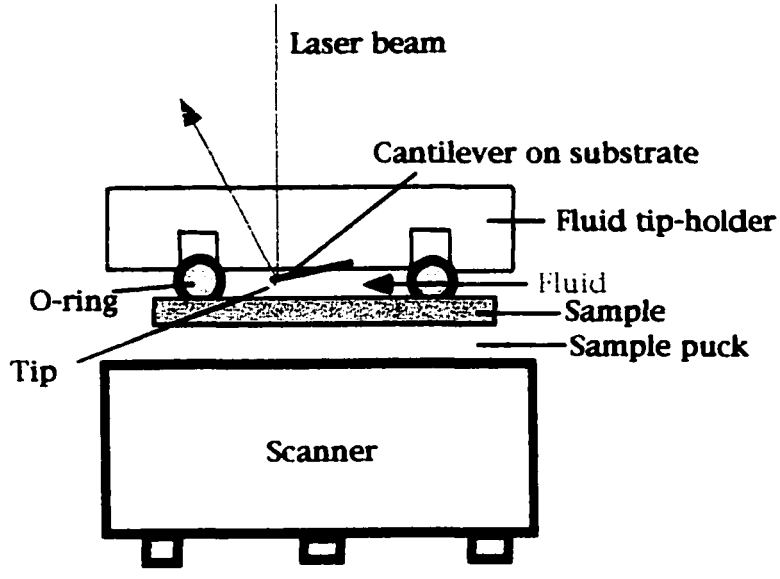

Figure 4.3. Schematic of a setup for AFM imaging in a fluid.

Reproduced with permission of the copyright owner. Further reproduction prohibited without permission.

4.3. Surface treatments and morphologies of crystal surfaces

Morphologies of the crystal surfaces were investigated before and after surface treatments with optical microscopy, scanning electron microscopy, and atomic force microscopy. The surface treatments applied to the crystal surfaces are: 1) physical polishing with colloidal silica, 2) chemical etching with 5 M NaOH at room temperature, hot 5M NaOH, and 18 M H_2SO_4 at room temperature, 3) high temperature annealing with a flow of oxygen.

i) Brazilian anatase crystals

Optical micrographs of the surface of a Brazilian anatase crystal are shown in Figure 4.4. The (101) surface of the Brazilian crystal indicates a stepped structure (Figure 4.4.a). The (001) surface of the Brazilian crystal appears flat without topographical features (Figure 4.4.b). Impurities in void and occlusions are clearly seen on both surfaces.

Scanning electron micrographs (SEM) of the Brazilian crystal before surface treatment were shown in Figure 3.4. In order to obtain SEM images at magnifications higher than x 2500, good electrical contact between the crystal and a sample holder was critical, since charging of the sample surface with the electron beam significantly reduced the resolution. A good electrical contact was formed with silver epoxy (Tricone). The (101) surface of the Brazilian crystal shows an angular scale-like structure (Figure 3.4.d). On the (001) surface of the Brazilian crystal, rectangular pits are seen at a low magnification (Figure 3.4.e), and tabular protrusions are visible at higher magnifications (Figure 3.4.f).

Reproduced with permission of the copyright owner. Further reproduction prohibited without permission.

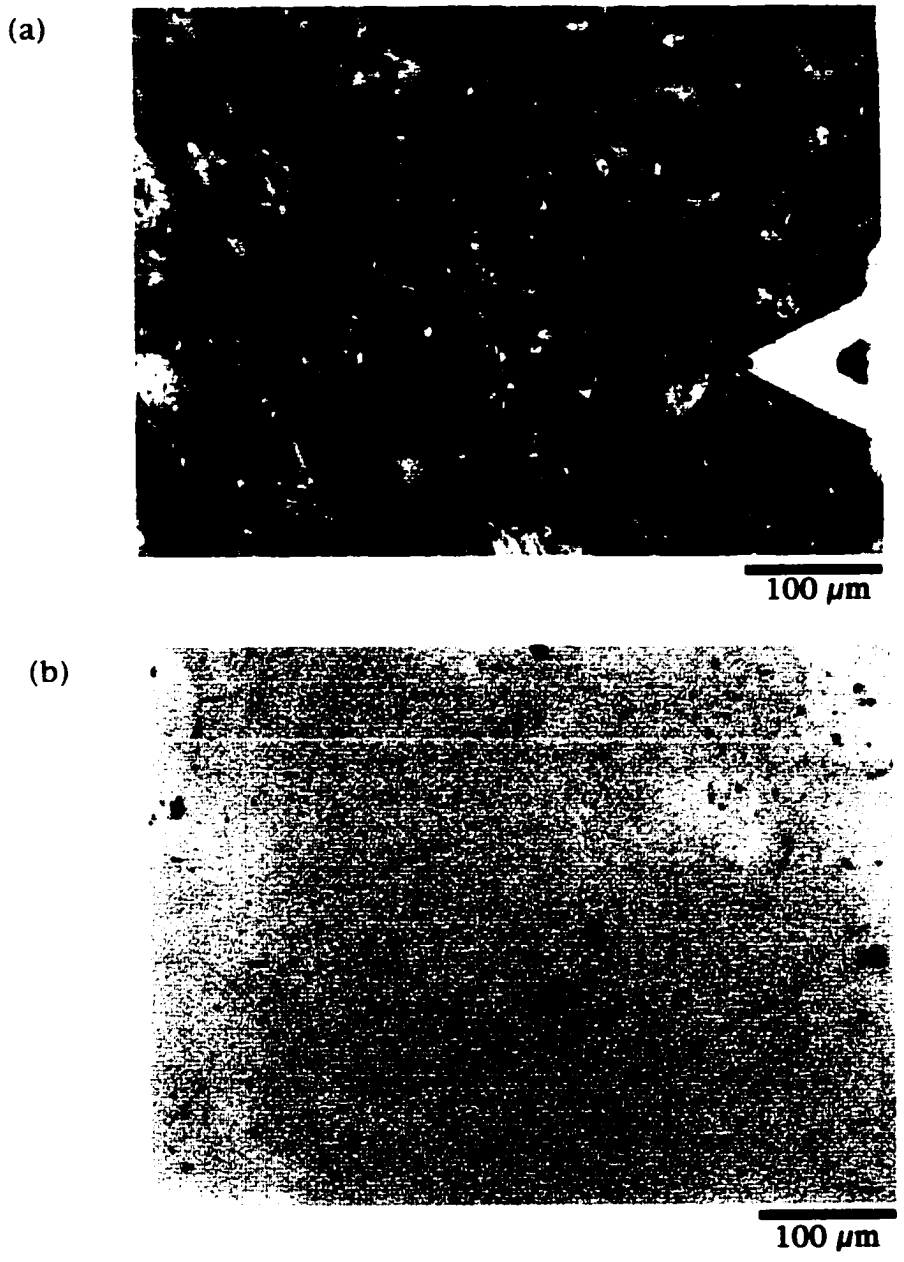

Figure 4.4. Optical micrographs of the surfaces of a Brazilian anatase crystal. (a) The (101) surface. A cantilever is seen at the right edge. (b) The (001) surface.

Reproduced with permission of the copyright owner. Further reproduction prohibited without permission.

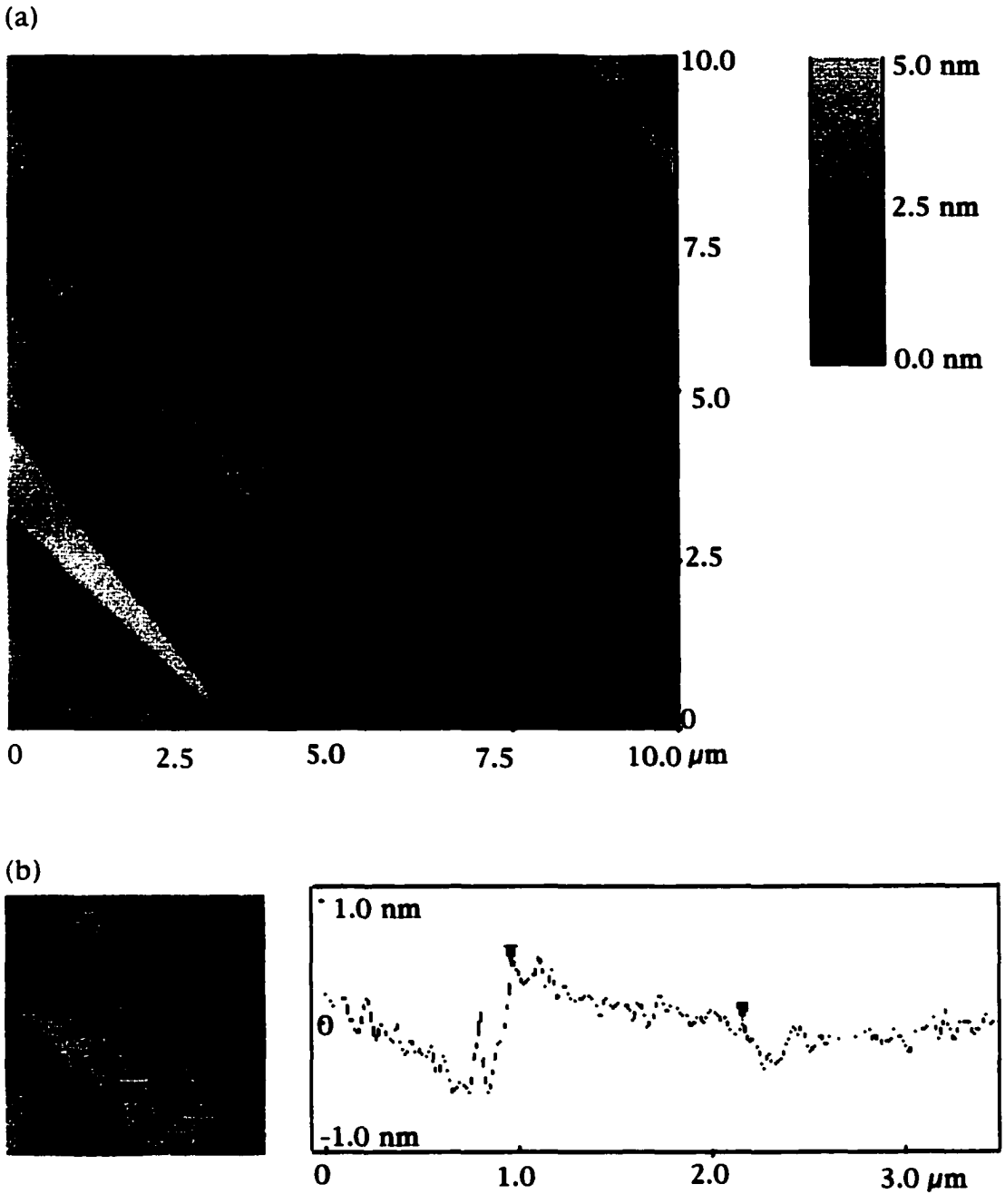

Figure 4.5 (a) Atomic force micrograph of the (001) surface of the Brazil anatase crystal before treatments. (b) Section analysis of the atomic force micrograph.

Reproduced with permission of the copyright owner. Further reproduction prohibited without permission.

A flat terraced surface was found with atomic force microscopy on an untreated (001) face of the Brazilian crystal, and is shown in Figure 4.5.a. Large terraces appear as sharp lines in the image. The section analysis of the atomic force micrograph (Figure 4.5.b) reveals that the height difference between the highest and lowest points on the line is approximately 5 Å, corresponding to one or two layers of the anatase unit cell. This flat terraced surface was found by chance, however, it or similar regions have not been located again.

To reproducibly obtain a flat terraced surface is crucial for investigation of dye adsorption on the crystal surface. Therefore, the natural crystals were polished to reduce the overall surface roughness prior to chemical etching. In order to polish the crystals, the crystals were potted in epoxy, so the crystal surface was parallel to the epoxy surface (Figure 4.6). Extra epoxy above the crystal surface was cut off, and the crystal surface was polished with successively smaller grits with the final polish using colloidal silica. Potting the crystals also facilitates the imaging of the crystal surfaces, particularly those with the shapes and sizes difficult to accommodate in the fluid tip-holder and o-ring.

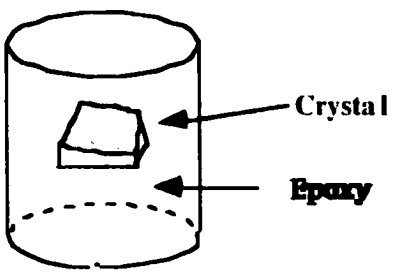

Figure 4.6. Natural crystal potted in epoxy

Reproduced with permission of the copyright owner. Further reproduction prohibited without permission.

AFM images of the Brazilian crystal after polishing are shown in Figure 4.7. At a large scan size (Figure 4.7.a), a wavy feature is seen, maybe indicating terraces. The wavy feature wasn't an artifact since the wavy lines turned 90° when the scan angle was changed by 90° (Figure 4.7.a to b). However, the image at a smaller scan size (Figure 4.7.c) reveals that the terraces are not clear cut and further surface treatments are necessary for obtaining flat surfaces.

The Brazilian anatase crystal was treated with hot 5 M NaOH for 3 hours. The AFM images of the chemically treated Brazilian crystal are shown in Figure 4.8. The image at a small scan size (Figure 4.8.c) indicates that the chemical etching may have sharpened the terrace edges by dissolving surface contaminants. The same sample was also investigated in ethanol with atomic force microscopy and shown in Figure 4.9. Imaging in a fluid with AFM potentially yields better resolution. This is because the condensed water layer, which is formed on a sample surface by the adsorption of water vapor from the atmosphere, has less effect in a fluid than in the air. This advantage of imaging in a fluid may be seen in Figure 4.9.b, showing a clearer image than obtained in the air (Figure 4.8.b). However, drift of scan spots during thermal equilibration of the liquid severely distorted the image taken at a smaller scan size (500 nm) (Figure 4.9.c).

Reproduced with permission of the copyright owner. Further reproduction prohibited without permission.

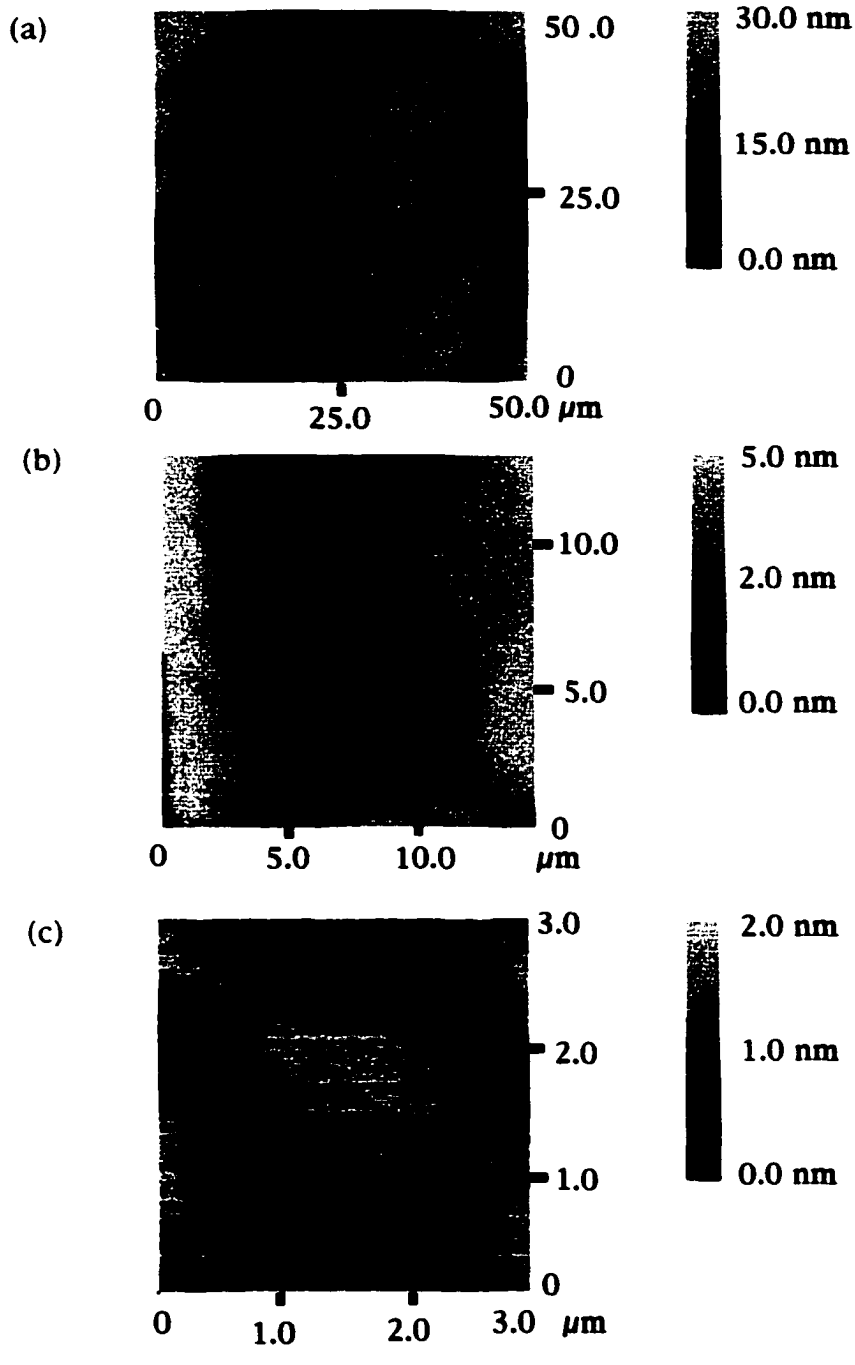

Figure 4.7. AFM images of the Brazilian anatase crystal after polishing. Scan rate: 0.5 Hz for (a), and 1.0 Hz for (b) and (c); set point: 0.92 V; drive amplitude: 900 mV; drive frequency: 234 kHz; number of samples per scan: 512; scan angle: O° for (a), 90° for (b) and (c).

Reproduced with permission of the copyright owner. Further reproduction prohibited without permission.

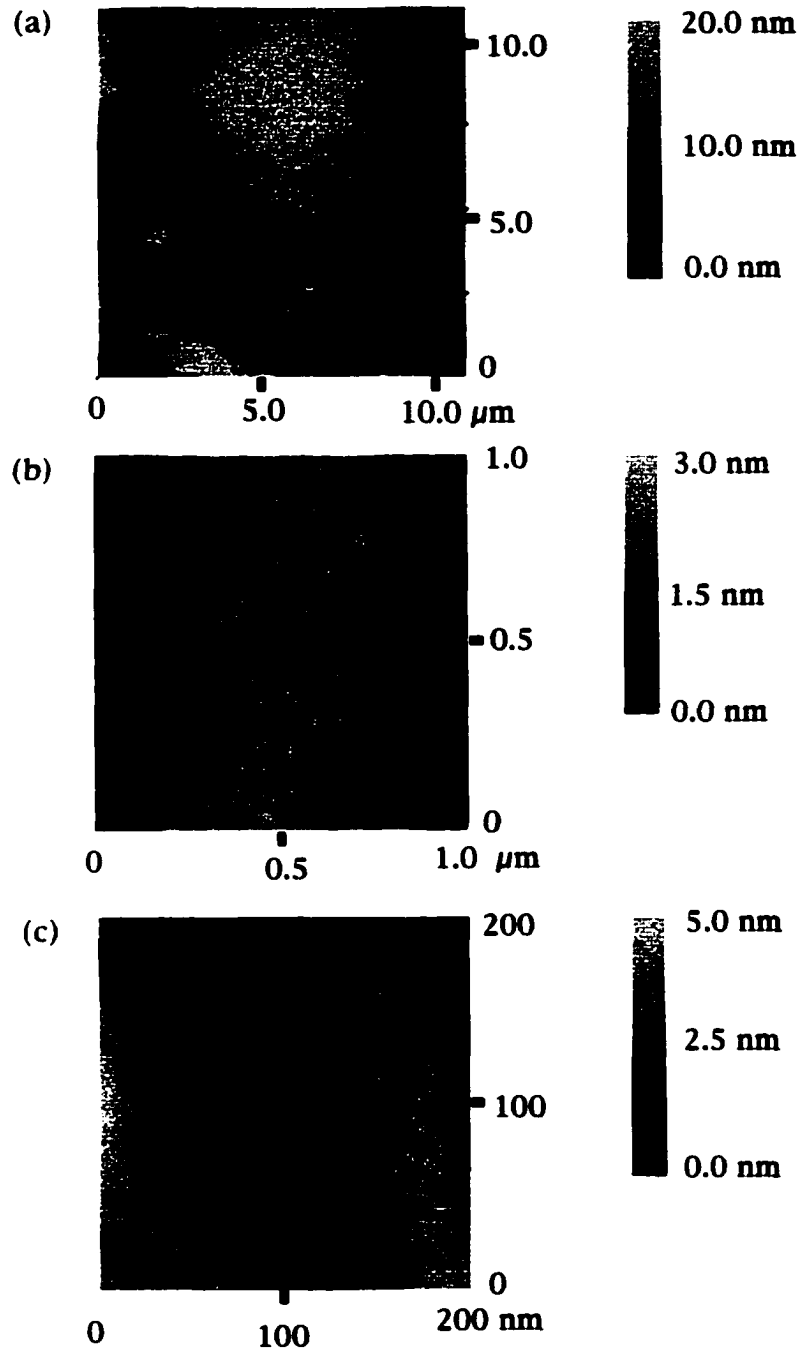

Figure 4.8. AFM images of the Brazilian anatase crystal after polishing and etching with hot 5 M NaOH for 3 hours. Scan rate: (a) and (b) 1.0 Hz, and (c) 0.5 Hz; set point:1.2 V for (a) and (b), and 1.4 V for (c); drive amplitude 500 mV; drive frequency 373 kHz; number of samples per scan: 512.

Reproduced with permission of the copyright owner. Further reproduction prohibited without permission.

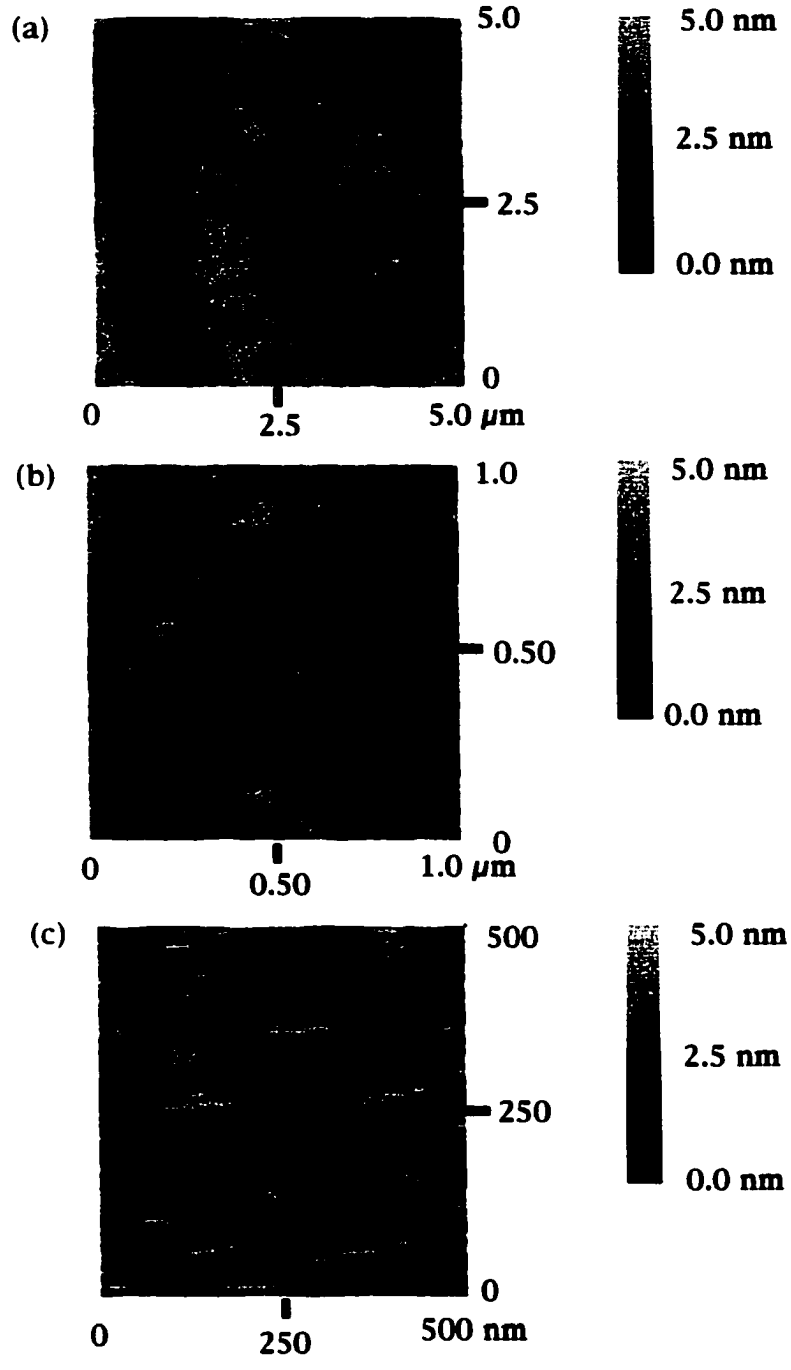

Figure 4.9. AFM images of the Brazil anatase crystal in ethanol. The crystal was polished and etched with hot 5 M NaOH for 3 hours. Scan rate: 1.0 Hz; set point: 1.2 V for (a) and (b), and 1.1 V for (c); drive amplitude: 500 mV; drive frequency: 7.34 kHz; number of samples per scan: 512.

Reproduced with permission of the copyright owner. Further reproduction prohibited without permission.

ii) Norwegian and Russian anatase crystals

An optical micrograph of a Norwegian anatase crystal clearly exhibits a stepped structure (Figure 4.10.a), which is explained with a crystal structure model of the (101) surface shown in Figure 4.10.b. The staircase structure is also clearly seen in scanning electron micrographs of the surface of the Norwegian crystal (Figure 3.4.a & b). AFM images of a Russian anatase crystal, which exhibited the same acute bipyramidal habit, are shown before treatments (Figure 4.11) and after polishing with colloidal silica (Figure 4.12). Because of the shape of the Norwegian and Russian crystals, mounting the crystals flat against the scanner is very difficult. Potting these crystals in epoxy (Figure 4.6) and polishing with colloidal silica solved this problem and greatly reduced the variation of surface height from 30 nm (Figure 4.11.b) to 3.0 nm (Figure 4.12.b) at 1.3 μm scan size. No changes in surface morphology of the Norwegian and Russian crystals were detected with AFM after the treatment with hot 5 M NaOH for 3 hours.

Reproduced with permission of the copyright owner. Further reproduction prohibited without permission.

(a)

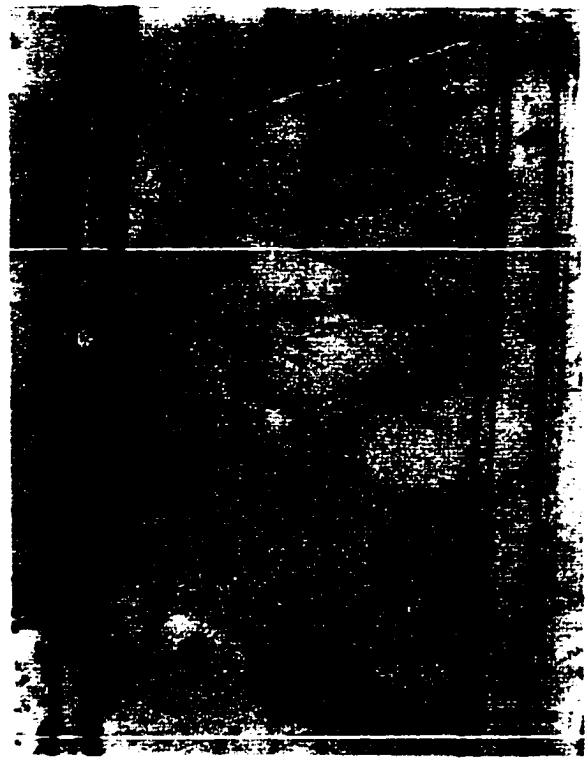

(b)

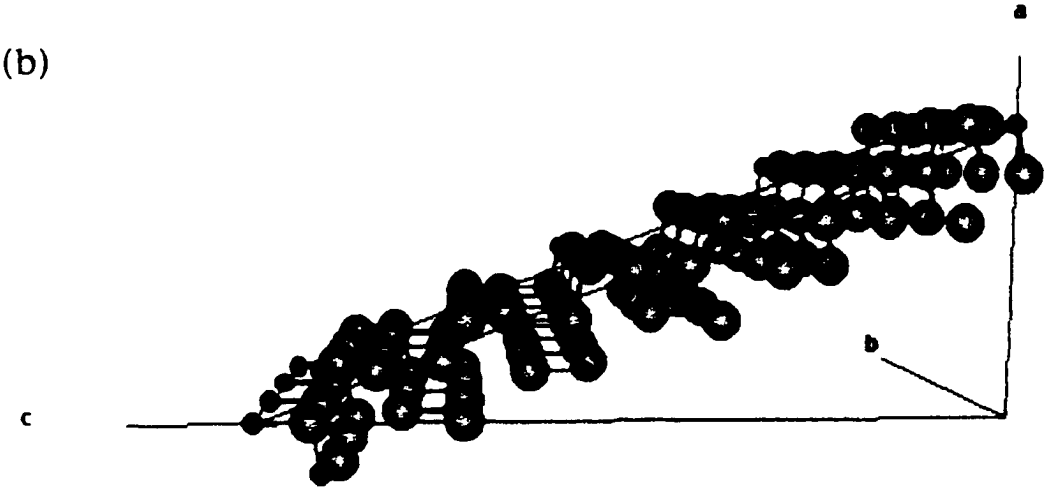

Figure 4.10. (a) Optical micrograph of a surface of a Norwegian anatase crystal. (b) A side view of the (101) surface of anatase crystal created by using Crystal Designer software. Small black spheres are titanium, and large gray spheres are oxygen.

Reproduced with permission of the copyright owner. Further reproduction prohibited without permission.

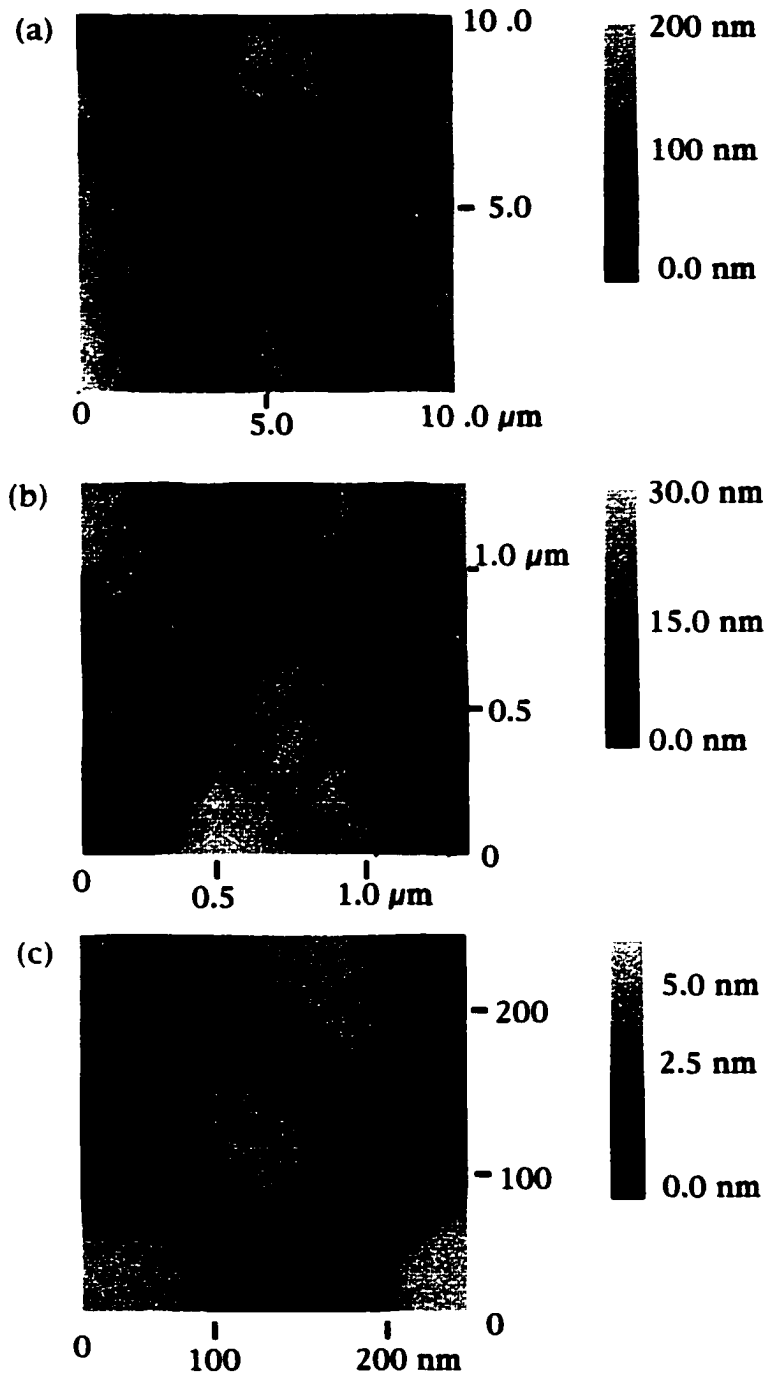

Figure 4.11. AFM images of the Russian anatase crystal without surface treatments. Scan rate: 3.0 Hz; set point: 0.32 V; drive amplitude: 477 mV, drive frequency 363 kHz; number of samples per scan: 512.

Reproduced with permission of the copyright owner. Further reproduction prohibited without permission.

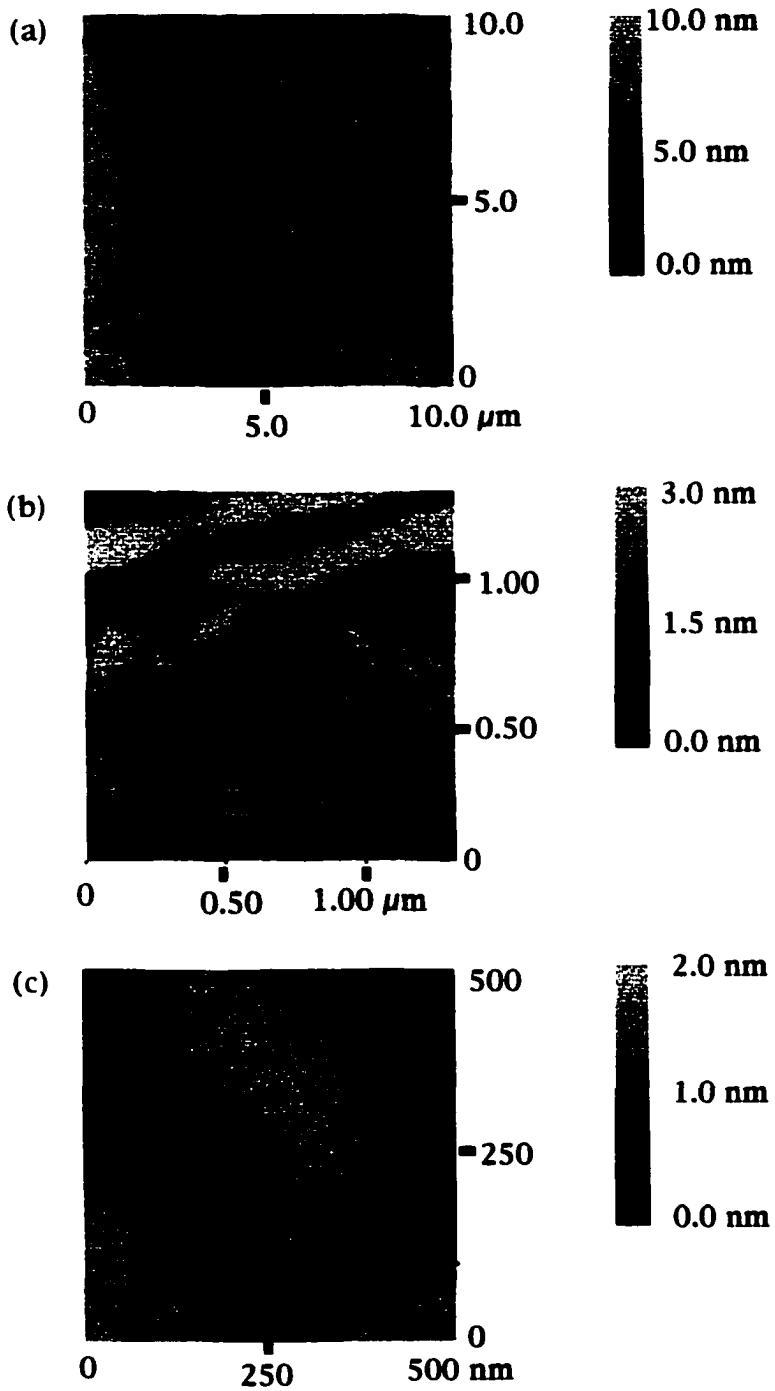

Figure 4.12. AFM images of the Russian anatase crystal after polishing. Scan rate: 1.0 Hz; set point: 0.39 V for (a) and (c), and 0.31 V for (b); drive amplitude: 550 mV; drive frequency:426 kHz; number of samples per scan: 512.

Reproduced with permission of the copyright owner. Further reproduction prohibited without permission.

iii) Synthetic anatase thin film

An AFM image of a synthetic anatase thin film of the (001) surface shows islands growth in a specific direction (Figure 4.13.b). At a smaller scan size, height variation is approximately 1 nm, which is about 1 unit cell in the c-direction (Figure 4.13.c). The anatase thin film was annealed at 800 °C under an oxygen flow in order to promote the formation of terraces. According to a private communication, this anatase thin film will not undergo phase transition to rutile even when annealed at 800 °C because the $SrTiO_3$ substrate is templating the anatase lattice.[6] The effect of the annealing on surface morphology was not detected with AFM.

iv) Synthetic rutile single crystals of the (100) and (001) surfaces

Synthetic rutile single crystals were investigated with AFM as received and after a treatment with hot 5 M NaOH for 1.5 hours. The rutile crystal of the (001) surface shows a directional islands growth (Figure 4.14), that was also observed on the (001) surface of the synthetic anatase film (Figure 4.13.b). The surface of the rutile crystal is fairly smooth with 1.0 nm variation in height at a scan size of 1 μm x 1 μm except the high islands growth. AFM images of the (001) surface taken in ethanol after the chemical treatment show pits on the surface (Figure 4.15.a & b). These pits may have been created by the chemical etching or became visible due to the better resolution of imaging in the fluid. A synthetic rutile single crystal of the (100) surface does not have any high islands growth (Figure 4.16), and the surface is fairly smooth with a variation in height of 1 nm. The parallel lines seen at a larger scan size (Figure 4.16.a) are polishing marks. The (100) surface was treated with hot 5 M NaOH for 1.5 hours, yet no improvement of

Reproduced with permission of the copyright owner. Further reproduction prohibited without permission.

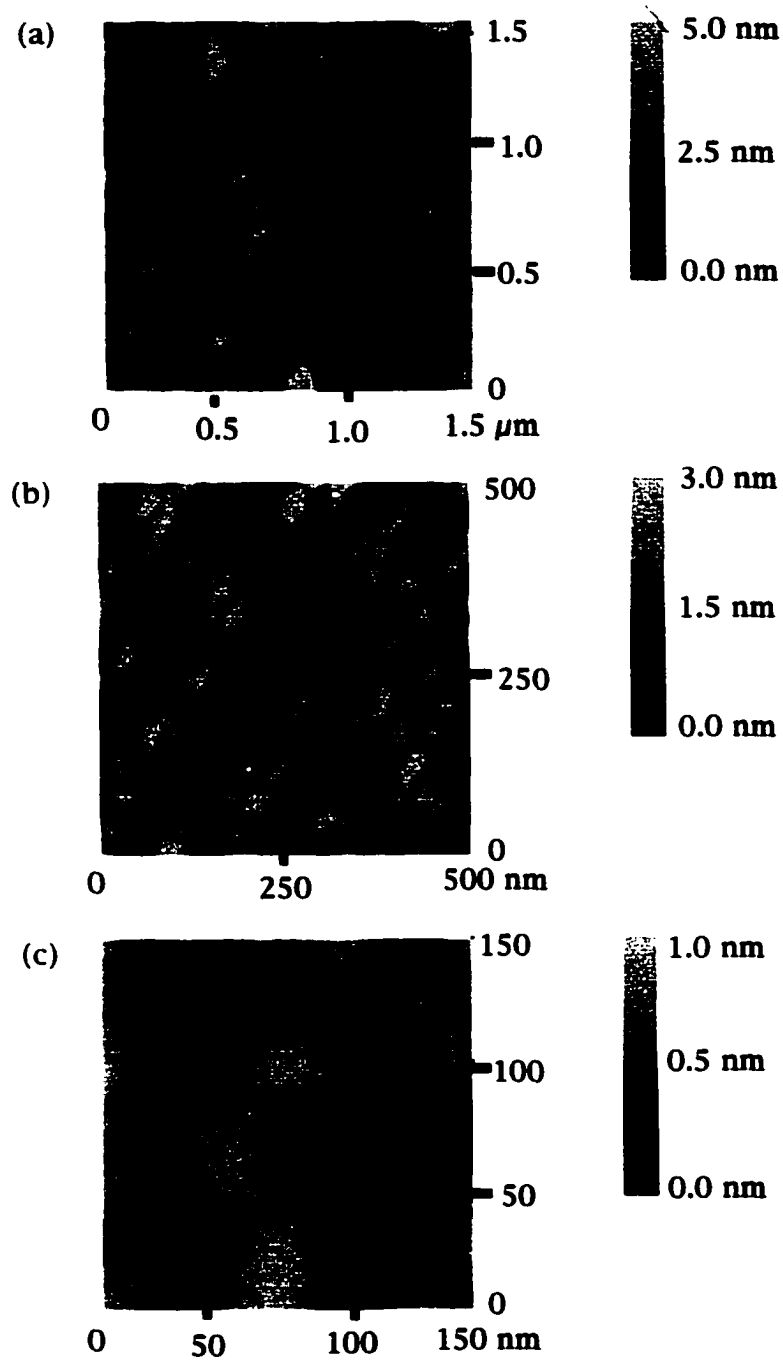

Figure 4.13. AFM images of synthetic anatase film of the (001) surface as received. Scan rate: 1.0 Hz; set point: 0.86 V for (a), 0.75 V for (b), and 0.84 V for (c); number of samples per scan: 512.

Reproduced with permission of the copyright owner. Further reproduction prohibited without permission.

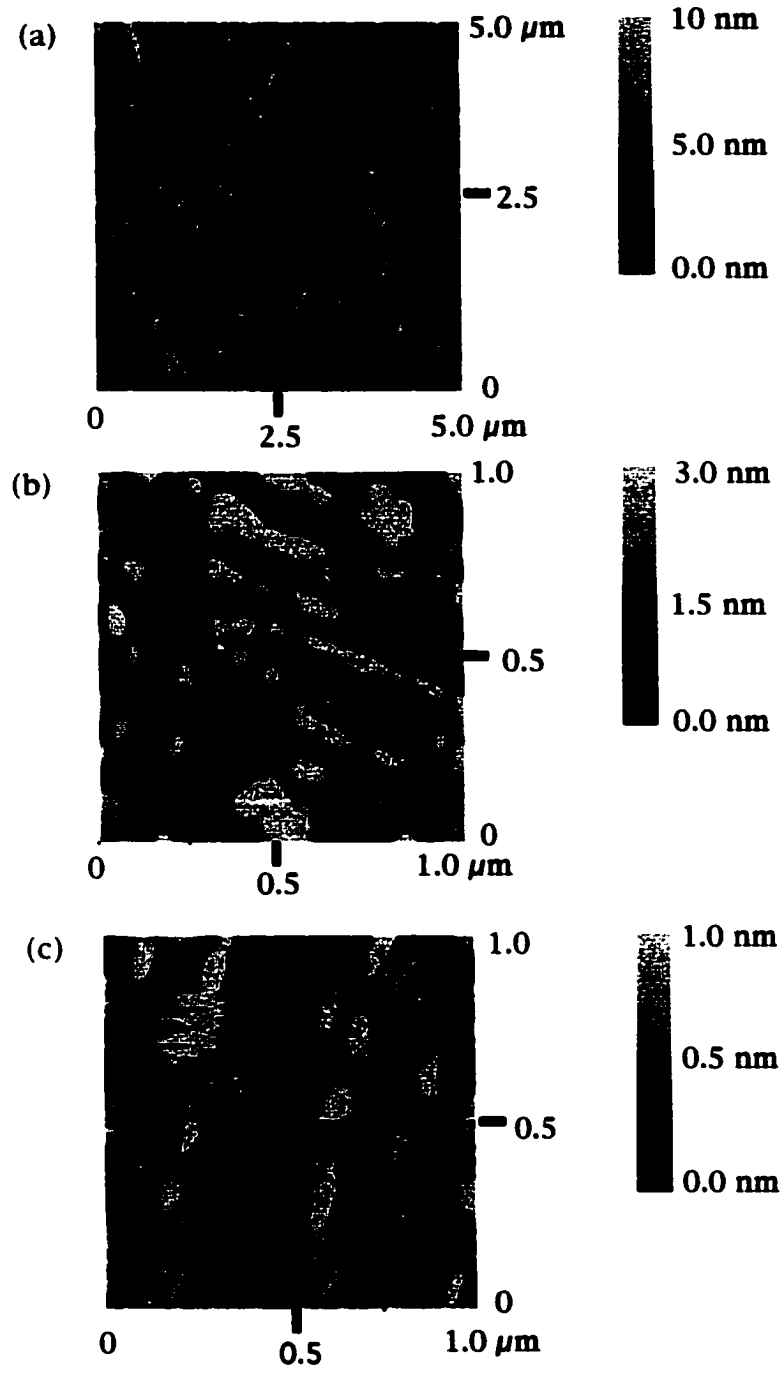

Figure 4.14. AFM imges of synthetic rutile with the (001) face as received. Scan rate: 1.0 Hz; set point: 1.2 V; drive amplitude: 600 mV; drive frequency: 282 kHz; number of samples per scan: 512.

Reproduced with permission of the copyright owner. Further reproduction prohibited without permission.

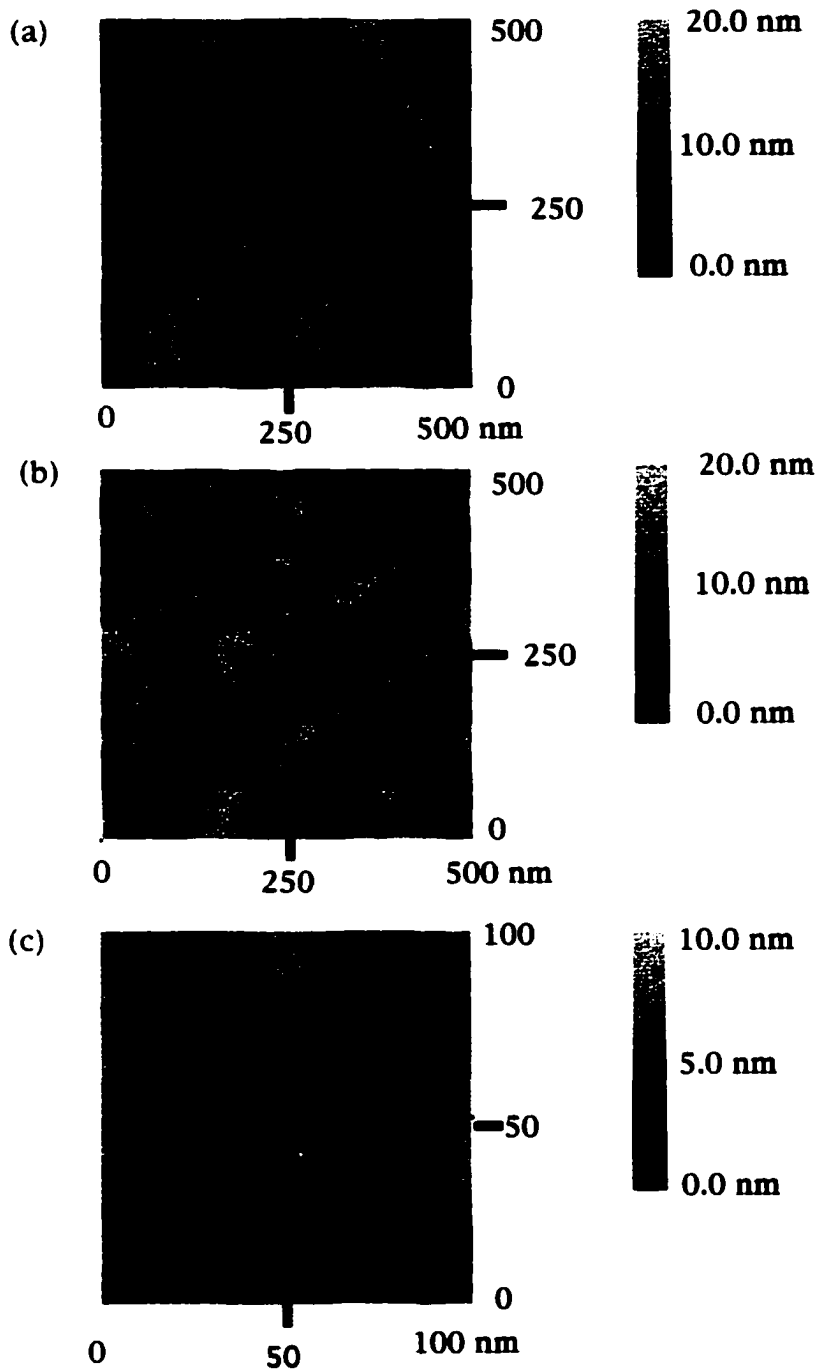

Figure 4.15. AFM images of synthetic rutile with (001) face in ethanol. The crystal was etched with hot 5M NaOH for 1.5 hours. Scan rate: 1.0 Hz; set point: 0.76 V for (a), and 0.59 V for (b) and (c); drive amplitude: 1.0 V for (a), and 1.2 V for (b) and (c); drive frequency: 9.1 kHz for (a), and 8.9 kHz for (b) and (c); number of samples per scan: 512.

Reproduced with permission of the copyright owner. Further reproduction prohibited without permission.

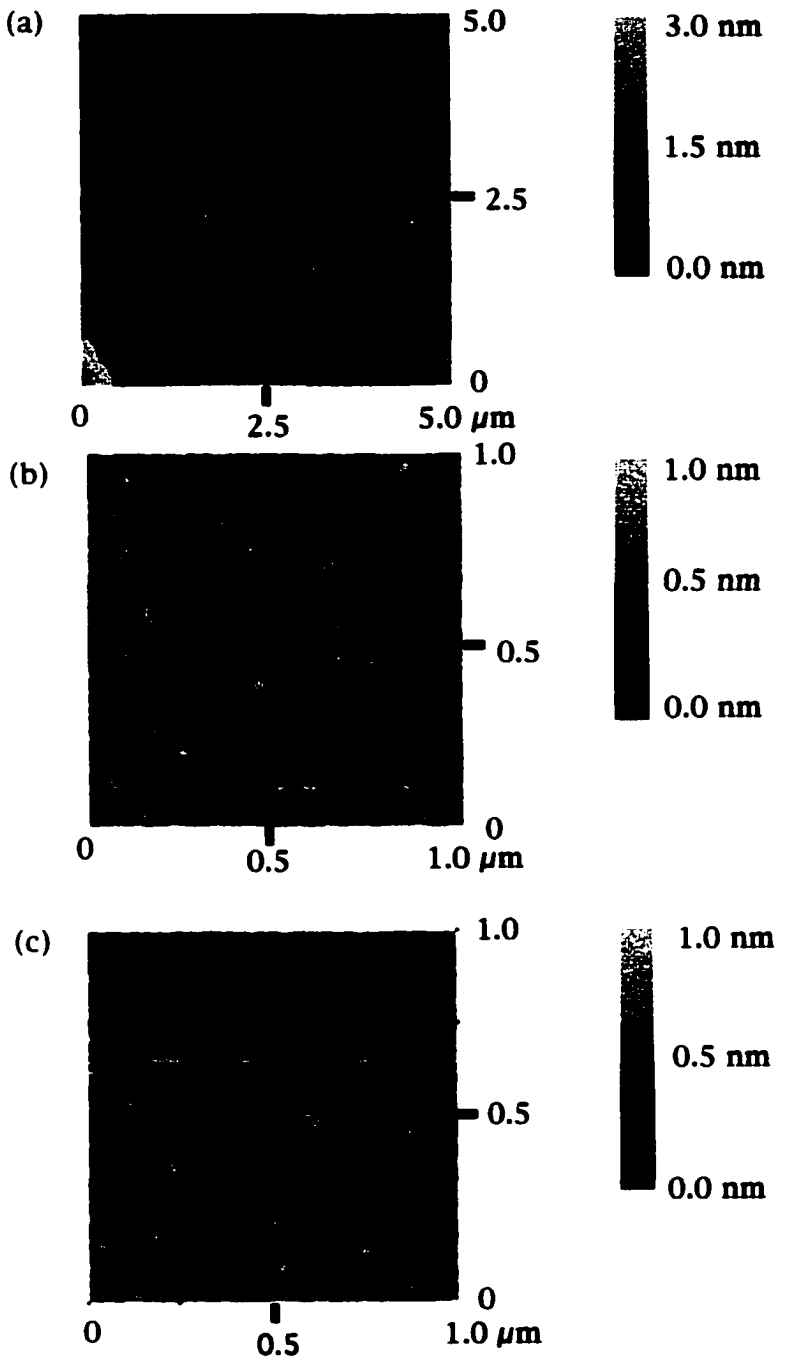

Figure 4.16 AFM images of synthetic rutile with the (100) face as received. Scan rate: 1.0 Hz; set point: 1.3V for (a) and (b), and 0.90 V for (c); drive amplitude: 700 mV for (a) and (b), and 500 mV for (c); drive frequency: 282 kHz; number of samples per scan: 512.

Reproduced with permission of the copyright owner. Further reproduction prohibited without permission.

the surface morphology was detected. After the surface treatment with 18 M H_2SO_4, AFM images of the rutile crystal of the (100) surface have not successfully been taken. After the treatment, the attraction between the surface and the AFM tip became so strong that engaging the tip to the surface in a smooth manner became very difficult.

4.4. Summary and direction for future work

Polishing the crystal surfaces with colloidal silica greatly reduced the surface roughness. However, no improvement of the surface morphologies of the crystals was observed with the chemical treatment with hot 5 M NaOH. Chemical etching of the polished surfaces with HF is considered to be the next resort to obtain flat terraced surfaces. HF with NH_4 buffer followed by heat treatment at 1100 °C has been reported to etch the $SrTiO_3$ (100) surface to produce unit-cell steps.[7] However, the anatase crystals should not be annealed at temperatures higher than 600 °C for long times since the transition from anatase phase to rutile phase occurs approximately at 600 °C for nanocrystallites.[8] Yet, bulk anatase crystals may undergo a phase transition at higher temperatures.

The synthetic anatase thin film and rutile single crystals had very small surface roughnesses, 1 to 5 nm in 1 μm scan size. These samples are promising to provide flat terraced surfaces. Heat treatment of the anatase thin film with oxygen flow may be worth trying at a higher oxygen flow.

Solving the "air bubble problem" for fluid imaging is crucial especially for real time observation of the dye adsorption. By realizing this observation, the time scale of the dye adsorption to the crystal surface, site

Reproduced with permission of the copyright owner. Further reproduction prohibited without permission.

specificity of the adsorption, and morphological effects on the adsorption will be understood. A more involved technique, *in situ* photo-assisted AFM, which is under development in our group, will add nanoscopic photoelectrochemical information. The set-up for *in situ* photo-assisted AFM consists of a chopped laser beam (514 nm), a lock-in amplifier, and electrically conductive AFM tips, in addition to the set-up for *in situ* AFM. The laser beam absorbed by dye adsorbed on a crystal surface generates photocurrent. The photo-induced component of the tunneling current between the tip and the crystal surface is isolated by utilizing the lock-in amplifier. This technique will provide important information of photoelectrochemical activities of the dye adsorbed at different sites, and this project will be completed.

Reproduced with permission of the copyright owner. Further reproduction prohibited without permission.

References cited in Chapter 4

1. V. Shklover, Y. E. Ovchinnikov, L. S. Braginsky, S. M. Zakeeruddin, and M. Grätzel, *Chem. Mater.*, **10**, 2533 (1998).

2. G. S. Herman, Y. Gao, T. T. Tran, and J. Osterwalder, *Surf. Sci.*, **447**, 201 (2000).

3. S. Chen, M. G. Mason, H. J. Gysling, G. R. Paz-Pujalt, T. N. Blanton, T. Castro, K. M. Chen, C. P. Fictorie, W. L. Gladfelter, A. Franciosi, P. I. Cohen, and J. F. Evans, *J. Vac. Sci. Technol. A*, **11**, 2419 (1993).

4. W. Sugimura, A. Yamazaki, H. Shigetani, J. Tanaka, and T. Mitsuhashi, *Jpn. J. Appl. Phys.*, **36**, 7358 (1997).

5. *MultiModeTM Scanning Probe Microscope Instruction Manual*, Digital Instruments, Chapter 7.

6. Y. Gao, *private communication* (1999).

7. A. D. Polli, T. Wagner, and M. Rühle, *private communication* (1998).

8. S. Ohkubo, K. Murakami, H. Sei, and G. Nogami, *J. Electrochem. Soc.*, **141**, 660 (1994).

Reproduced with permission of the copyright owner. Further reproduction prohibited without permission.